AD NUMBER: AD0348613
CLASSIFICATION CHANGES
TO: Unclassified
FROM: Confidential
LIMITATION CHANGES
TO: Approved for public release; distribution is unlimited.
FROM: Distribution authorized to U.S. Gov't. agencies and their contractors; Administrative/Operational Use; 1 Oct 1963. Other requests shall be referred to Office of Naval Research, Arlington, VA 22203.
AUTHORITY
20190710 - c to u per GDS schedule and c/2 to a/1 per DoDD 5200.20

THIS REPORT HAS BEEN DELIMITED
AND CLEARED FOR PUBLIC RELEASE
UNDER DOD DIRECTIVE 5200.20 AND
NO RESTRICTIONS ARE IMPOSED UPON
ITS USE AND DISCLOSURE.

DISTRIBUTION STATEMENT A

APPROVED FOR PUBLIC RELEASE;
DISTRIBUTION UNLIMITED.

GENERAL DECLASSIFICATION SCHEDULE

IN ACCORDANCE WITH
DOD 5200.1-R & EXECUTIVE ORDER 11652

THIS DOCUMENT IS:

CLASSIFIED BY_____

Subject to General Declassification Schedule of Executive Order 11652-Automatically Downgraded at 2 Years Intervals- DECLASSIFIED ON DECEMBER 31, 7[illegible].

BY

Defense Documentation Center
Defense Supply Agency
Cameron Station
Alexandria, Virginia 22314

MC-61-6-R2

A SOLUTION TO THE PROBLEM OF RAIN EROSION AT SUPERSONIC SPEEDS

(UNCLASSIFIED TITLE)

BY

BURTON D. FIGLER

INTERIM ENGINEERING REPORT

OCTOBER 1963

MITHRAS, INC.

MICROWAVE AND THERMAL RADIATION SENSORS

380 PUTNAM AVENUE, CAMBRIDGE, MASS. 02139

MITHRAS, INC.
380 Putnam Avenue
Cambridge, Massachusetts
02139

MC-61-6-R2

A SOLUTION TO THE PROBLEM OF RAIN EROSION AT SUPERSONIC SPEEDS

(Unclassified Title)

by

Burton D. Figler

Interim Engineering Report
Nonr Contract 3684(00)

October 1963

This report contains 149 and
xiv pages. Copy No. 69

MS Log 1148

FOREWORD

The research reported herein has been directed toward a study of the problem of rain erosion on radomes of high speed vehicles. Particular emphasis has been placed on the experimental investigation of a practical solution to this problem.

This research is being sponsored by the Department of the Navy's Office of Naval Research and Bureau of Naval Weapons under Contract Nonr 3684(00).

Scientific Officer for ONR Air Programs has been Lt. Cmdr. Stuart D. Kearney; and for BuWeps Missile Division, Mr. James M. Lee.

This report covers our second year's activity from October, 1962 to October, 1963.

MITHRAS would like to express its appreciation to the personnel of the Gas Dynamics Division of the David Taylor Model Basin, for their excellent support provided us in the experimental phases of this program.

TABLE OF CONTENTS

TABLE OF CONTENTS (Continued)

TABLE OF CONTENTS (Continued)

TABLE OF CONTENTS (Continued)

LIST OF FIGURES

LIST OF FIGURES (Continued)

LIST OF FIGURES (Concluded)

LIST OF TABLES

LIST OF SYMBOLS

a	$1/2 \left[\frac{\sigma}{q C_f D}\right]^2$
A	area
c	speed of sound, coefficient
C	coefficient
d	diameter
D	drag force, diameter
E	Young's Modulus
g	acceleration due to gravity
k	constant
l	equivalent length
L	length
m	mass
$\dot{m}$	mass flow rate
M	Mach number
p	pressure
q	dynamic pressure
r	radius
R	radar range
Re	Reynold's number
s	running length
S	area
t	time
T	temperature

LIST OF SYMBOLS (Continued)

V	velocity
W	weight
x	distance
z	accoustic impedance

Superscripts

'	target material

Subscripts

a	air
b	breakup
D	drop
f	friction
i	intercept
j	jet
m	missile
R	rain
Rel	relative
t	terminal
w	water
o	free stream
1	region between shock and trapped air
2	trapped air region
∞	free stream, final value
δ	diameter, pit depth
μ	absolute viscosity

LIST OF SYMBOLS (Concluded)

ν	Poisson's ratio
ρ	density
σ	surface tension
τ	time constant

I. SUMMARY

Based on previous theoretical and experimental work, a test program was conducted in a supersonic wind tunnel to determine the effectiveness of flow separation devices in providing rain erosion protection to missile radomes. These tests indicated that complete protection from rain damage can be provided by the use of flow separating spikes. It was also possible to obtain experimental verification of earlier theoretical work on this problem; in particular, those relationships which govern the design of the dome-spike combination have been substantiated.

2. INTRODUCTION

The advent of the supersonic and hypersonic flight vehicle has resulted in the appearance of several new problem areas not found in the subsonic flight regime. Vehicle stability problems, structural problems and aerothermal problems have been among those encountered. Many of these newly encountered problems have been successfully solved in recent years through the use of improved materials and systems.

One problem area, attendant to high speed flight in the atmosphere which has, until now, defied solution is that of rain erosion. All known materials show rain erosion damage if they are exposed for a sufficiently long period of time at velocities in excess of 500 or 600 feet per second. The rain erosion problem is particularly severe in the case of the non-metallic materials that currently are used in the construction of radomes and IR-domes of today's high speed aircraft and missiles. The fiberglass reinforced plastics, which are so widely used cannot withstand more than a few minutes of one-inch-per-hour rainfall at 700 feet per second and substantially less at higher velocities. At supersonic velocities, rapid erosion of radomes takes place, usually within seconds, until the dome is weakened to the point where disintegration occurs. This can then lead to the loss of the aircraft or missile. At best, it will mean destruction of the radar dish and gimbal system which are unable to withstand the sudden aerodynamic loads imposed upon them.

Although a substantial amount of experimental data has been collected on rain erosion at subsonic velocities, data on supersonic erosion phenomena has been virtually non-existent, primarily because of the lack of suitable facilities and the difficulties inherent in conducting meaningful tests. To date, sled tests have provided the primary method of obtaining data on supersonic erosion but this method has frequently proven to be unreliable and is quite expensive. Problem of vibration

and proper sled design are extremly severe and data collection is difficult. It is also extremly difficult to provide more than the equivalent of 1 or 2 seconds flight through rain with existing sled tracks. Flight profiles of current day missiles often require flight times that are in the range of 15 to 80 seconds, while advanced missiles will have flight times in excess of a hundred seconds (1). The method of extrapolation of data obtained in less than 10 seconds of rain exposure to flight times of duration in excess of 100 seconds have yet to be substantiated so that the data obtained from short duration tests may be of little if any value when considering the erosion problems associated with long duration flights.

In addition to sled tests of radomes, several limited studies have been made, in recent years, on the raindrop breakup process in high speed flows, but these have been hampered by the difficulties inherent in creating actual raindrops in supersonic flows. Although a complete understanding of the drop breakup phenomenon had not been developed at the time, MITHRAS had determined that under appropriate conditions of relative velocity between the surrounding airstream and the water drop, the water drop could be broken up into much smaller particles. It was also known that the amount of damage resulting from rain or particle erosion was closely related to the size of the impinging particle. It was at this stage that MITHRAS became interested in the possibility of breaking up raindrops through the use of flow separating spikes and thereby affording rain erosion protection to the radomes of high speed flight vehicles.

At this time MITHRAS proposed to the Navy a solution to the eroison problem based on the use of a spike projecting from the nose of the missile. A properly designed nose spike will produce a "dead air" region immediately in front of the vehicle. The relative velocity of this dead air region, it was suggested, differed sufficiently from that of the oncoming air and raindrops so as to induce breakup of the raindrops before they could strike the radome.

Our initial work had the following objectives:

To undertake

1) An experimental and analytical determination of the behavior of waterdrops in supersonic air streams;

2) An experimental and analytical determination of the effects of waterdrop impact on radome materials; and,

3) The testing and evaluation of the effectiveness of a flow separating spike as a means of protecting a radome against raindrop damage or destruction.

This report describes the research accomplished during the second year of work under this contract.

It had been intended, at the inception of the program, that MITHRAS would design and construct a small blow down wind tunnel in which the test program would be carried out. As the testing problems were more closely analyzed, however, it became apparent that such a tunnel would be of quite limited use because of its cost, small size and short run time. In addition, such a tunnel would require the expenditure of an undue amount of engineering manpower before it would become fully operational. For these reasons, plans for constructing the tunnel were dropped and instead an effort was made to locate existing wind tunnels that would be suitable for rain erosion testing.

The 18" x 18" supersonic tunnel at the David Taylor Model Basin (DTMB) was found to be ideal and was therefore selected for the second year's erosion tests. A water injection system, capable of producing high velocity waterdrops, and auxiliary recording equipment were installed at the DTMB tunnel where a number of tests were conducted at a nominal Mach number of 1.86 to study the breakup process of waterdrops in supersonic air-streams and to determine the effectiveness of flow separating spikes in providing rain erosion protection to radomes. These tests were also designed to complement wind tunnel tests on the rain erosion problem that had been conducted one year earlier by MITHRAS at MIT (Reference 2).

The results of the tests at DTMB have been extremely encouraging. These tests have demonstrated conclusively, that missile and aircraft radomes can be protected from rain erosion damage when properly designed flow separating spikes are employed.

3. THE RAIN EROSION PROBLEM

The rain erosion problem can be best illustrated by referring to Figure 1. This photograph shows a fiberglass radome after a run at supersonic velocity through rain as simulated in the wind tunnel. The rain impact area was restricted to the damaged area, otherwise it might have been difficult to find enough pieces to reconstruct the dome. It should be quite obvious what the consequences would have been if the dome had been mounted on the nose of a supersonic missile that was flying through a rain storm.

This rain erosion problem is common to all high speed flight vehicles and is not restricted to plastic materials. Indeed, erosion of structural metals is found to occur if the metal is exposed for a sufficiently long period of time at supersonic and hypersonic velocities. Ceramic radomes (proposed as substitutes for plastic domes) often are found to suffer catastrophic failure when subjected to rain erosion. It is true that, at the present time, the erosion problem is most severe in the case of missile and aircraft radomes. Damage to structural members has not yet proven unduly severe.

Because of the close tolerances in radome thickness required to keep boresight errors to a minimum, even surface damage that does not lead to radome destruction can render the dome unsatisfactory for further use and in actual flight may lead to excessively large miss distances.

3.1 Description of the Problem

The damage produced in a material by high speed impact with waterdrops appears to be linearly dependent upon the drop diameter and nearly linearly related to the drop velocity, where the damage is defined as the pit depth. In fiberglass radomes, the damage that is produced consists of cracking, pitting and de-lamination of the layers. Once the dome is weakened to the point where aerodynamic loads exceed the struc-

tural capabilities of the dome, catastrophic failure ensues.

In very thick radomes of low resin content, it may appear that only severe surface damage has resulted, but the surface damage will, in most cases, render the dome inoperative.

3.2 Past Work on the Problem

Several attempts have been made in the past 15 years to study the erosion problem. Much of the experimental work has been conducted on rocket sled ranges or shock tunnels. These investigations have ranged from basic studies of waterdrop behavior in supersonic airstreams to testing of full size radomes in simulated rain fields. A partial bibliography of these efforts is contained in the list of references of Reference 2.

In all cases reported, however, emphasis has been placed upon the problem of developing and testing improved rain resistant radome materials. Very little effort (with the exception of Reference 3) has been expended on the possibility of alleviating the erosion problem by acting directly upon the raindrops themselves prior to their impacting on the radome.

To date, the most widely used test facilities have been the rocket sled range and the shock tunnel. A limited amount of work has also been conducted in ballistic ranges. To the author's knowledge, no testing in supersonic wind tunnels, with the exception of the tests conducted by MITHRAS, has been successfully attempted.

4. THE MITHRAS SOLUTION TO THE RAIN EROSION PROBLEM

Several investigators, dating back to Lord Rayleigh, have considered the stability of liquid drops in air flows. It has been found by these investigators that for a given drop size, there is a critical relative velocity between the air and the drop above which drop breakup occurs and below which no breakup occurs. At supersonic relative velocities, drop breakup can always be expected to occur. As derived in Reference 2, the time for a drop to breakup is given by the following relation:

$$t_b = \frac{\sigma}{qv}\sqrt{\frac{\rho_w}{2C_f^3\rho_a}} \qquad (4.1)$$

and the breakup distance is

$$X_b = \frac{\sigma V_D}{q V_{rel}}\sqrt{\frac{\rho_w}{2C_f^3\rho_a}} \qquad (4.2)$$

where

t_b = drop breakup time

σ = drop surface tension

q = dynamic pressure on drop

V_{rel} = relative velocity between drop and airstream.

ρ_w = density of drop

C_f = friction coefficient between drop and airstream

ρ_a = density of airstream

V_D = relative velocity between drop and target

Based on the information available on drop breakup and on its

own research, MITHRAS had proposed to utilize a flow separation spike extending upstream of the radome to produce a region of relatively high velocity (with respect to oncoming raindrops). (See Figure 2).

The separated boundary layer from the spike in front of the body produces a trapped-air region in front of the body as indicated in Figure 2. This trapped-air region possesses a velocity with respect to oncoming raindrops of approximately the missile velocity. In addition, the air between the oblique shock and the trapped-air region possesses a velocity with respect to the oncoming raindrops that is fairly high. (Indeed, in the case of a blunt nosed vehicle, rain erosion protection can be achieved by having a sufficiently large normal shock standoff distance, i. e., by having a large diameter blunt nose). The raindrops in traversing both flow fields, will be quickly broken up into a fine mist before they can reach the missile nose. The use of the spike in front of the radome results in drag values comparable to those of a cone, instead of values appropriate to a blunt body. It is also possible to reduce radome heating rates through suitable design. A discussion of the aerodynamic behavior of spike-tipped radomes which may be found useful is contained in Reference 4. In addition, MITHRAS has intensively studied the aerodynamics and thermodynamics of spike-tipped bodies and has assembled a considerable body of data and information on these devices.

The effect of particle or drop impact on various materials has been investigated by several authors. While the relations describing damage due to drop impact have not been completely determined, it would appear that particle penetration is proportional to the particle diameter. (See Eq. B. 8a in Appendix B.) By breaking the raindrop up into much smaller drops, the damage due to individual impacts is considerably reduced and the effect of the individual impacts is spread over the entire radome surface rather than being concentrated at particular points. The total overall damage will be much less for the protected radome than for the unprotected radome.

The amount of protection afforded the radome by the presence

of a protruding spike depends upon the spike length. If the spike is too short, the radome will be eroded because the waterdrops will have impacted the radome before they have had time to disintegrate. If the spike is made too long, aerodynamic difficulties are encountered (see Section 6.1).

The proper spike length can be calculated from Eq. 4.2 by inserting the desired value of drop diameter and missile flight conditions. Reference to literature on spike-bodies will then indicate whether the spike length is aerodynamically acceptable. It should be noted that the requirements on spike design imposed by erosion resistance considerations, i.e., spike length, are generally compatible with the aerodynamic requirements on the spike design.

5. TESTS OF RAIN EROSION PHENOMENA AND TESTING OF THE MITHRAS SOLUTION TO THE PROBLEM

As a major part of its research on the problem of rain erosion of supersonic radomes, MITHRAS conducted a test program in an 18" x 18", Mach 1.86 wind tunnel at the David Taylor Model Basin, Carderock, Maryland.

The objectives of the MITHRAS test program at the David Taylor Model Basin were:

1) To study the basic behavior of high speed waterdrops in a supersonic airstream.
2) To study the drop breakup process in regions of high relative velocity between the drop and the surrounding airstream.
3) To investigate the utility of flow separating spikes in reducing rain erosion damage to radomes.

A series of models, fully described in Appendix E. 3, were utilized to investigate the various aspects of the erosion problem. These models included fiberglass radomes as well as models utilizing brass and lead impact targets. In addition, special photographic and electronic timing equipment were utilized in conjunction with a high speed water injection system. This equipment is fully described in Appendix E.

The tests at DTMB extended over nearly three weeks. During this period of time, approximately two hundred test runs were made. In order to insure the optimum utilization of the available time and to insure that maximum safety was afforded, it was necessary to follow a specific procedure when conducting the test program. This procedure involved system check-out, calibration and inspection prior to actual running.

5.1 Schlieren Photographs

Schlieren photographs were made of the flow around each of the models to:

1. Insure the tunnel was not blocked by the larger models.
2. Insure the flow around the models was not highly turbulent.
3. Determine the maximum length spike such that the boundary layer would still detach at the spike tip.

The Schlieren photographs were all taken prior to actual testing of the respective models. Figures 3 through 6 show the Schlieren photographs of the various models.

5.2 Test Run Sequence

An actual test run was conducted in the following manner:

Referring to Figure 7, a check was made to insure that valves 3, 6, 7 and 9 were open and valves, 1, 2, 4, 5, 10 and 11 were closed.

With the high pressure safety valve 1 closed, the accumulator was pumped to operating pressure, ranging from 10, 000 to 25, 000 psi. Immediately before the run, the high pressure gage was isolated from the accumulator by closing valve 3 and the safety valve (1) was then opened.

The room lighting was then turned off, and the wind tunnel started. As the tunnel is brought to operating conditions a normal shock travels down the tunnel, usually triggering the electronic flash unit. Because of the high capacitance of the flash units, a five second charging time was needed before the delay circuit could be reset. The tunnel flow was also being established in this interval. The camera operator at the front side of the tunnel was able to see a neon bulb which indicated capacitor charging. When this light was extinguished, charging was completed and the shutters of the cameras were then opened, followed by the actual release of the high pressure water into the tunnel. The water traveled past the trigger detector initiating the flash delay circuit cycle (described in Appendix E) allowing the water jet to be photographed as it came into the field of view of the camera system. The tripping of the quick opening valve was made by a second operator located behind

the tunnel. Intercom communication between the two operators was provided so that synchronization of the cameras and water equipment was insured.

Following the run, the tunnel was shut down, the safety valve closed, and the room lights turned on. The photographic system was moved from in front of the tunnel window to permit opening of the wind tunnel door and removal or inspection of the model. Along with each model is associated two water photographs, one scope timing picture, and information concerning the initial and final water pressure, model and tunnel configuration and nozzle used. This data was recorded for every run. A complete log of the test runs is contained in Appendix G.

6. DATA PRESENTATION AND ANALYSIS

6.1 Air Flow Around Models

The properties of the air flow around the various test models are most readily discerned from the Schlieren photographs taken in the wind tunnel prior to water drop impact tests.

6.1.1 Flow Field Around Sleeved Models

Figure 3 shows the flow patterns around the sleeved model. Part (a) is a Schlieren photograph of the unsleeved model while Part (b) shows the flow pattern around the sleeved model. Both flow patterns are seen to be nearly identical. The bow shocks in front of the models and the expansion region at the shoulder are clearly evident. The normal shock stand-off distance is found to be approximately 3/4 inch for the sleeved model.

6.1.2 Flow Field Around Flat Faced Models

Figure 4 clearly shows the flow patterns around the flat faced model, both with and without a flow separating spike. In Figure 4-a, the flow around the unspiked model is shown. The flow pattern is quite similar to that of the sleeved model (See Figure 3) except for a scale change. Again the normal shock and shoulder expansion are readily discerned. For the flat faced model, the shock stand-off distance is found to be approximately 1.9 inches. Figure 4-b shows a normally developed flow around the spiked flat faced model. The separated boundary layer is seen to detach at the spike arrowhead and re-attach at the shoulder of the model. An oblique conical shock attached to the spike tip, is produced by this conical boundary layer. This shock has replaced the bow shock of the unspiked model. Again the flow expands at the model shoulder.

Figure 4-c shows the flow pattern produced with too short a spike. The flow oscillates between the normal shock and oblique shock configurations. This flow instability can result in radome damage in

certain cases. Figure 4-c shows a superposition of the oscillatory flow patterns because of the relatively long exposure time of the photograph compared to the flow oscillation period.

Figure 4-d illustrates the flow pattern that results from the use of too long a spike. The boundary layer does not detach at the spike tip but remains attached to the spike for about a third of the spike length where it then detaches, expands and then reattaches at the model shoulder. A weak conical shock is produced by the spike tip itself and then a much stronger conical shock is produced by the separated boundary layer. This second shock is seen to be attached to the spike at the point of boundary layer detachment. In both Figures 4-c and 4-d, the flow expansion around the model shoulder is clearly discernable.

6.1.3 Flow Field Around Hemispherical Radome Models

Figure 5 demonstrates the flow field around the hemispherical radome model, both spiked, unspiked, and with and without collar. Figures 5-a and 5-b show the hemispherical dome without a collar. In Figure 5-a, a typical blunt body flow is established with a curved normal shock in front of the body and an expansion fan at the shoulder. Shock standoff distance is approximately 3/4". Figure 5-b clearly shows the separated boundary layer and attendant conical shock typical of spiked bodies. In Figures 5-b and 5-c, a 5 1/2" collar has been mounted at the dome's shoulder. The boundary layer reattachment point now falls at the shoulder of the collar rather than on the dome itself. In Figure 5-c, a normal flow pattern is obtained for the proper spike length while in Figure 5-d, the spike is too long and the boundary layer detachment point is no longer at the spike tip but is about a third of the way back along the spike. Comparison of Figures 5 and 4 will show the similarity in flow fields between the hemispherical models and the flat faced models.

6.1.4 Flow Field Around Ogival Radome Models

The flow field about the ogival radome is shown in Figure 6. The

attached, nearly conical shock and expansion fan appear prominently. The lack of shock detachment for streamlined bodies of this type should be carefully noted.

6.2 Test Photographs

Nearly two hundred sets of photographs (about 500 pictures) were taken during the wind tunnel tests. No object, save the needless boring of the reader would result from our presenting all these pictures and therefore only those that are representative and possess the most clarity have been included in this report.

6.2.1 Sleeved Models

Figures 8 and 9 show typical photographs taken during tests of the sleeved models. Scope photographs corresponding to these runs were also taken but are not presented here (See Figure E. 17 for a typical oscilloscope photograph taken during a test run). The drop breakup behind the normal shock preceding the sleeved models is evident in these photographs. Individual drops can be discerned upstream of the models and velocity measurements are also easily made. Of particular interest in Figure 8, is the short distance (approximately 3/4") over which the drop breakup is observed to occur.

6.2.2 Flat Faced Models

Test photos of the flat faced models are shown in Figures 10 and 11. Again, drop breakup is evident in the separated flow region produced by the spike. The flat faced model photos, taken when no spike was employed, show evidence of water drop breakup in the region immediately downstream of the bow shock. These photos also show individual drops and permit the measurement of the water velocity.

6.2.3 Hemispherical Radomes

Figure 12 shows test photographs of a run made with the unspiked hemispherical radome. Some drop breakup behind the bow shock is observed to occur.

In the case of the spiked hemispheres, examination of the test

photographs, Figures 13, 14 and 15, indicate the initiation of drop breakup in a plane of the wind tunnel which appears to lie in front of or just on the spike tip. This is quite unexpected since drop breakup should not commence prior to the conical shock produced by the separated boundary layer off the spike (See Figure 5-C). Several possible mechanisms that might produce this effect were considered. Only one explanation of the observed phenomenon seemed consistent with all observables. It appears that model blockage of the wind tunnel induced choking at a station just at or slightly upstream of the spike tip. At this location, a normal shock in the tunnel was apparently produced. The water drops, after passing this normal shock, began to break up because of the reduced stream velocity.

The reason why the tunnel should be blocked during the test runs and not during the pre-test runs when the Schlieren photographs were taken (See Figure 5) can only be explained as being due to the downstream displacement of the model during the test runs by four or five inches from where the model was located in Figure 5. It is known that tunnel blockage is most likely to occur when the test model is located at the most rearward station.

While wind tunnel choking can explain most of the observed phenomena in Figures 13, 14, and 15, it is not conclusive proof that such a situation existed. Five inch diameter flat disc blocking models were successfully run in the DTMB prior to the MITHRAS test program. That this model would not block the tunnel and a 5 1/2 " spiked model would, is somewhat open to question.

Fortunately, however, the answer to the question of whether or not tunnel blockage occurred with this particular model, is in no way essential to the problem of demonstrating the utility of flow separating spikes. If the tunnel was not choked, then the test results apply directly to the question of the effectiveness of flow separating spikes. If the tunnel was choked, then the test results show that the flow separating spike will give results superior to those expected. That such is the case can be readily demonstrated by referring to Equation 4.2

which is reproduced below.

$$X_b = \frac{\sigma V_D}{q V_{rel}} \sqrt{\frac{\rho_w}{2 C_f^3 \rho_a}}$$

In the case of drop breakup within the separated boundary layer, V_{rel} and q are both fairly large since the air inside the boundary layer is very nearly at stagnation condition. Although ρ_a is less than behind the normal shock, its effect is less than that of V_{rel} and q.

It is shown in sections C. 2 and C. 3 of Appendix C that the drop breakup distance behind a tunnel normal shock will be approximately 3 1/2 times as long as the breakup distance within the separated boundary layer of the spiked body. If protection is afforded to the dome by a normal shock located six inches upstream of the dome, then a spike of six inch length, with properly developed flow, will provide an even greater degree of protection.

Also, as indicated in Section 6. 2. 2, the spiked flat-faced models (smaller diameter than the hemispherical model) did run as expected, thereby demonstrating the behavior of the spike-tipped model.

6. 2. 4. Ogival Models

No satisfactory photographs of the two test runs made with the ogival radomes were obtained.

6. 3 Target Damage

6. 3. 1 Damage to Sleeved Models

The results of the test runs employing the sleeved model are succinctly illustrated in Figure 16, where the 1/16" thick lead and .003" thick brass targets have been arranged in order of increasing sleeve length. The unprotected targets (unprotected except for the 3/4" thick air layer between the target and the detached shock) are heavily damaged in the impact area. As the length of the protective sleeve is increased,

the target damage is seen to decrease at an extremely rapid rate. By the time the sleeve length has been increased to 3.5", target pitting has been reduced to quite a small level.

6.3.2 Damage to Flat Faced Models

Figure 17 shows the effect of using a flow separating spike in front of a flat faced model. The 1/16" thick targets in the upper half of the fig. e were impacted by the high velocity water stream with no flow separating spike in front of the model. The targets in the lower half of the figure were run with various lengths of flow separating spikes. The three upper targets were moderately pitted and dented, although not nearly to the extent that the sleeved model target was damaged when run without the protective sleeve (See Figure 16).

The lead target corresponding to a three inch spike length showed some pitting, however this is not unexpected since, for this short a spike, airflow instability, corresponding to that shown in Figure 4 can be anticipated. The two lead targets corresponding to a 6.5" spike and a 10" spike showed very little pitting, indicating that a sufficiently long drop breakup region had been provided.

The damage to the upper three targets in Figure 17 is seen to be considerably less than the upper left hand lead target in Figure 16 although both models employed were similar. The reason for the lesser damage to the flat faced model targets becomes apparent when it is appreciated that the drop breakup distance does not scale with model size but is fixed for given operating conditions. In the case of the sleeved model, the shock standoff distance is approximately 3/4" while that of the flat faced model is approximately 1.9". This latter standoff distance is sufficiently long to partially break up the oncoming stream of water drops so that the damage to the larger targets is less than that of the sleeved model targets.

6.3.3 Damage to Hemispherical Radome Models

The hemispherical radomes were each subjected to three runs, with initial pressures of 15 kpsi in the nitrogen charged accumulator.

One hemisphere, Model D3, without the spike mounting hole in the nose is shown in Figure 18 before the test runs and in Figure 19 after the test runs. Figure 20 provides a closeup view of the eroded area of this dome. The damaged area on this dome extends over an area of roughly 1/2 square inch which is, in all likelihood, the extent of the high velocity stream of water drops. Measurements on the hemispherical radome showed that, in the region adjacent to the drop impact area, the dome thickness had a standard deviation of 0.0021 inches. The depth of the eroded region was then measured and it was found that somewhat more than 0.030 inches of material had been eroded away. The large difference between the standard deviation of the dome thickness and the erosion depth showed that the rain erosion had removed the dome material and that variation in material thickness could not have produced an appreciable part of the measured damage.

The two spiked hemispherical models were not run in identical fashions. Figure 21 shows the appearance of one of the radome models prior to testing. Model D2 was tested by making three firings, identical to those on Model D3, with the spike not installed. The dome was then rotated 180°, a 6" spike installed, and another three firings, at identical conditions, made. This permitted direct comparison on the same model, of the damage produced with and without the use of a flow separating spike. Figure 22 shows the dome after testing. The damaged region just above the spike-hole was produced when the dome was run without the flow separating spike. The region just below and slightly to the left of the spike-hole, where some paint has been removed, is the impact region when the model was run with a 6" inch spike in place. The effectiveness of the spike is clearly apparent. When the dome thickness variation was measured, it was found that the dome thickness standard deviation was 0.0018 inches in the vicinity of the impact areas. The eroded region produced, with no spike in place, showed a measured erosion depth of approximately 0.030 inches while the erosion depth in the impact region produced with the spike was only 0.0018 inches. This latter value is accounted for by the random variation in dome thickness. Thus no measurable rain erosion damage was produced when

the flow separating spike was installed.

The second spiked hemispherical radome, Model D1, was tested in a manner identical to that of Model D3 except that a 6" spike was employed. Figure 23 shows the dome after testing while Figure 24 provides a closeup of the impact area. Again, except for paint removal, no visible damage to the dome itself was apparent. Measurements on dome thickness showed a standard deviation in the vicinity of the impact area of 0.0017 inches, while the measured erosion depth was 0.0015 inches which, once more, is accounted for by random variations in dome thickness. Figure 19 and 20 should be compared with 23 and 24.

One of the primary concerns during the testing of the spiked radomes was to insure that the injected stream of water drops did not actually strike the spike. This was accomplished by rotating the water injection nozzle by a small amount so that the stream diverged slightly from the tunnel center line. This offset of the nozzle resulted in the hemispherical domes being impacted at a lateral distance of 3/4" from its axis of rotation. Figure 25, drawn to scale, illustrates the path of the water stream and shows the distance by which the stream missed the tip of the flow separating spike.

6.3.4 Damage to Ogival Radome Models

The ogival radomes were tested in a manner nearly identical to the hemispherical models. Since reported erosion damage to streamlined bodies had been most severe at the tips of these bodies, the water injection nozzle was roughly aligned so that the water drop impact area would occur near the tip of the ogival doms. It had been intended that the two ogival domes would be subjected to three test firings each, so that the test conditions of the hemispherical radome models would be duplicated. However, both ogive models were so severely damaged after a single firing, that the tests were terminated for fear of completely destroying the models. Figure 26 shows an ogive radome prior to testing and Figures 27 and 28 show the two ogive radomes after the tests.

In looking at Figure 27 and 28 and then referring back to Figure 6, it becomes apparent that the lack of any shock detachment distance is in

large part responsible for the extremely severe damage to the ogive. The stream of water drops is largely intact at the instant of impact and the resulting dome damage is intense.

7. PRACTICAL ASPECTS

As in any branch of science and engineering, the utility of any idea or concept ultimately depends upon the practical application. In the case of the spiked radome, several problems must be considered before the concept of the spiked dome can be said to be practical. These problems include aerodynamic and aerothermal considerations, effects on radar performance, and structural design. In the following sections these areas will be briefly covered. No attempt will be made to go into these problems in any depth since that would carry us beyond the scope of this report.

7.1 Drag and Radar Range

The use of a spike and collar arrangement on a missile can entail either an increase in the frontal areas of the missile or a reduction in the radar dish diameter. Figure 29 illustrates the three possible situations. In the upper diagram is shown an ogive missile nose with unit radar range, R and unit drag D. The radar range equation for a common transmitting and receiving antenna shows that R is linearly proportional to the radar dish diameter, δ. The missile nose drag on the other hand is proportional to the square of the missile diameter d. Both these relations are illustrated in the right hand portion of Figure 29. If the missile diameter is increased to permit the addition of a collar and spike, we have the case shown in the center diagram of Figure 29. The radar range is unaffected while the drag is increased. In the lower portion of Figure 29, we see the situation when the radar dish diameter is reduced. Here the radar range decreases while the missile drag remains essentially unchanged.

What are the percentage changes in drag and radar range in a practical situation? Let us consider an 8 inch diameter missile with a 6 inch diameter dish. For proper dome cooling, the collar diameter should be 1 1/2 times the dome diameter or roughly 9 inches. The

drag increase is thus found to be

$$9^2/8^2 - 1 \cong 26\%$$

or if the dish diameter is reduced to 5.34 inches, the reduction in radar range is found to be

$$1 - \frac{5.34}{6.00} \cong 11\%$$

If both the collar diameter and dish diameter are changed we might choose the following;

$$d = 8.4"$$
$$\delta = 5.6"$$

The drag increase is only 10% while the radar decrease is only about 6 1/2%. However there are advantages that are to be gained by going to the spiked-dome configuration. If the original configuration were 24 inches long (a3:1 fineness ratio) and the thickness (half-wave) were 0.1 inches, then the new configuration (thin wall) with a thickness of 0.03 inches would be roughly only one third the weight of the original configuration, (the thinner wall is possible because of the lower aerodynamic loads). In addition, an increase in radar transmission (because of the thinner domes possible) of about 10% is possible. Radome cost and boresight error are decreased because of the spherical radome shape. When these advantages are weighed against the drag and range penalties, it appears that a net advantage accrues. In fact, if the 10% gain in radar transmission due to the thinner dome construction is balanced off with the range decrease caused by the smaller dish diameter then,

$$\delta = 5.4"$$
$$d = 8.1"$$

and the drag penalty is now only 3% with radar range unaffected.

In addition, it is possible to realize structural benefits from the use of spiked domes because of reduced thermal and aerodynamic loads.

7.2 Spike Length

The drop breakup distance equation determines the minimum spike length required for a given body diameter, Mach number and altitude. Figure 30 plots this relation for spiked and unspiked hemispherical bodies for various Mach numbers and altitudes and for a waterdrop diameter of 1 inch. For drop diameters of reasonable size, the breakup distance equals the ordinate multiplied by the drop diameter to the 3/4ths power. Figure 31 provides a curve of drop diameter to the 3/4ths power versus drop diameter for convenience.

Based on the results of Reference 5, the maximum permissible ratios of spike length to body diameter (spike length is measured from collar face) are:

(M)	(L/D) Max.
1.86	1.31
3.	1.44
4.	1.73

Given the missile diameter, the maximum spike length possible is then obtained. Of course if this length is found to be less than the drop breakup distance, then a collar can be added to allow the use of a longer spike.

Also plotted in Figure 30 is the drop breakup distance for an unspiked hemisphere (breakup occurring in the region between the normal shock and the dome). It is interesting to note that at the low supersonic Mach numbers, the breakup distance for the spiked hemisphere is less than that for the unspiked hemispheres, while at the higher Mach numbers, the reverse holds. The increasing shock strengths (with attendant higher air densities) at the higher Mach numbers, cause this effect.

As a practical example, let us consider an 8 inch diameter missile at Mach 1.86 flying at 15,000 feet altitude. For 0.1 inches diameter raindrops, the drop breakup distance is found to be

$$20 \times 0.18 = 3.6''$$

which is less than the 11 inch spike that could be used with this vehicle.

7.3 Radar Performance

The effect of the spike on radar performance, has in the past been questioned. Both theoretical and experimental investigations have shown that the spike has no harmful effects on radar performance as long as the spike cross sectional area is much less than the radar dish area. In the practical situation, this is always the case. In effect this condition means that aperture blockage due to the spike is negligible. It has even been shown experimentally (Ref. 6) that certain spike support configurations can lead to radar side lobe suppression with a resultant improvement in radar performance. This condition is not always attained, but the important point to be made is that radar performance does not have to be degraded by the presence of the flow separating spike, and if an attempt is made to consider the spike and radar systems jointly, rather than as separate pieces of hardware, then it may be possible to attain superior radar system performance than would be possible without the presence of the spike.

7.4 Angle of Attack

If the spiked hemisphere body were flown at an angle of attack, the air flow pattern would have the appearance shown in Figure 32a. The lower portion of the radome would be unprotected from rain erosion and at the reattachment point A significant increase in pressure loading and heating would occur. This problem can be simply avoided by a small angulation of the spike with respect to the missile so that the flow pattern illustrated in part (b) of Figure 32 is obtained. In this case no pressure or thermal overloads are produced on the radome and adequate rain erosion protection is obtained. Experimental verification of the performance of spiked bodies at angle of attack with and without angulated spikes has been obtained (Reference 5). MITHRAS has designed a self-angulating spike, driven by ambient air pressure that lines the spike up with the free stream.

This design allows the spike to behave in a manner similar to a weather vane. By using a flow separating spike of this design, good angle of attack performance is obtained for moderate values of pitch and yaw (up to about $\pm 10^{0}$).

8. DISCUSSION OF RESULTS AND CONCLUSIONS

The series of test runs with the sleeved models indicate the utility of Equation 4.2 in obtaining an estimate of drop breakup distance in high speed air flows. In addition, the results of these tests were in good agreement with the results of the MITHRAS tests at M. I. T.'s Gas Turbine Laboratory. Drop breakup was observed to begin immediately behind the normal shock preceding the model. Target damage was considerably reduced with the use of a 3.5 inch sleeve extending upstream of the target. Once again, the utility of a stagnated air region in inducing the breakup of high velocity waterdrops was clearly demonstrated.

Good agreement on the determination of drop size was obtained by employing two different methods, photographic measurements and measurement of target pit depth. Equation E-1 of Appendix E, which was used to predict drop size, was found to underestimate the drop size by roughly an order of magnitude, however. This equation had been empirically derived in Reference B-1 for the case of an atomizing jet in an airstream. Velocities considered were on the order of four or five hundred feet per second. Our use of this relation was based on the hypothesis that this empirically derived equation could be utilized at the higher velocities present in the rain erosion case. It now appears, based on the results obtained during the tests reported herein, that this extrapolation is not valid. Thus the use of Equation E-1, as it stands, will not give the proper drop size for the breaking up jet.

The distance required for the water jet to breakup into a stream of drops was predicted in Appendix D by applying the water drop breakup equation to the jet breakup case. It was found during the tests that the use of the drop breakup equation provided estimates of the jet breakup distance that were conservative, i.e., the equation

overestimated the jet breakup distance. The extent of overestimation could not be determined from the results of recent tests.

In regards to the problem of jet breakup, some mention should be made of the effect of nozzle design. It was observed during the tests that nozzles 3 and 4 (Figure E-4) produced a highly atomized jet; one in which individual drops could not be discerned, either photographically or by the measurement of pit depth. It appeared that the jet was broken up, quite rapidly, into a fine mist. Nozzle 2, however, was found to produce waterdrops in sizes ranging from 0.020" to 0.080" when the relative velocity between the jet and the airstream was properly adjusted. For this reason Nozzle 2 was used in the great majority of test runs.

The flat faced, ogival, and hemispherical models demonstrated quite conclusively that even a very thin region of still, or at least slow, air has an appreciable effect on the damage produced. In the case of the ogival domes, where the oblique shock is attached, the dome was nearly destroyed, but in the case of the hemispherical domes, where the shock was detached on the order of 3/4 inch, the damage, although severe, was much less than that produced on the ogival domes.

The usefulness of flow separating spikes was conclusively demonstrated in this series of tests. The unprotected domes were observed to suffer severe rain damage while the protected domes were left undamaged after being subjected to the same rain environment. Streamlined radomes were found particularly susceptible to rain erosion while the blunter shapes did have some slight erosion resistance.

As a practical matter, the spiked missile is found to suffer no performance penalties when compared with pointed bodies and may even prove to be superior in performance.

It must be concluded, that based on the outcome of its recent tests, MITHRAS, has successfully achieved the three goals listed in the introduction to this report.

9. REFERENCES

1. Holter, M. R. Morita, Y., Target-Warning and Threat-Detection Investigation (U). Vol. III, part II, Appendixes, Annual Report (Fourth quarterly) 1 April 1961 to 31 May 1962, Infrared Laboratory, Institute of Science and Technology-The University of Michigan, Ann Arbor, Michigan, June, 1962, (S)

2. Figler, B. D., Parkin, W. J., Wilson, J. C. Jr., Rain Erosion Suppression at Supersonic Speeds (U), MITHRAS Report MC-61-6-R1, Cambridge, Mass., October, 1962 (C)

3. Engel, O. G., Fragmentation of Waterdrops in the Zone Behind an Air Shock" Journal of Research of the National Bureau of Standards" Vol. 60, No. 3, March 1958, Research Paper 2843, pp 245-280

4. Crawford, D. H. Investigation of the Flow Over a Spiked-Nose Hemisphere-Cylinder at a Mach Number of 6.8. NASA TN D-118, December, 1959 (U)

5. Lorah, L. D. and Hill, J. A. F. Development of Improved Cooling Systems for High Performance Missiles (U), NAVWEPS Report 8041, NOTS TP3034, September, 1962 (C)

6. Charlton, T. E. The Quadripod Space Frame and Antenna System Performance, The Antenna Laboratory, Department of Electrical Engineering, Ohio State University, Report number 1180-2, 15 Mar 1961 (U)

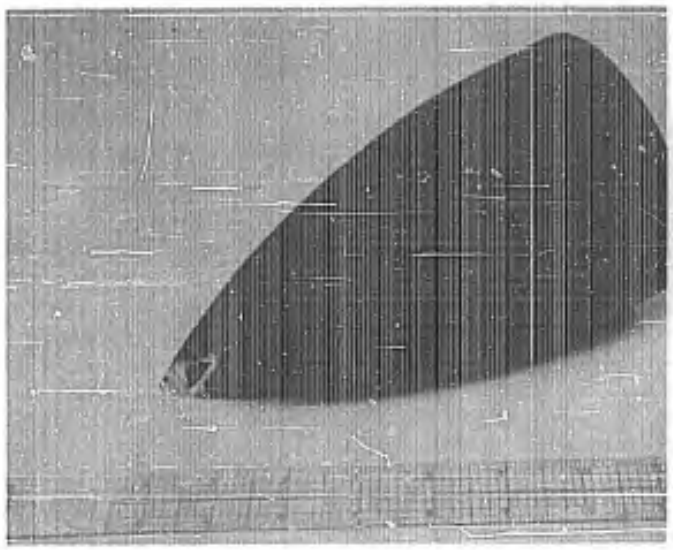

Figure 1: Radome After Simulated Flight Through Rain

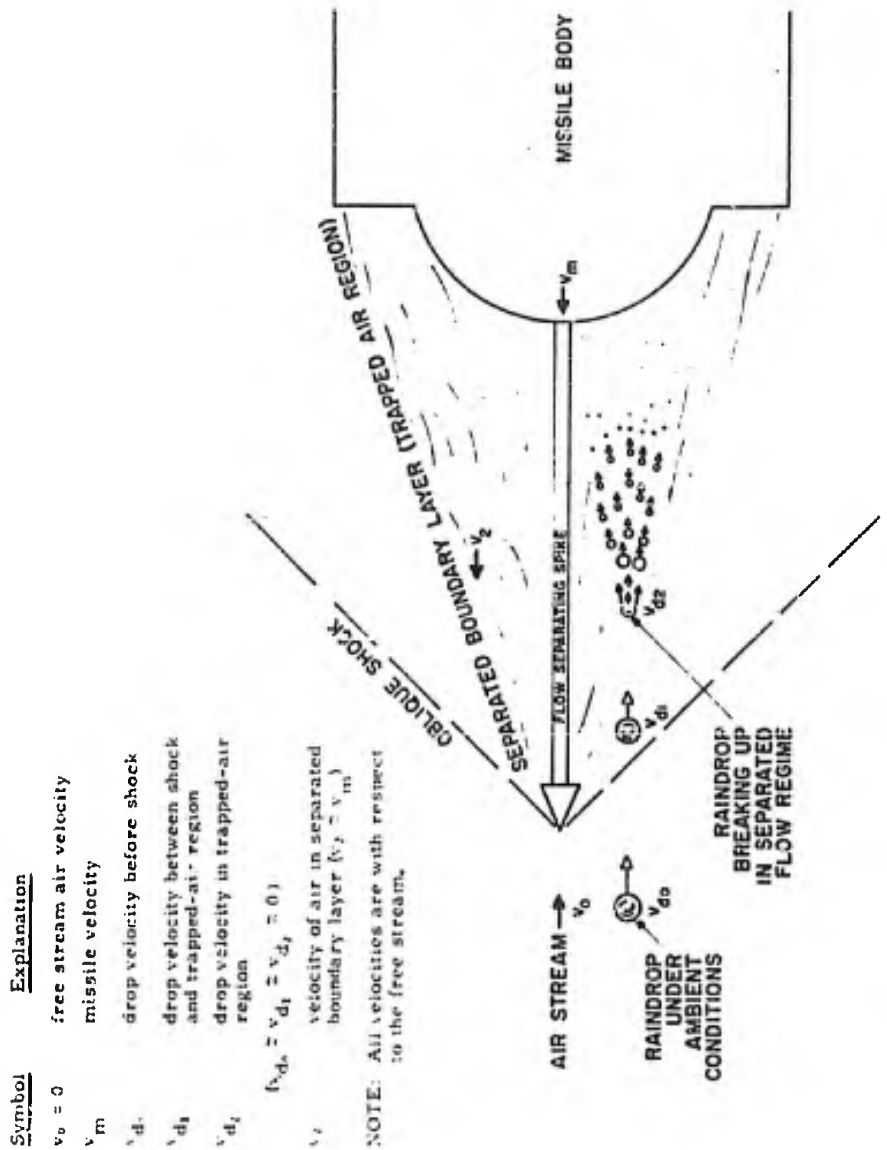

Symbol	Explanation
$v_o = 0$	free stream air velocity
v_m	missile velocity
v_{d_1}	drop velocity before shock
v_{d_2}	drop velocity between shock and trapped-air region
v_{d_3}	drop velocity in trapped-air region
$(v_{d_o} = v_{d_1} = v_{d_3} = 0)$	
v_2	velocity of air in separated boundary layer ($v_2 = v_m$)

NOTE: All velocities are with respect to the free stream.

Figure 2: Raindrop breakup in a separated flow regime.

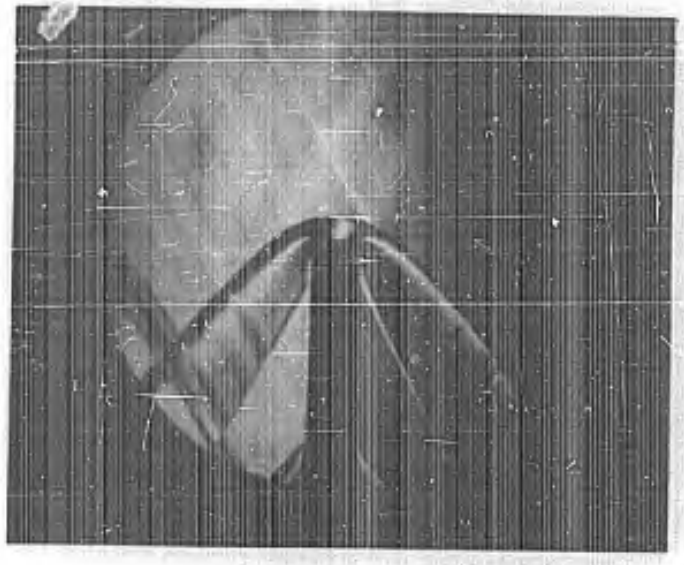

b. With Plexiglass Sleeve

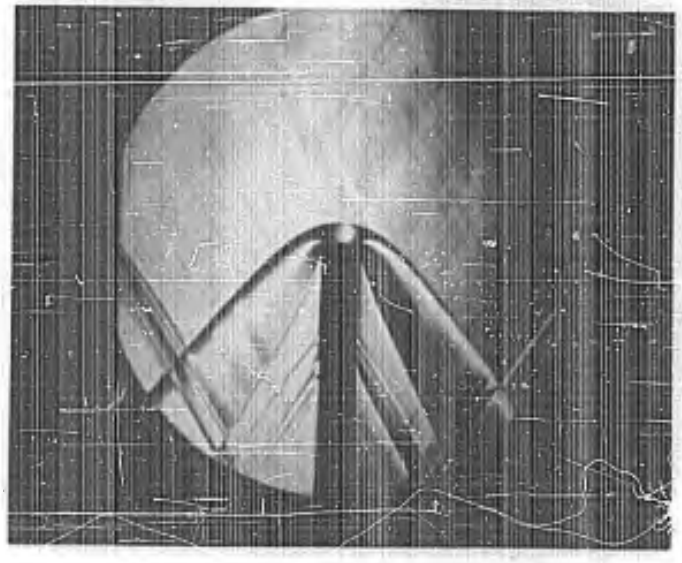

a. Without Plexiglass Sleeve

Figure 3: Schlieren Photographs of Sleeved Models

b. With Spike of Correct Length

a. Without Spike

Figure 4: Schlieren Photographs of Flat Faced Models

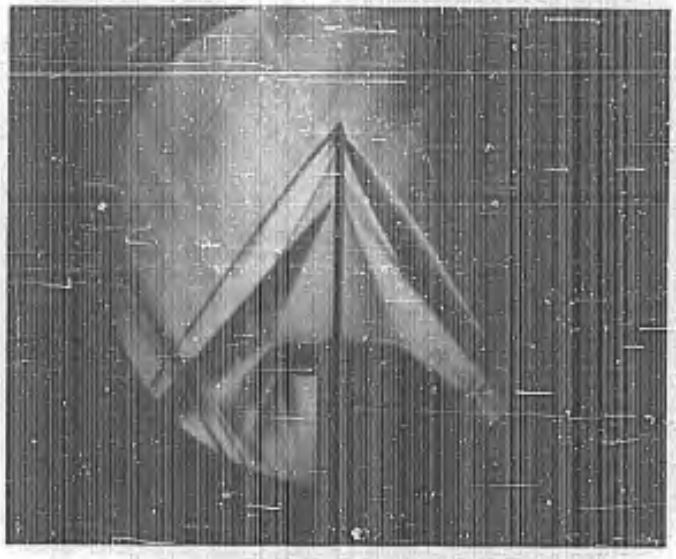

d. With Long Spike

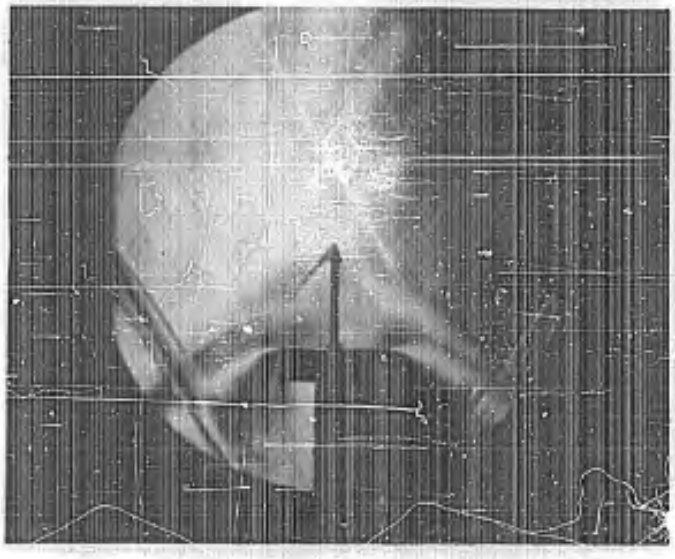

c. With Short Spike

Figure 4 (continued): Schlieren Photographs of Flat Faced Models

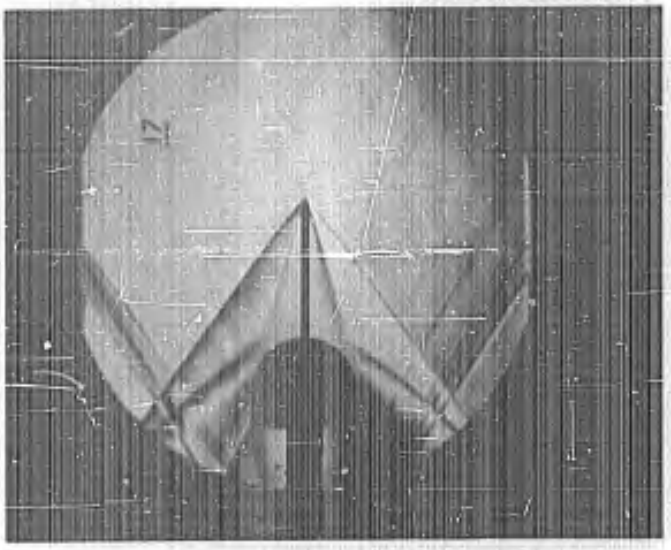

b. With Spike

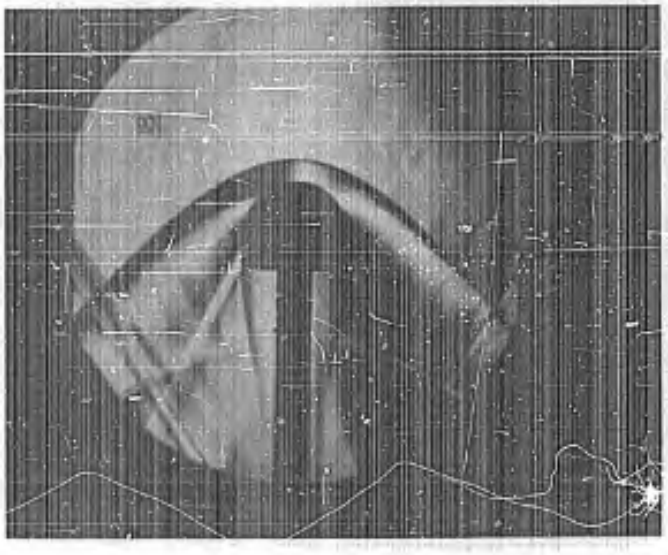

a. Without Spike

Figure 5: Schlieren Photographs of Hemispherical Radome Models

d. With Overlong Spike and 5 1/2 inch Collar

c. With Spike and 5 1/2 inch Collar

Figure 5 (continued): Schlieren Photographs of Hemispherical Radome Models

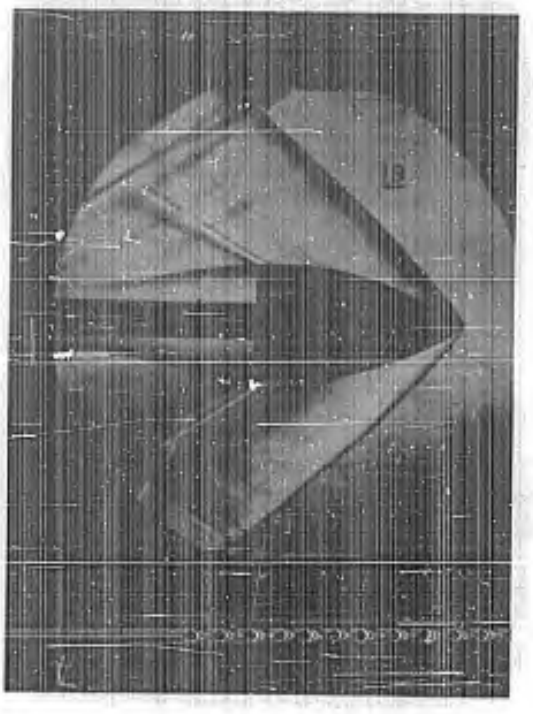

Figure 6: Schlieren Photograph of Ogive Radome Model

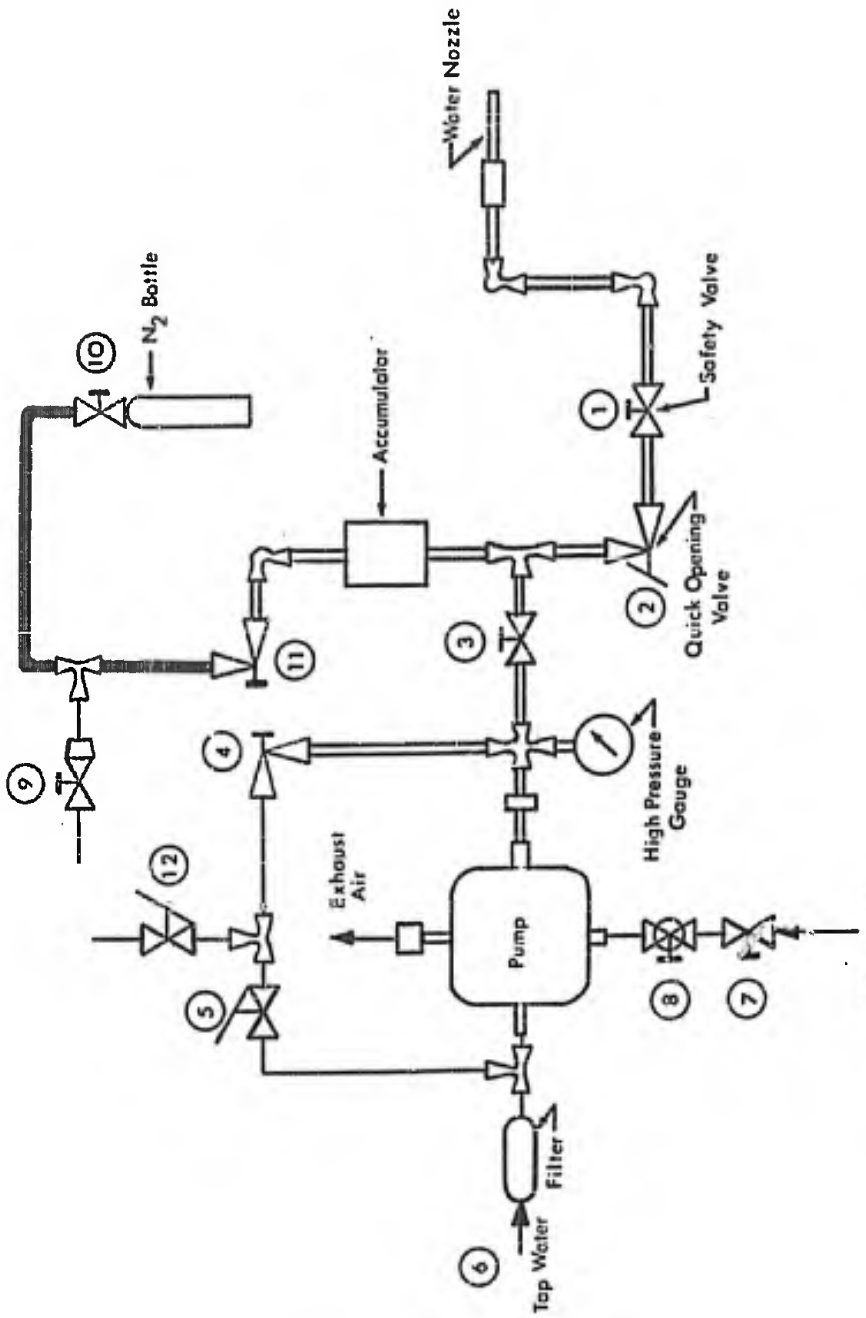

Figure 7: High Pressure Pumping System Layout

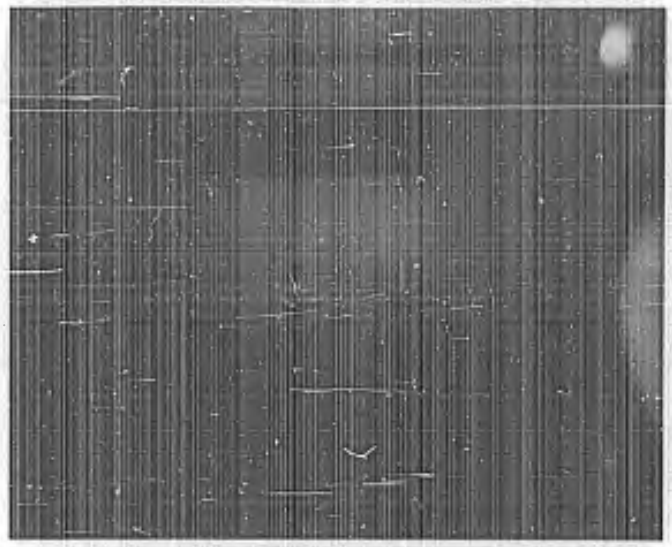

a. First Photograph (t = 760 μ sec)

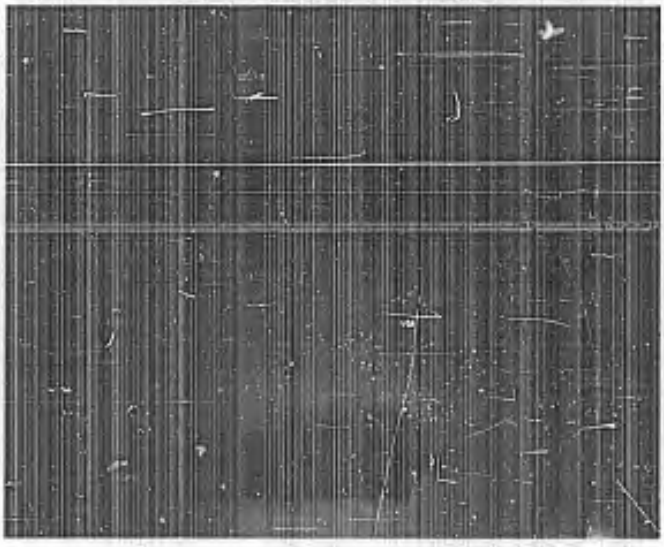

b. Second Photograph (t = 1120 μ sec)

Figure 8: Test Photographs of Sleeved Model (Run No. 46; No Sleeve)

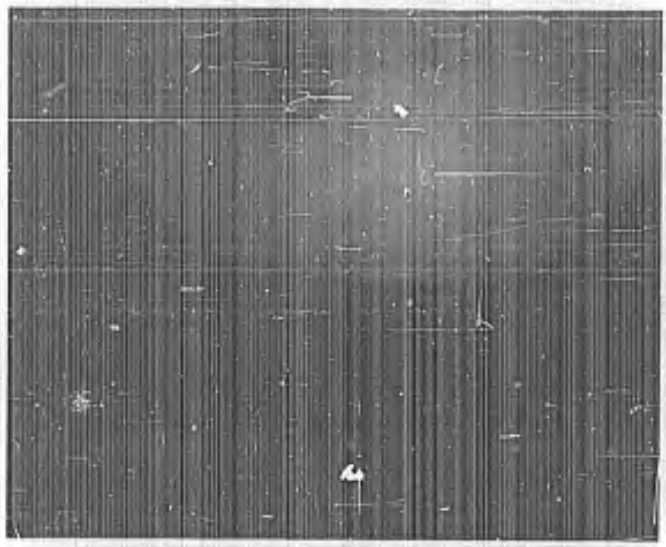

a. First Photograph (t = 510 μ sec)

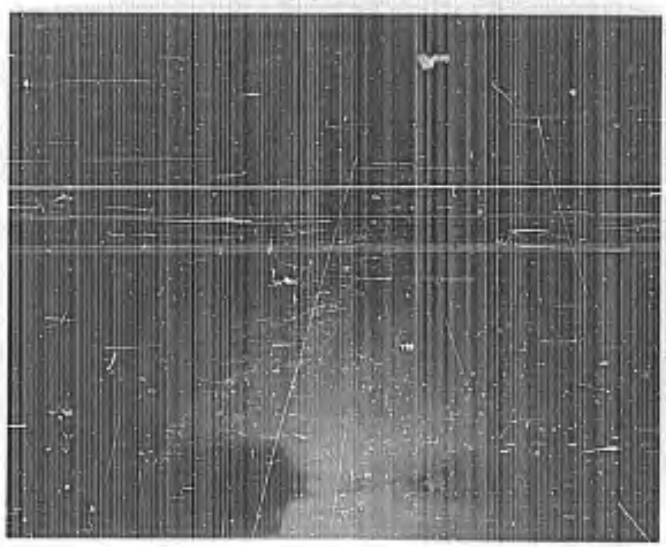

b. Second Photograph (t = 670 μ sec)

Figure 9: Test Photographs of Sleeved Model (Run No. 107; 5 inch Sleeve)

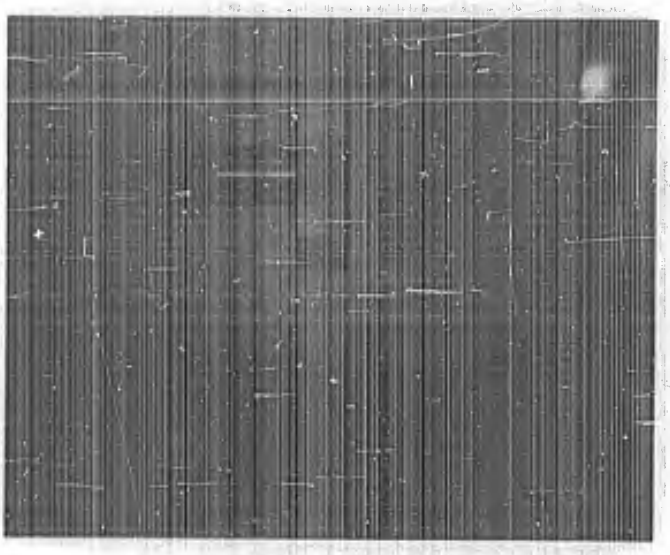

a. First Photograph (t = 615 μ sec)

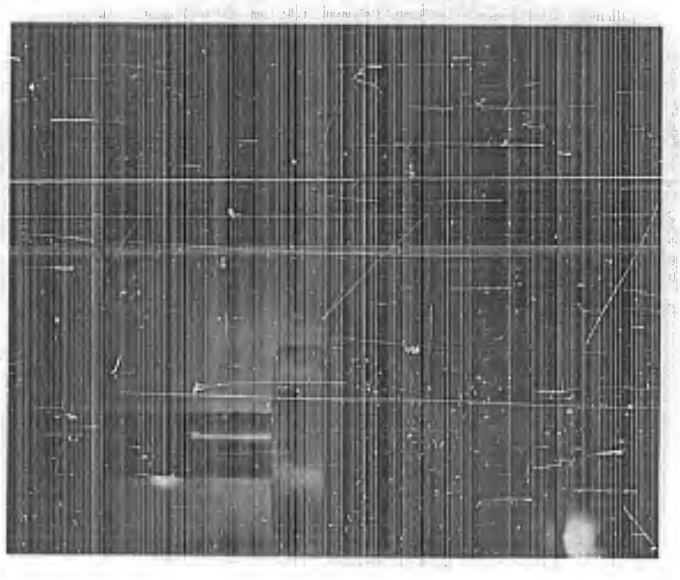

b. Second Photograph (t = 740 μ sec)

Figure 10: Test Photographs of Flat Faced Model (Run No. 28; No Spike)

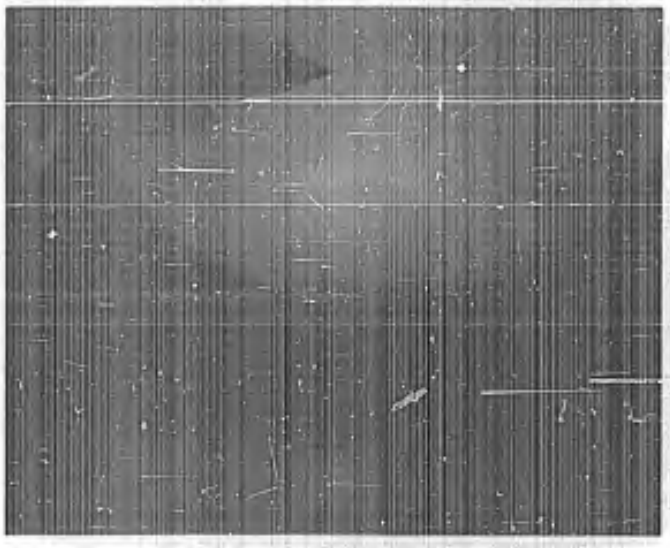

a. First Photograph (t = 610 μ sec)

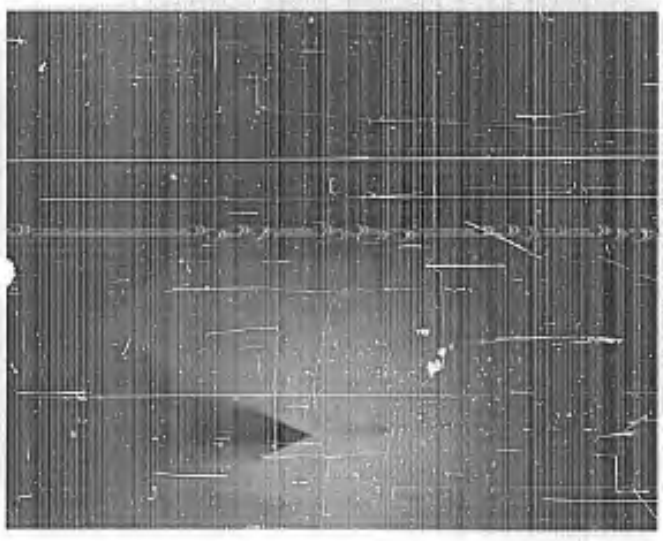

b. Second Photograph (t = 765 μ sec)

Figure 11: Test Photographs of Flat Faced Model
(Run No. 89; 6 1/2 inch Spike)

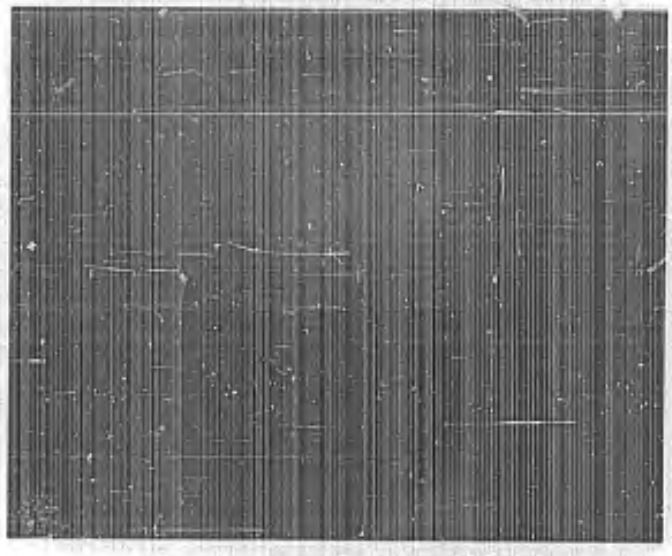

a. First Photograph (t = 580 μ sec)

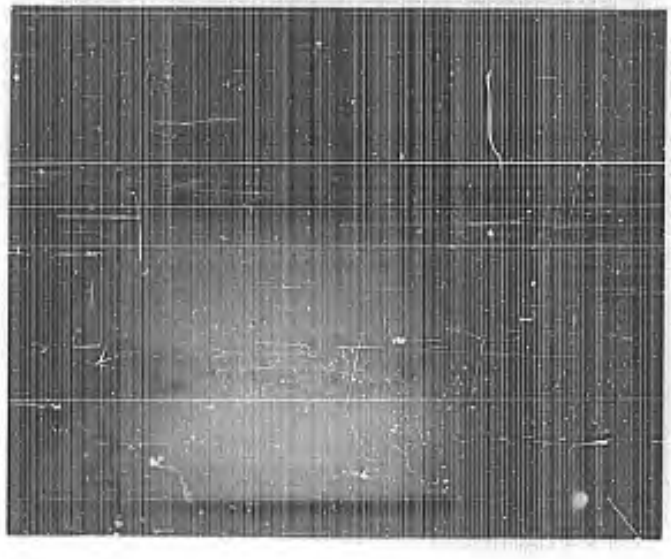

b. Second Photograph (t = 870 μ sec)

Figure 12: Test Photographs of Hemispherical Radome
(Run No. 136; No Spike)

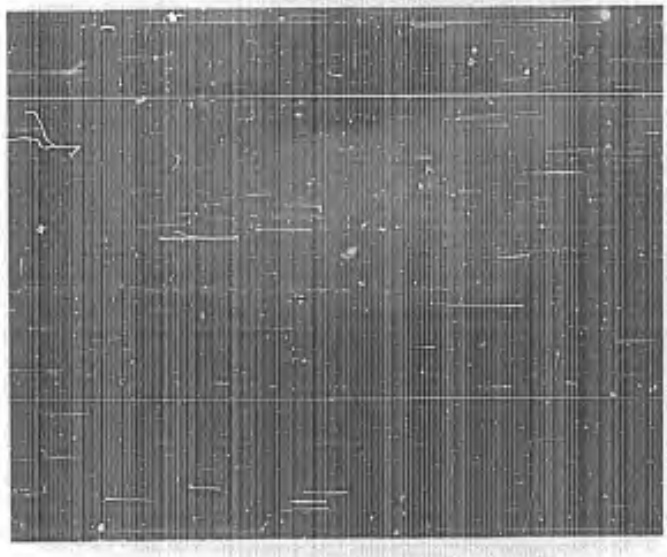

a. First Photograph (t = 580 μ sec)

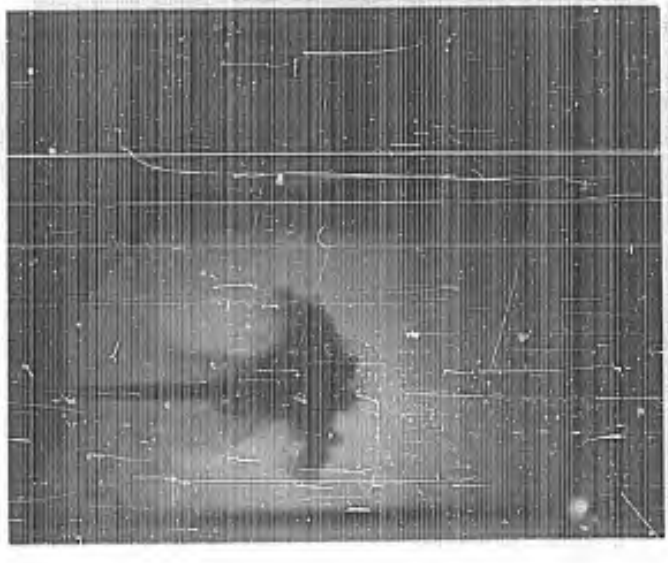

b. Second Photograph (t = 870 μ sec)

Figure 13: Test Photographs of Hemispherical Radome
(Run No. 132; 6 inch Spike)

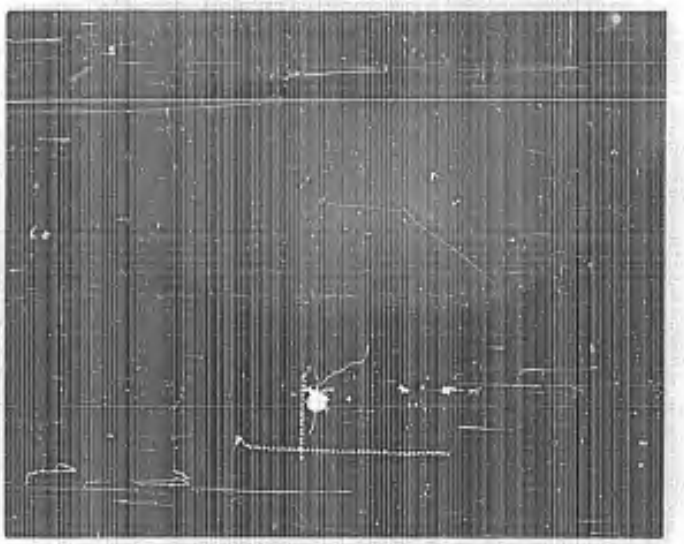

a. First Photograph (t = 580 μ sec)

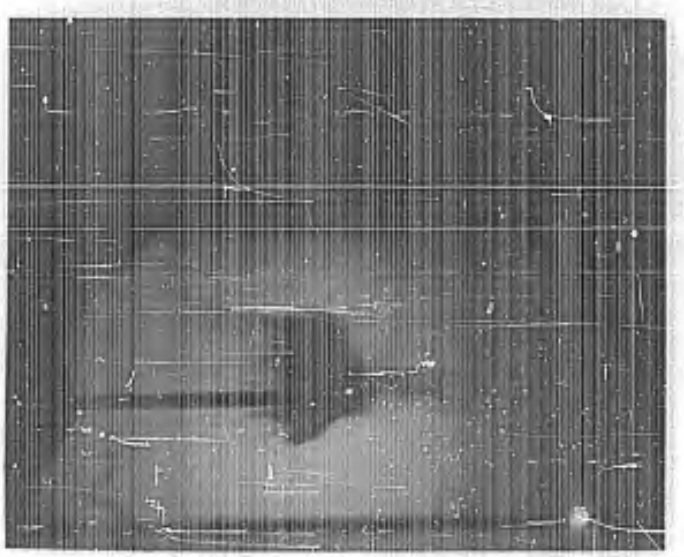

b. Second Photograph (t = 865 μ sec)

Figure 14: Test Photographs of Hemispherical Radome
(Run No. 134; 6 inch Spike)

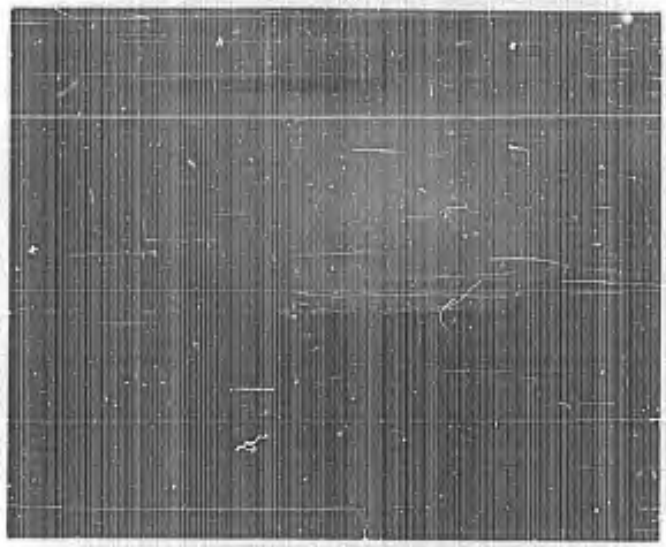

a. First Photo (t = 560 μ sec)

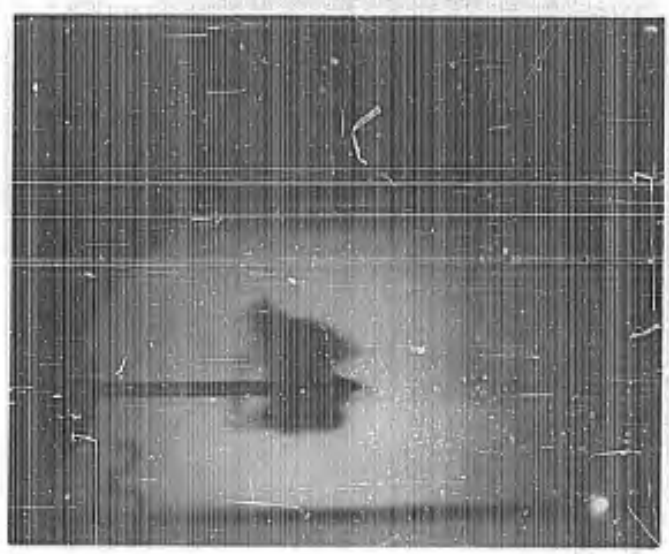

b. Second Photo (t = 850 μ sec)

Figure 15: Test Photos of Hemispherical Radome (Run no. 142; 6" Spike)

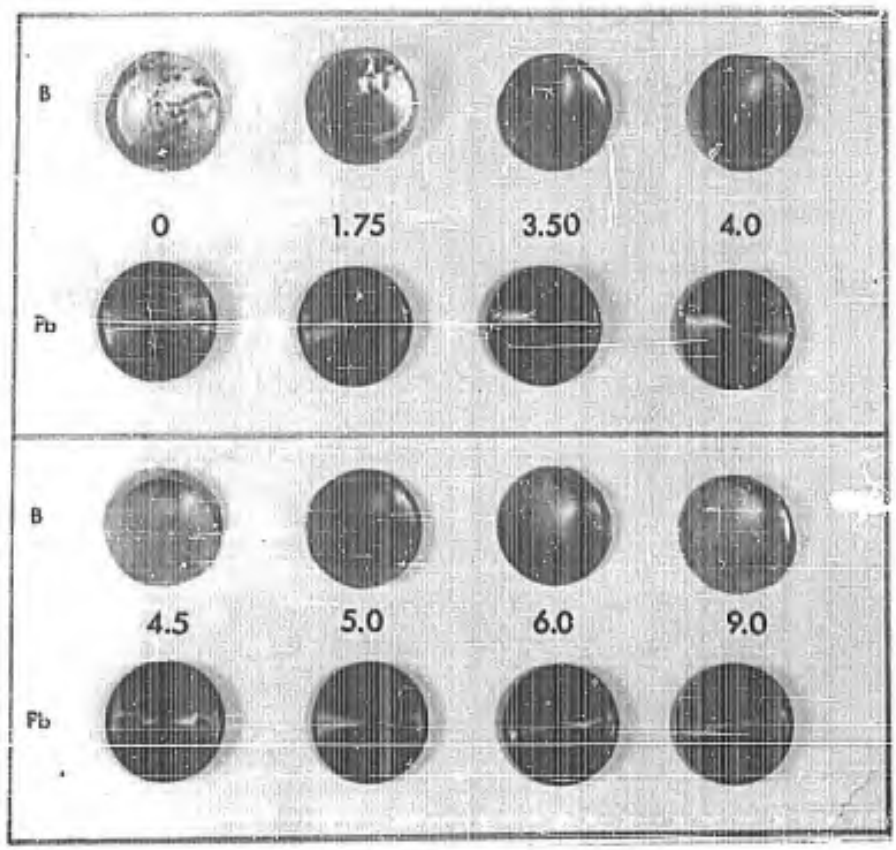

Figure 16: Target Damage Versus Breakup Length (in.). (Sleeved Model)

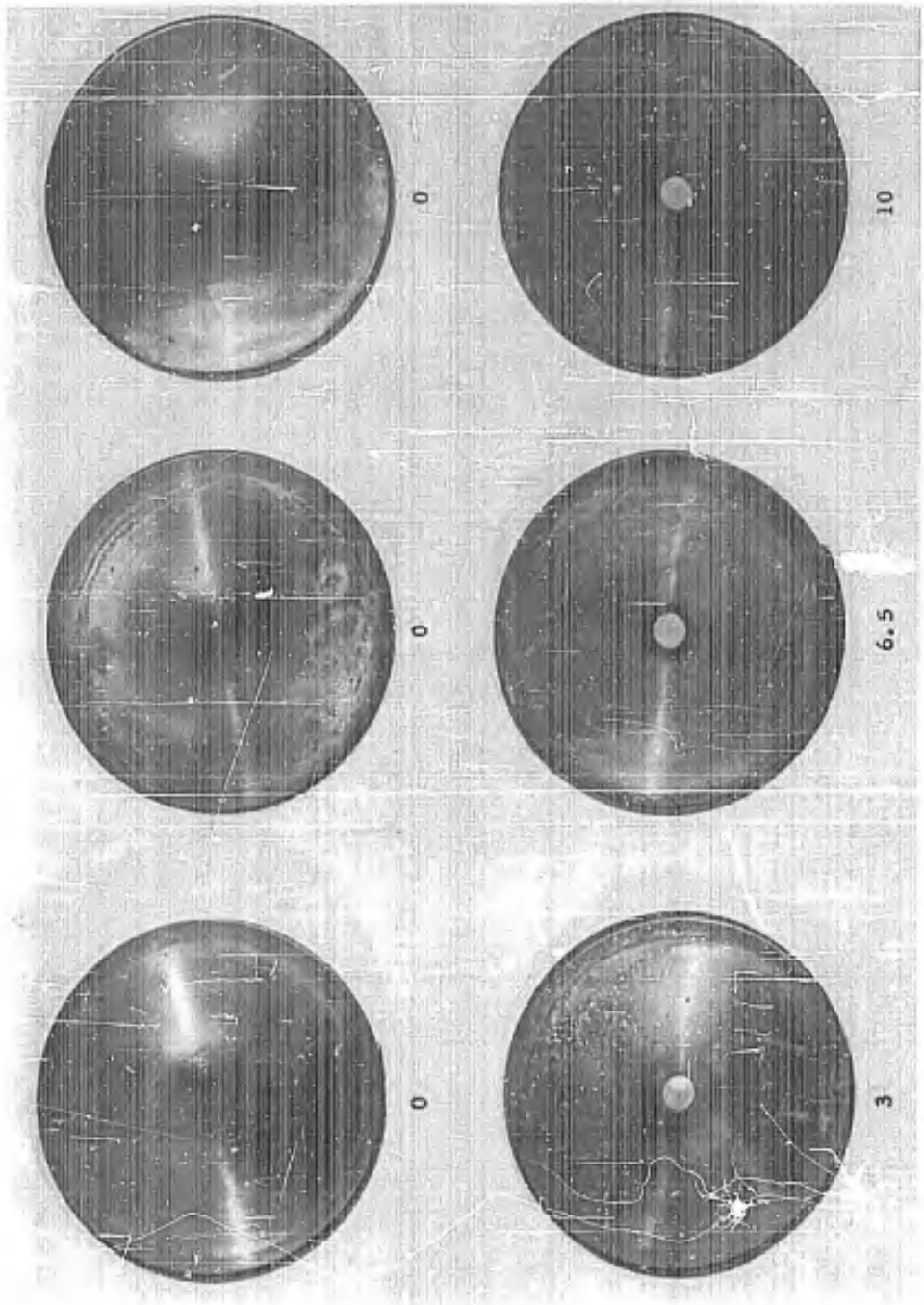

Figure 17: Target Damage Vs. Spike Length (in) (Flat Faced Model)

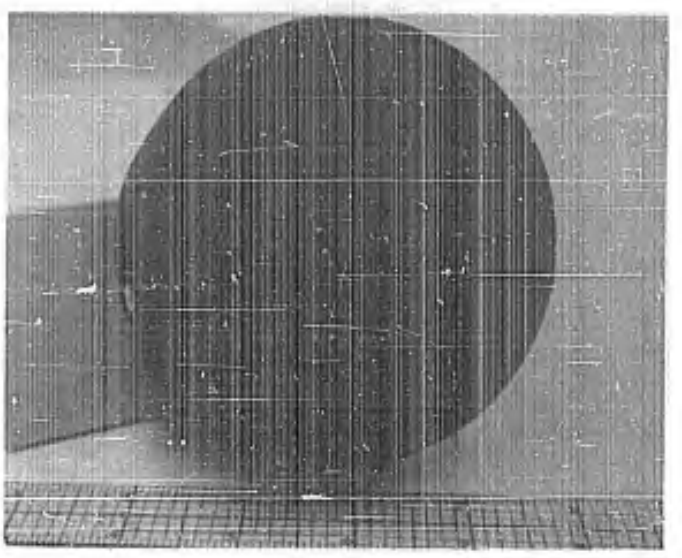

Figure 18: Unspiked Hemispherical Radome Before Tests

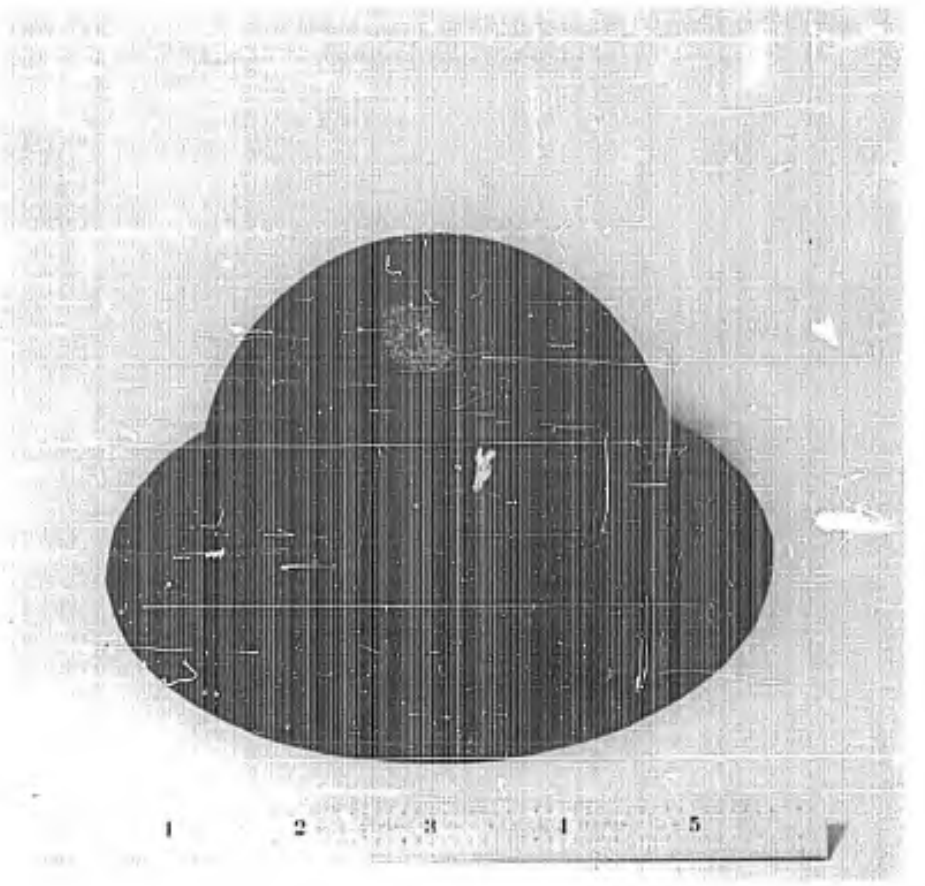

Figure 19: Unspiked Hemisphere After Tests

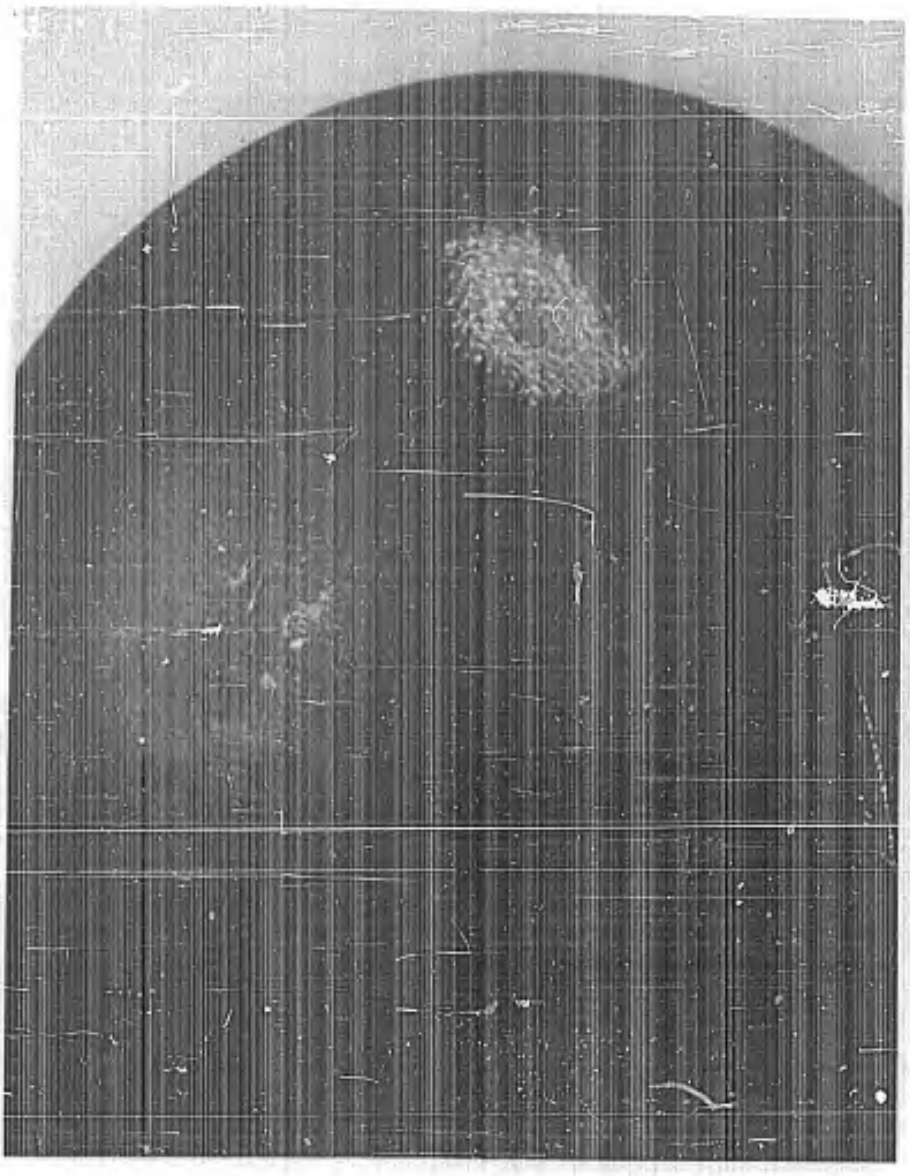

Figure 20: Unspiked Hemispherical Radome After Tests (Closeup)

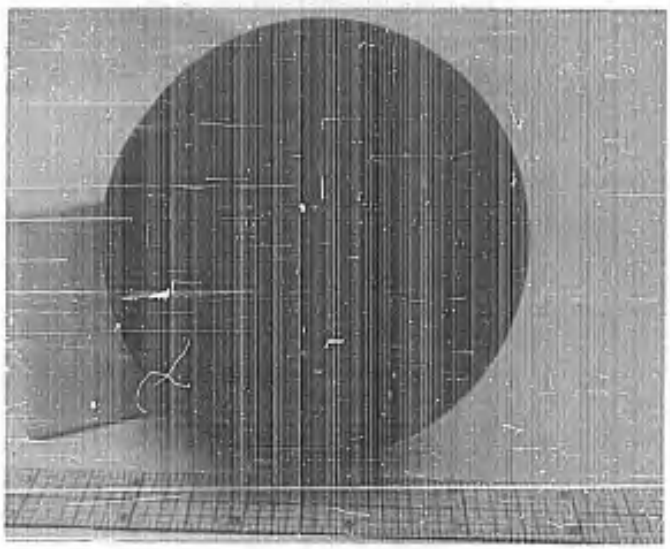

Figure 21: Spiked Hemispherical Radome Before Tests

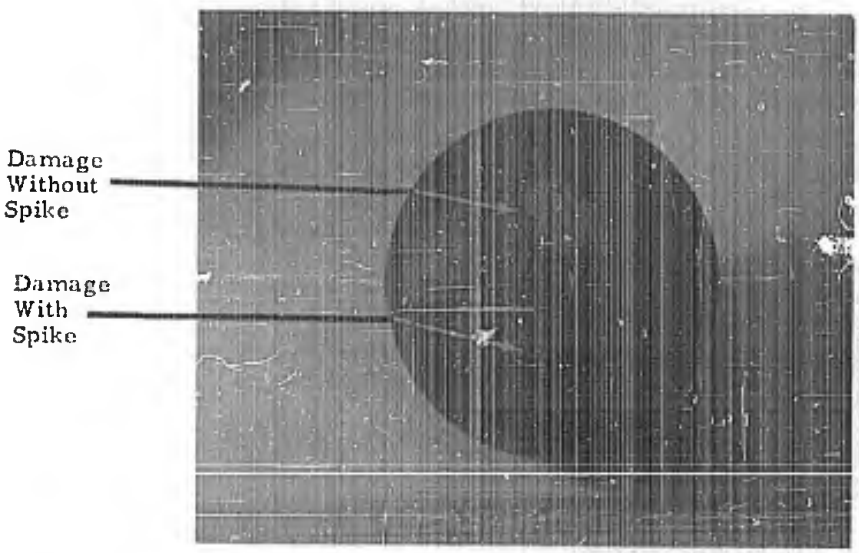

Figure 22: Model D2 After Tests

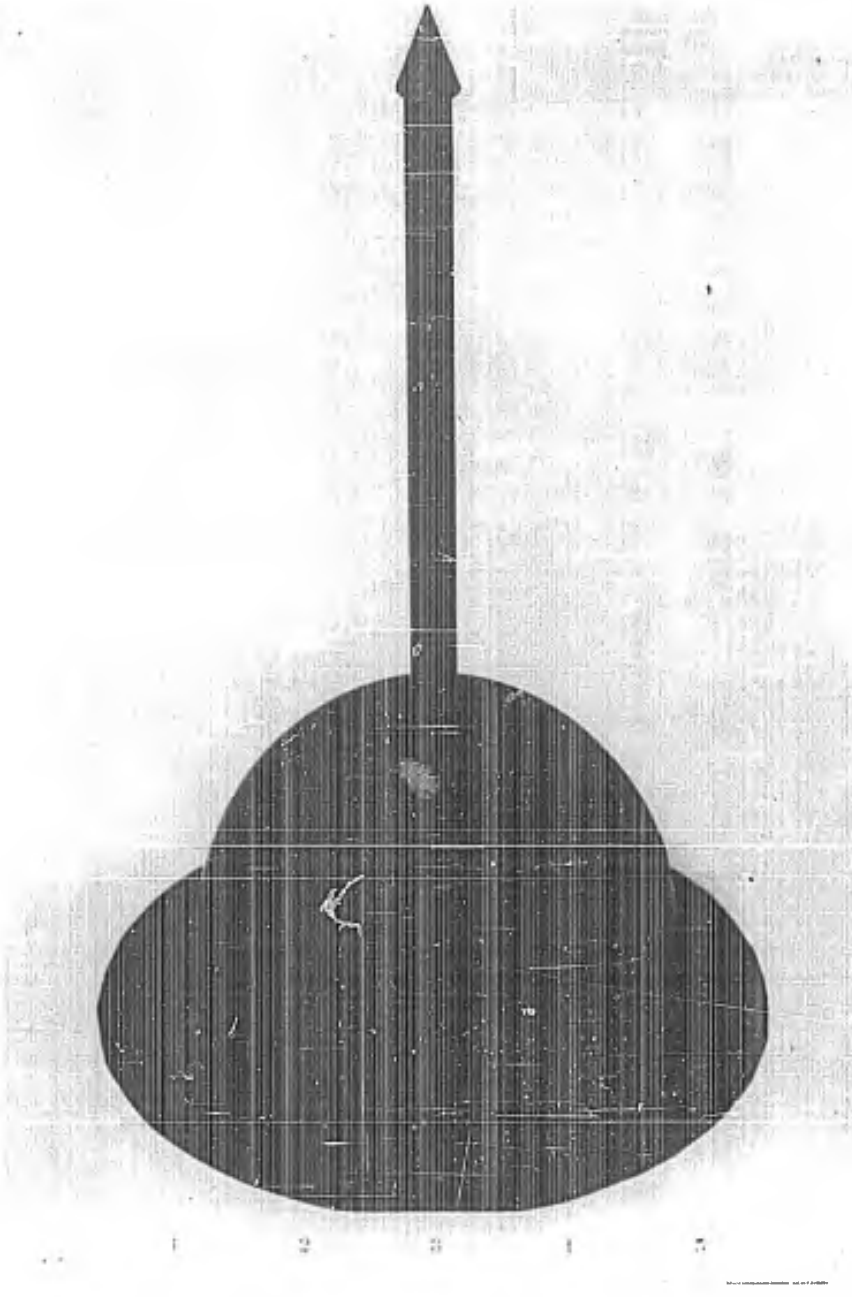

Figure 23: Spiked Hemispherical Radome After Tests

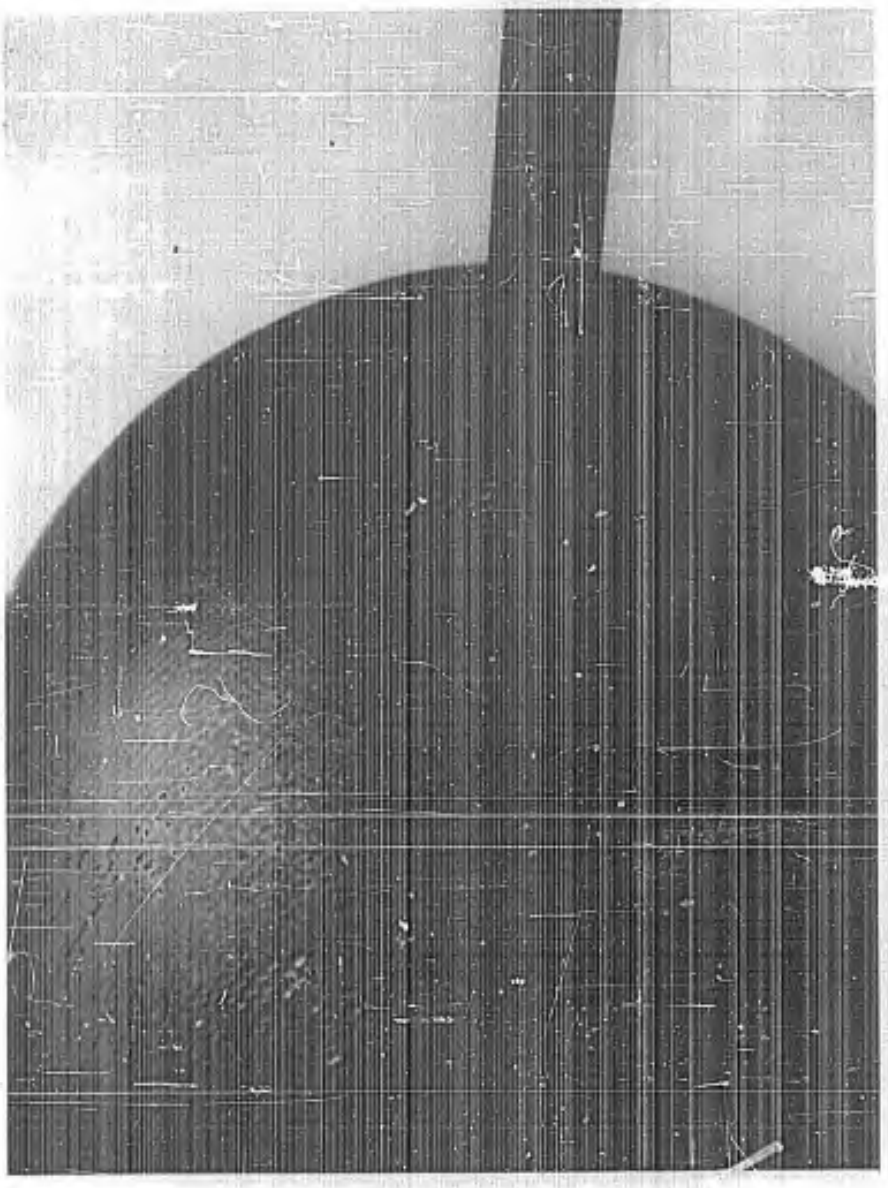

Figure 24: Spiked Hemispherical Radome After Test (Closeup)

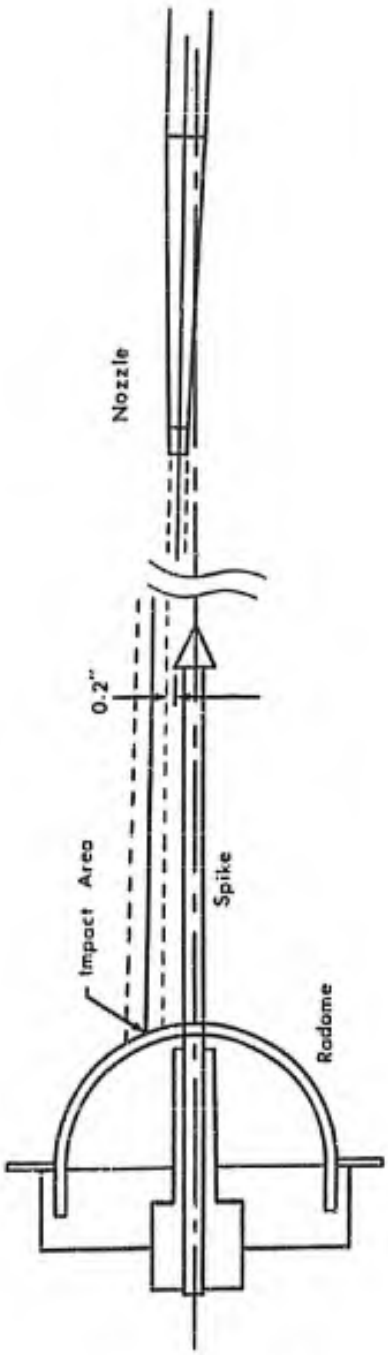

Figure 25: Water Jet and Spiked Dome Geometry

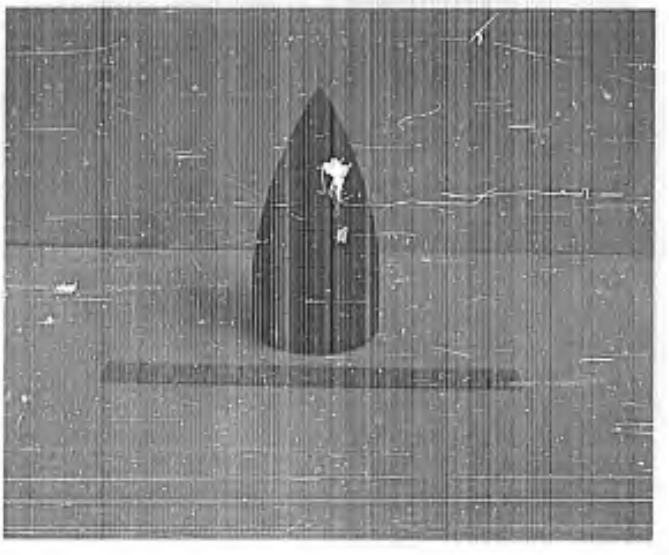

Figure 26: Ogival Radome Before Tests

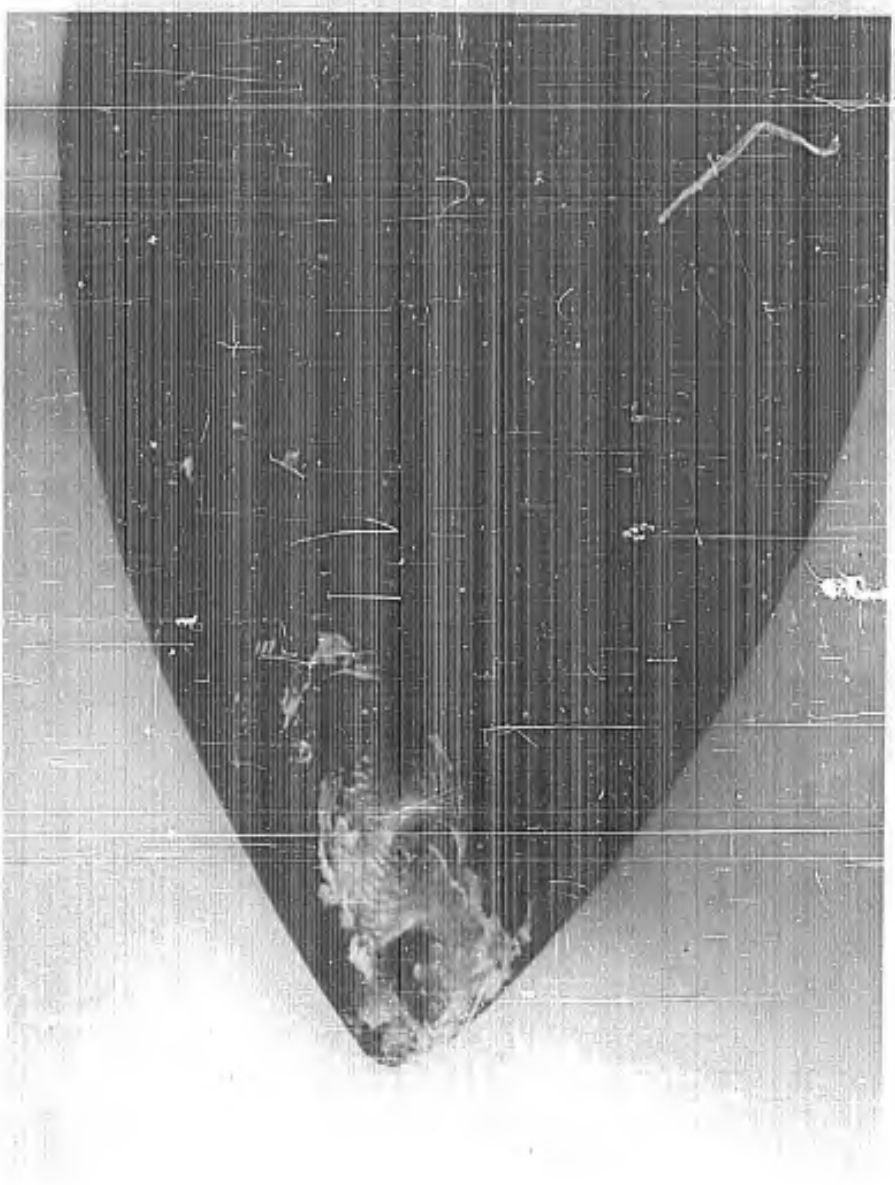

Figure 27: Ogival Radome After Tests (Model E1)

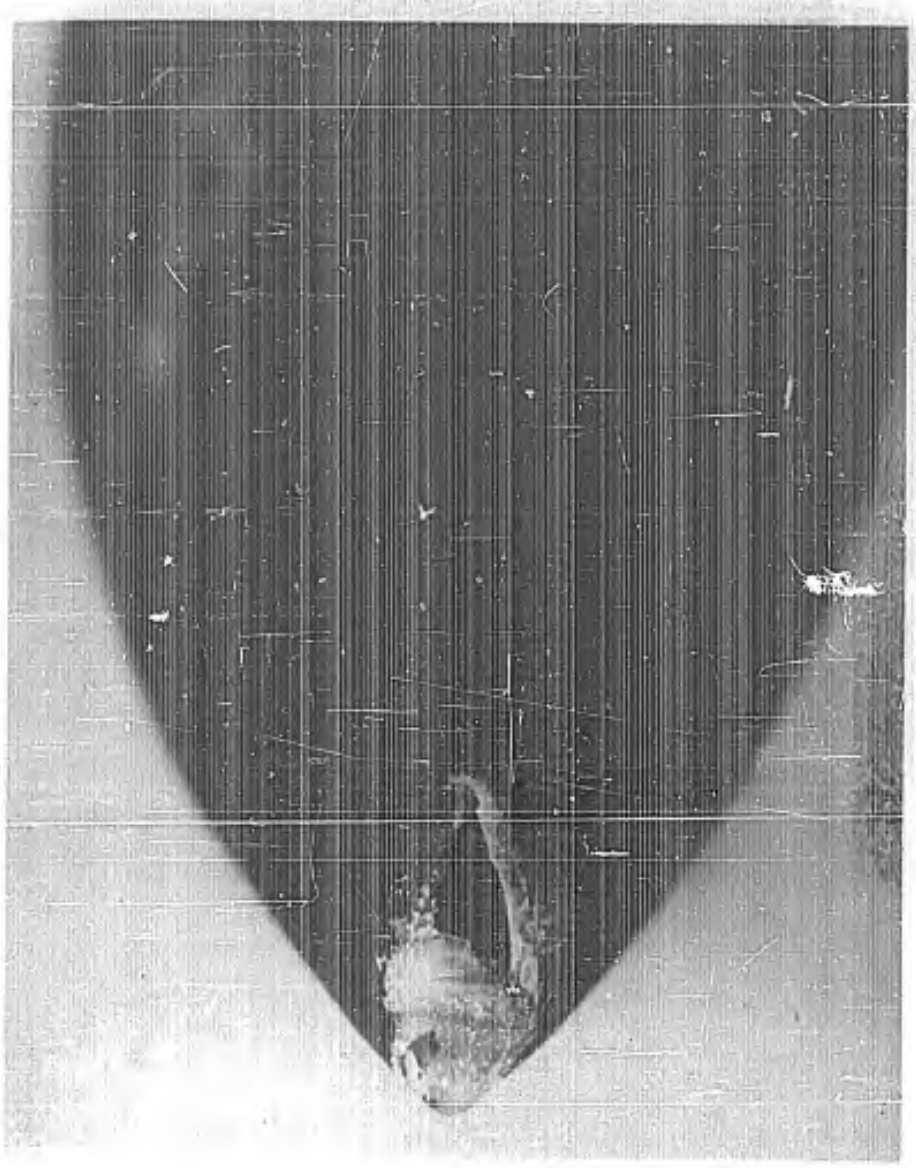

Figure 28: Ogival Radome After Tests (Model E2)

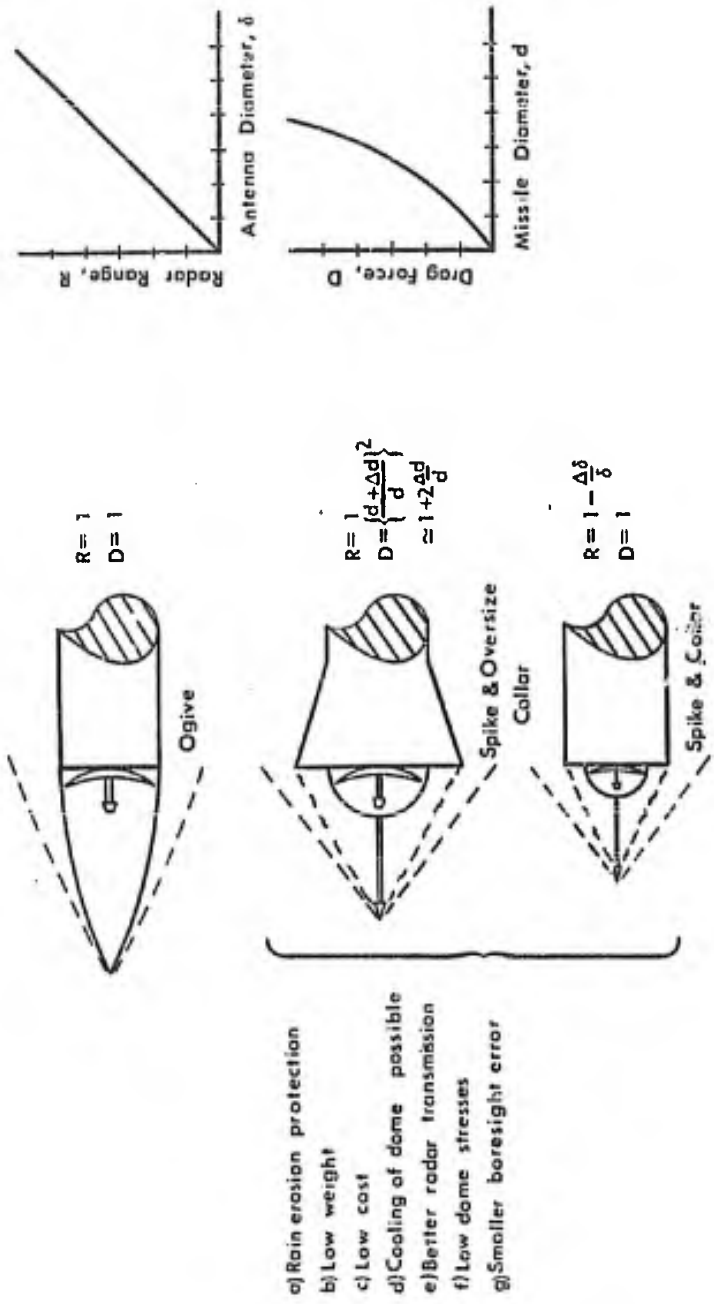

Figure 29: Spiked Body Configurations

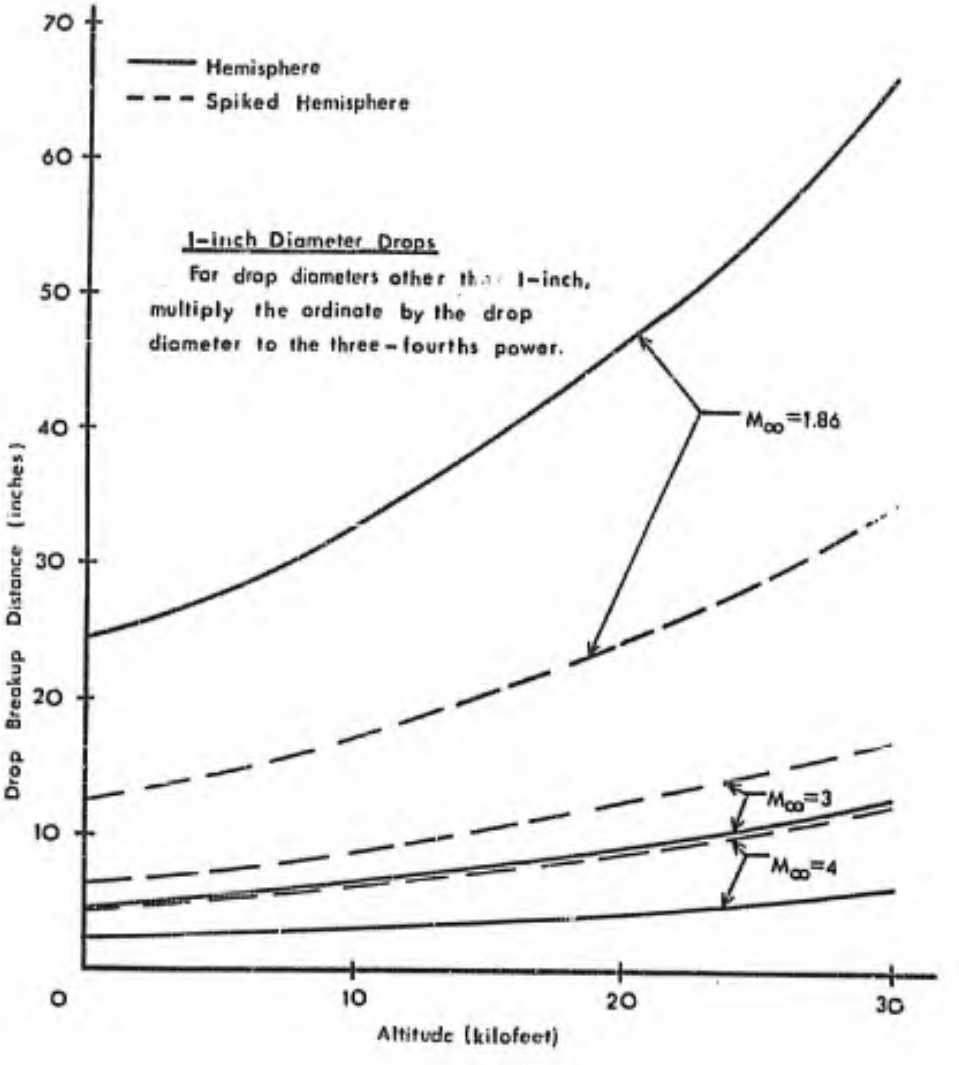

Figure 30: Drop Breakup Distance as a Function of Mach Number and Altitude

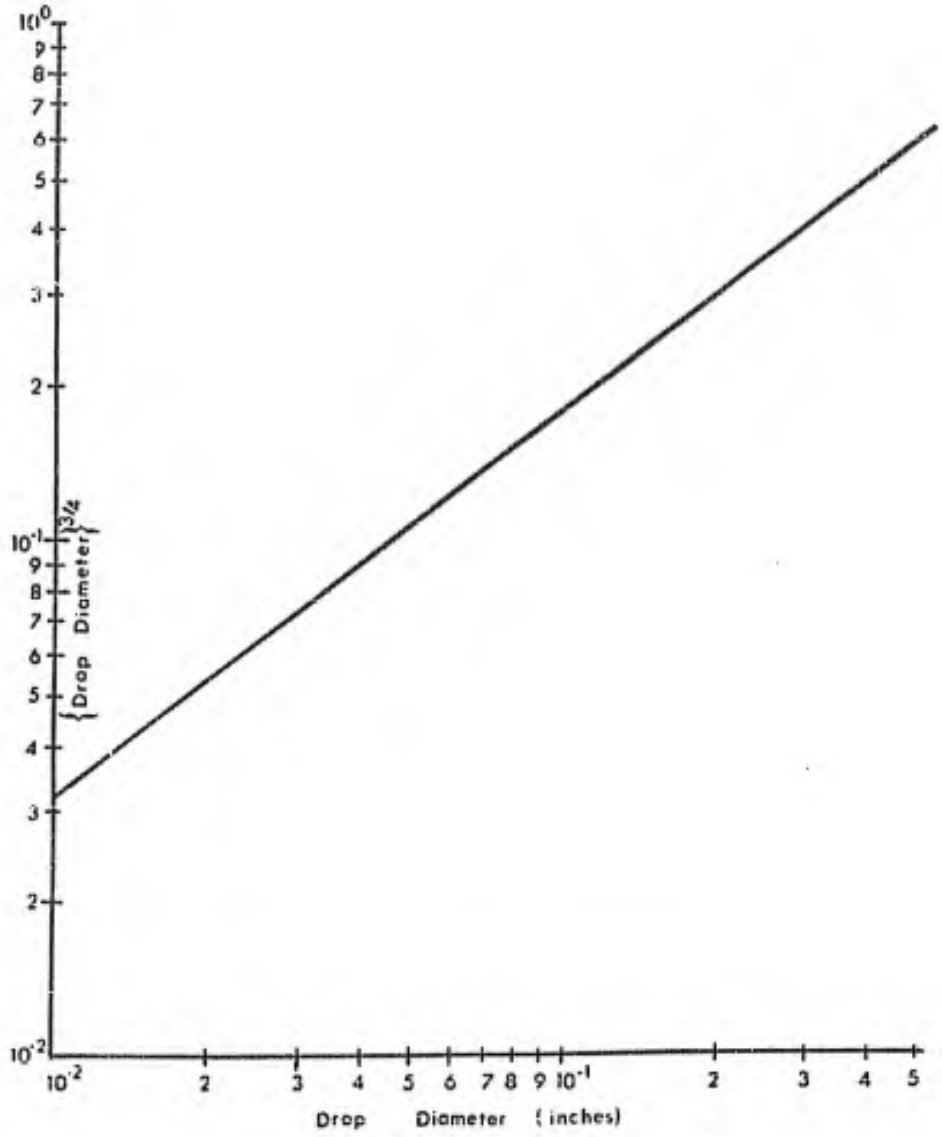

Figure 31: Drop Diameter to the Three-Fourths Power

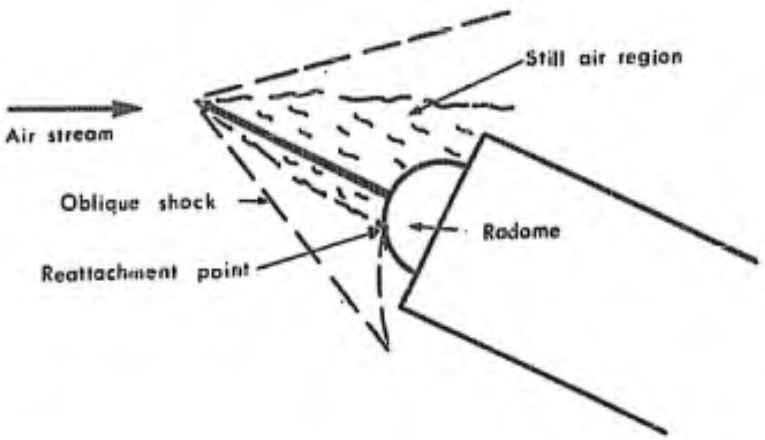

a) Fixed Spike

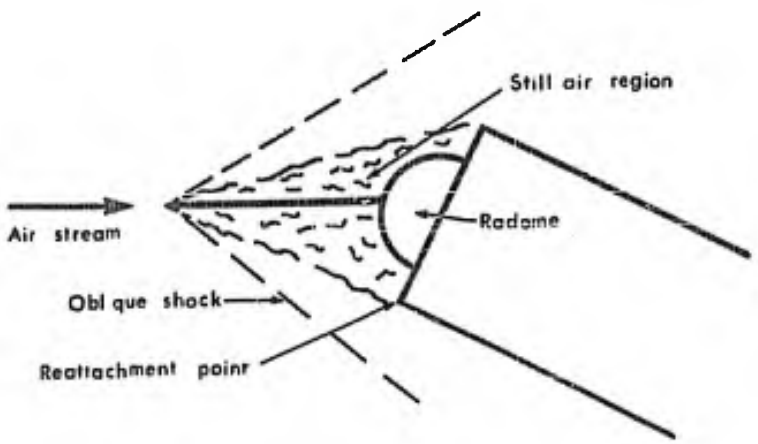

b) Angulated Spike

Figure 32: The Spiked Hemisphere at Angle of Attack

APPENDIX A

Equivalent Time of Flight Through Rain

A. 1 Terminal Velocity of Rain Drops

The water drag equation is

$$D = 1/2\ \rho_A\ V^2 S C_D \qquad \text{(A. 1)}$$

where D = Drag
ρ_A = Air density
V = Drop velocity
S = Drop cross sectional area
C_D = Nondimensional drag coefficient

At terminal velocity

$$W = D \qquad \text{(A. 2)}$$

where W = drop weight

Now for a spherical drop

$$W = mg = \rho_W 4/3\ \pi r^3 \qquad \text{(A. 3)}$$

where
m = drop mass
g = acceleration due to gravity
r = drop radius
ρ_W = water density

For a drop diameter of 1/8 inch and a C_D of 0. 5, we find for the terminal velocity

$$V_t = 30 \text{ ft./sec.} \qquad \text{(A. 4)}$$

A. 2 Mass Density of Rain

For a one-inch per hour rainfall rate, we will have falling on a one square inch area in one second

$$V_w = 2.78 \times 10^{-4} \frac{\text{cu. in}}{\text{in}^2\text{-sec}} \qquad \text{(A. 5)}$$

$$\frac{\dot{m}_W}{A} = \rho_W V_W = 3.17 \times 10^{-7} \frac{\text{sl}}{\text{in}^2\text{-sec}}$$

Using the mass flow equation

$$\dot{m}_W = \rho_R A V \qquad \text{(A. 6)}$$

where

$\dot{m}_W$ = mass rate of flow of water.

ρ_R = mass density of rain.

A = cross sectional area.

we can find ρ_R as

$$\rho_R = \frac{\dot{m}_W}{A V}$$

Taking A as 1 square inch and V as 360 in/sec. (30 ft/sec)

$$\rho_R = 8.81 \times 10^{-10} \frac{\text{sl}}{\text{in}^3}$$

A. 3 Equivalent Flight Time

The damage area on the fiberglass radomes was measured and found to extend primarily over a 1/2 sq. in. area. Taking a nominal velocity of 1000 ft./sec., the equivalent flight time through rain corresponding to one test run with the MITHRAS rain injection system can be found by equating the total masses of water that strike the eroded area. In the wind tunnel tests, this mass is found to be (See Figure E-8).

$$9.25 \times 10^{-3} \text{ slugs}$$

Equating this to the rain swept out over a one-half square inch area at 1000 feet per second in one-inch-per-hour rain, we have

$$M = \rho_R A V \Delta t = 9.25 \times 10^{-3} \text{ slugs}$$

and solving for the flight time, Δt

$$\Delta t = 1748 \text{ sec.}$$

or

$$\Delta t = 29.1 \text{ minutes.}$$

This value is obtained when the accumulator is charged with 0.5 liters of 2000 psi nitrogen. For the case where no nitrogen is used, the equivalent flight time through a one-inch-per-hour rainfall is found to be

$$\Delta t = 19 \text{ minutes at } 850 \text{ ft./sec.}$$

APPENDIX B

Estimation of Drop Size From Pit Depth Measurements

B.1 Introduction

Two papers by Dr. Olive G. Engel of the National Bureau of Standards on the subject of pitting of metal targets by impacting liquid and metal spheres are the basis of this appendix. These are:

1. Pits in Metals Caused by Collision with Liquid Drops and Soft Metal Spheres

   Engel, O. G., "Journal of Research of the National Bureau of Standards" 62 (6), June 1959, Research Paper 2958, pp 229-246

2. Pits in Metals Caused by Collision with Liquid Drops and Rigid Steel Spheres

   Engel, O. G., "Journal of Research of the National Bureau of Standards" - Applied Physics and Chemistry, 64A(1), Jan-Feb, 1960, pp 61-72.

The portion of these papers concerning drop impacts on metallic surfaces is of interest in that it allows the size of the impinging drop to be determined when the drop velocity, pit depth and physical properties of the liquid and metal are known.

B.2 Relation Between Pit-depth and Drop Size and Velocity

Experimentally, it is observed that, in general, when pit depth is plotted against relative collision velocity, a straight line with a velocity axis intercept results. Specifically, if the target has only edge support, the pit-depth-versus-velocity curve has an intercept on the velocity axis, but if the target is rigidly backed, the pit-depth-versus-velocity curve goes directly to the origin. The slope of the curve is found to be a function of the drop size.

Designating the pit depth by δ' and the relative velocity by V, we can represent the pit-depth-versus-velocity curve as

$$\delta' = K_1 V - K_2 \qquad \text{(B. 1)}$$

where K_1 and K_2 are constants.

Using a semi-empirical approach the slope, K_1, is found to be

$$K_1 = \frac{7.2}{1 + \left(\frac{c'}{c}\right)\left(\frac{\rho'}{\rho}\right)} \frac{d}{c} \qquad \text{(B. 2)}$$

d is the drop diameter
c is the speed of sound in the drop
c' is the speed of sound in the target
ρ' is the density of the target
ρ is the density of the drop

The speed of sound can be related to the mechanical properties of the material through the following relation:

$$c = \left[\frac{1 - \nu}{(1-2\nu)(1+\nu)} \frac{E}{\rho}\right]^{\frac{1}{2}} \qquad \text{(B. 3)}$$

where
ν is Poisson's ratio
E is Young's modulus

Combining equations (B. 1) and (B. 2) we get

$$\frac{\delta'}{d} = \frac{7.2}{1 + \left(\frac{c'}{c}\right)\left(\frac{\rho'}{\rho}\right)} \left(\frac{V}{c}\right) - K_2/d \qquad \text{(B. 4)}$$

K_2/d is a dimensionless intercept on the velocity axis. This quantity is more or less empirically found to be

$$\frac{K_2}{d} = \frac{136.8\ E'}{\rho^{1/2}\ \rho'^{1/2}}\ \frac{c\rho}{cc'\ c'\rho'} = \frac{136.8\ E'\ \rho^{1/2}}{c'^2\ \rho'^{3/2}} \qquad \text{(B. 5)}$$

where

E' is Young's modulus of the drop

The intercept velocity, i. e., the velocity at which δ'/d is zero given by

$$V_i = \frac{19E'\ (c\rho + c'\rho')}{\rho^{1/2}\ \rho'^{3/2}\ c'^2} \qquad \text{(B. 6)}$$

In evaluating E', the dynamic rather than the static value of Young's modulus must be used. The strength that should be used for E' is the dynamic yield strength in shear

Combining equations (B. 5) and (B. 6)

$$\frac{K_2}{d} = \left[\frac{19E'\ (c\rho + c'\rho')}{\rho^{1/2}\ c'^2\ \rho'^{3/2}}\right]\ \left[7.2\ \frac{\rho}{c\rho + c'\rho'}\right] \qquad \text{(B. 7)}$$

$$\frac{K_2}{d} = V_i\ \left[7.2\ \frac{\rho}{c\rho + c'\rho'}\right] = \left[\frac{V_i}{c}\ \frac{7.2}{\left(\frac{c'}{c}\right)\left(\frac{\rho'}{\rho}\right) + 1}\right]$$

Combining equations (B. 4) and (B. 7), we obtain

$$\frac{\delta'}{d} = \frac{7.2}{c\left[1 + \left(\frac{c'}{c}\right)\left(\frac{\rho'}{\rho}\right)\right]}\ \left[V - V_i\right] \qquad \text{(B. 8)}$$

or using a slightly different form

$$\frac{\delta'}{d} = \frac{7.2\,z}{c(z + z')} \left[V - V_i\right] \qquad \text{(B. 8a)}$$

where

$$z = c\rho$$
$$\text{and } z' = c'\rho'$$

The z's are known as the accoustic impedances.

Equation (B. 6) can be written as

$$V_i = \frac{19E'\,(z + z')}{(\rho c'\, z'^3)^{1/2}} \qquad \text{(B. 9)}$$

The following table contains values of the various mechanical and physical constants used in equations (B. 8) and (B. 8a). This table is contained in the first of Miss Engel's two papers. It is to be noted that the dynamic yield strength in compression is used for E' rather than the shear strength.

As an example of the use of equation (B. 8), let us plot drop diameter, d, versus pit depth, δ', in the case of water drops impacting a lead target. We find:

$$\rho = 0.99707 \text{ g/cm}^3$$
$$z' = 2.41 \times 10^6 \text{ g/sec - cm}^2$$
$$z = 0.1493 \times 10^6 \text{ g/sec - cm}^2$$
$$c = 1.497 \times 10^5 \text{ cm/sec}$$
$$c' = 2.128 \times 10^5 \text{ cm/sec}$$
$$E' = 4.324 \times 10^8 \text{ d/cm}^2$$

Material	Density, ρ (g/cm^3)	Speed of Sound, c (cm / sec)	Acoustic Impedance, Z ($g/sec\text{-}cm^2$)	Static Tensile Yield Strength, y (psi)	Dynamic Compressive yield strength, E' (d/cm^2)
1100-0 Aluminum	2.713	6.318×10^5	1.714×10^6	2,625 5,000	7.239×10^8
2024-0 Aluminum	2.768	6.370×10^5	1.763×10^6	12,625	1.183×10^9
Copper	8.92	4.691×10^5	4.184×10^6	3,975	2.394×10^9
Lead, Chemical	11.344	2.277×10^5	2.583×10^6		4.324×10^8
Lead, pig		2.128×10^5	2.414×10^6		
Steel, coldrolled	7.859	5.786×10^5	4.547×10^6		8.274×10^9
Iron	7.86	5.850×10^5	4.598×10^6		7.660×10^9
Zinc	7.14	4.170×10^5	2.977×10^6		
Mercury	13.546	1.451×10^5	1.966×10^6		
Water, 25°C	0.99707	1.497×10^5	0.149×10^6		

TABLE B.1 Physical and Mechanical Properties of Various Materials

CONFIDENTIAL

V_i can be computed and is found to be 1.21×10^4 cm/sec or 397 ft/sec.

Thus

$$\frac{\delta'}{d} = 2.82 \times 10^{-6} (V - V_i)$$

This relation is plotted in Figure B. 1.

B. 3 Drop Size Measurements

The diameters of the waterdrops produced by the high pressure water system were estimated by two different methods. First, drop diameters were measured directly from the run photographs. Second, the drop diameter was estimated by measuring the pit depth produced in the soft lead targets and then using the method of Sections B-1 and B-2 to infer drop diameter. Figure B-2 gives the normalized drop size distribution as estimated by both methods. Good agreement is obtained. The majority of drops are seen to have diameters in the range of .020 inches to .080 inches.

B. 4 Prediction of Water Drop Size

The final drop size resulting from the breakup of a water jet is given in Reference B-1 as:

$$X = \left[\frac{\sigma_w}{\rho_a V^2}\right] 0.60 \left[\frac{\mu_w V}{\sigma_w}\right]^{2/3} \left[1 + \frac{10^3 \rho_a}{\rho_w}\right] \left[\frac{D_j \rho_w \sqrt{v \sigma_w \mu_a}}{\mu_w^2}\right]^{1/6} \qquad (B-10)$$

where

x = final drop diameter.

σ_w = surface tension of the drop.

ρ_a = airstream density.

ρ_w = drop density.

V = relative velocity between jet and air.

D_j = jet diameter.

v = jet velocity.

μ_w = viscosity of drop.

μ_a = viscosity of airstream.

Using the following values:

$\sigma_w = 4.8 \times 10^{-3}$ lbs/ft.

$\rho_w = 1.94$ sl/ft.^{3}

$\mu_w = 1.42 \times 10^{-5}$ sl/ft-sec.

$\rho_a = 5.91 \times 10^{-4}$ sl/ft.^{3}

$\mu_a = 3.95 \times 10^{-7}$ sl/ft.-sec.

$D_j = 3.3 \times 10^{-3}$ ft.

$V = (1,600\text{-}v)$ ft/sec.

We can plot final drop diameter versus jetvelocity. Such a plot is given in Figure B-3.

When the measured values of drop diameter and velocity are compared with the predicted values, it is found that for a given velocity equation B-10 apparently underestimates the final drop size by an order of magnitude. It thus appears that Equation B-10 cannot be used in its present form to accurately predict final drop size resulting from the v er jet breakup.

B.5 REFERENCES

1 Weiss, M. A., Worsham, C. H. Atomization in High Velocity Air Streams. Esso Research and Engineering Company, Linden, New Jersey, NOrd 16706, Bumblebee Series, Report No. 277, May 1958 (U)

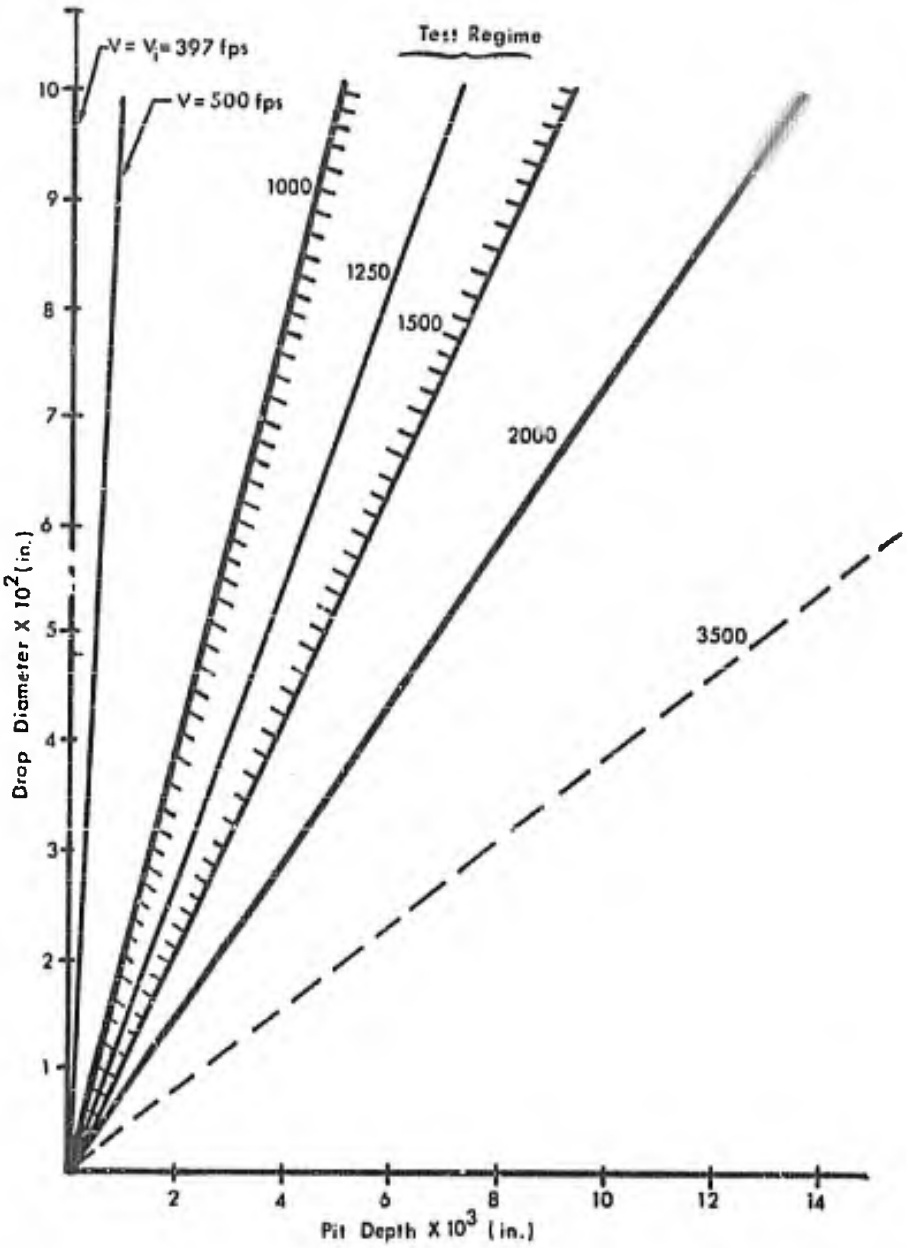

Figure B-1: Drop Diameter Vs. Pit Depth

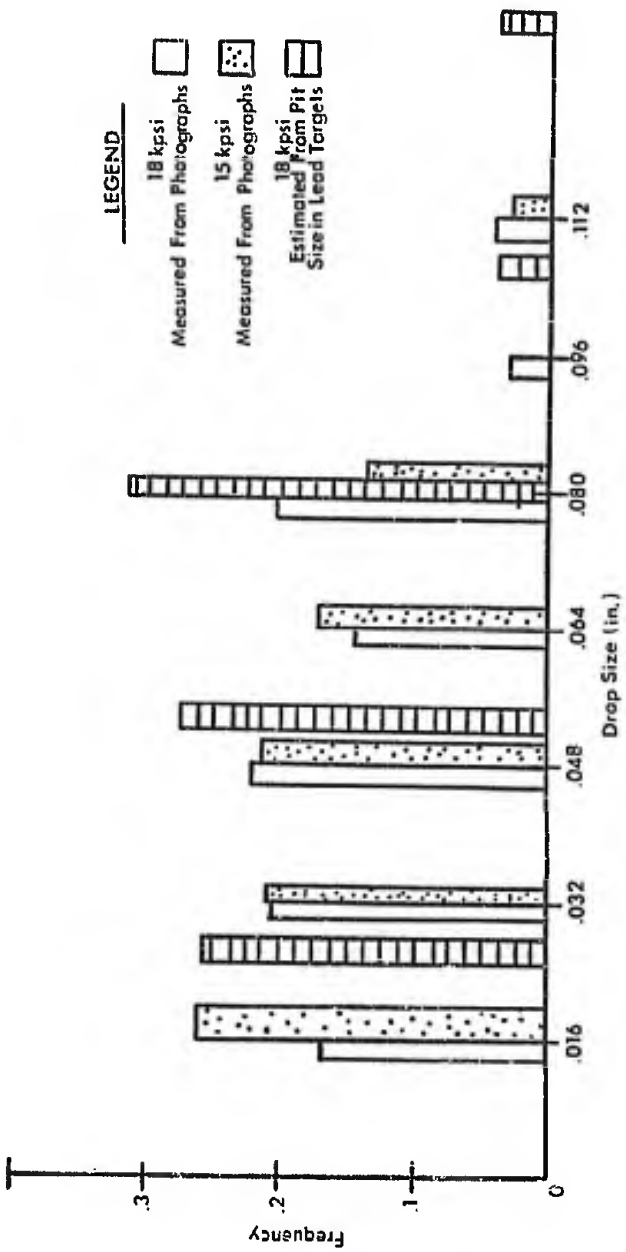

Figure B-2: Drop Size Frequency Vs. Drop Size

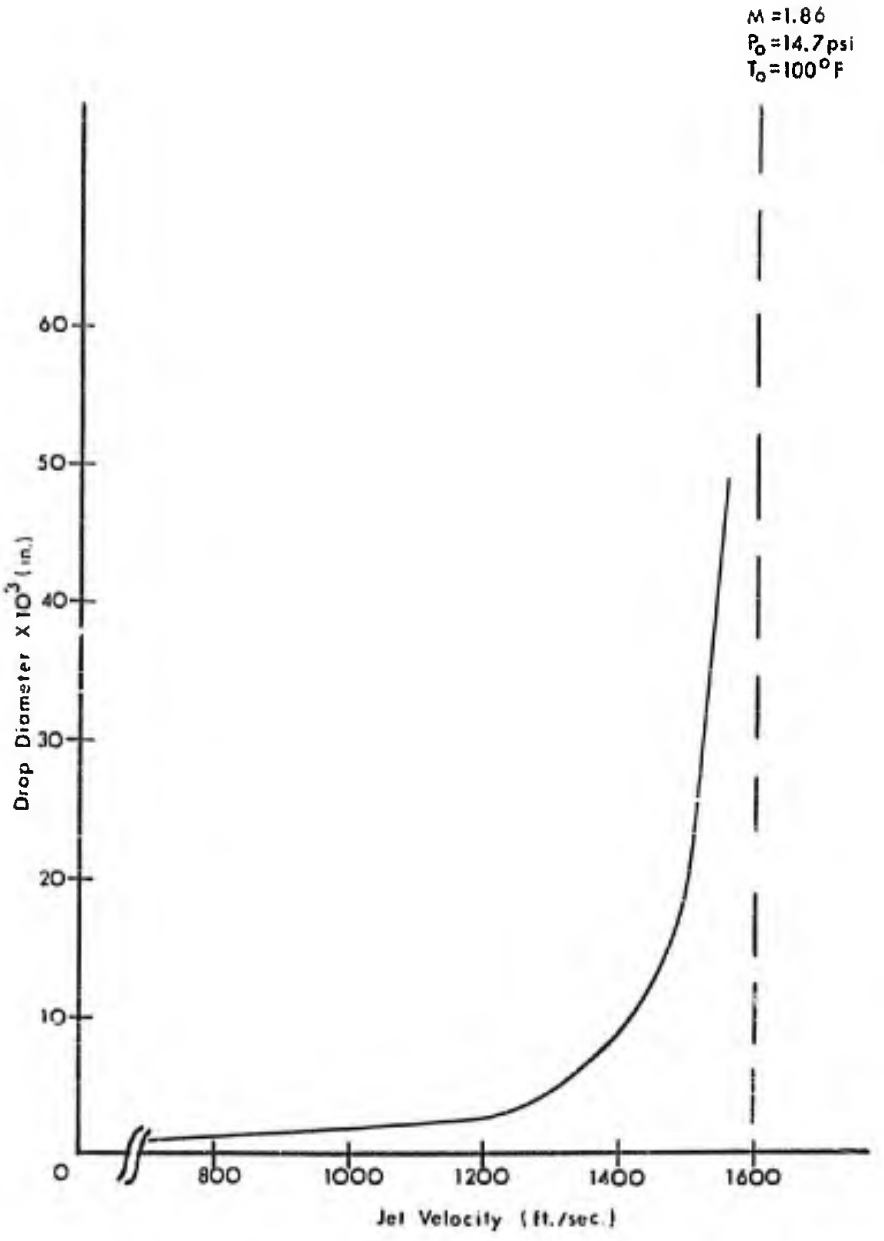

Figure B-3: Predicted Drop Size Vs. Jet Velocity

APPENDIX C

Drop Breakup Distance

C. 1 Drop Breakup Distance in Sleeved Model

The drop breakup equation as given in Reference 2 is

$$X_b = V_D\, t_b = \sqrt{\frac{a}{C_f}}\,\frac{D}{V_{rel}}\sqrt{\frac{\rho_w}{\rho_a}}\; V_D \qquad \text{(C-1)}$$

where

X_b = drop breakup distance.

V_D = drop velocity.

t_b = drop breakup time.

C_f = friction coefficient.

D = drop diameter.

V_{rel} = relative velocity between air and drop.

ρ_w = drop density.

ρ_a = air density.

and

$$a = \frac{1}{2}\left[\frac{\sigma}{q\ C_f\ D}\right]^2 \qquad \text{(C-2)}$$

where

σ = drop surface tension.

q = dynamic pressure of air on drop.

C_f is determined from Figure C-1 taken from Reference C-1. To use this figure, the Reynolds number of the drop must be found. This is given by

$$Re = \frac{\rho a \, V_{rel} \frac{\pi D}{4}}{\mu_a} \qquad (C-3)$$

where Re = Reynold's Number

μ_a = absolute viscosity of air.

For the sleeved model we find

$$\rho_a = 0.0558 \text{ lb/ft.}^3$$

$$V_{rel} = V_D = 1200 \text{ ft./sec.}$$

$$q = 1.25 \times 10^3 \text{ lb/ft.}^2$$

Using a drop diameter, D, of 0.050 inches and

$$\mu_a = 1.2 \times 10^{-5} \text{ lb}_m\text{/ft-sec.}$$

we obtain a Reynolds number of

$$Re = 1.83 \times 10^4$$

and a value for the friction coefficient of

$$C_f = 0.012$$

also

$$\sigma = 4.8 \times 10^{-3} \text{ lb/ft.}$$

thus, $a = 2.99 \times 10^{-3}$

and $\sqrt{\frac{a}{C_f}} = 0.5$

Finally $X_b = 0.850$ inches.

As indicated in Reference 2, Equation C-1 gives values that are at the lower end of the range of measured breakup distance. An upper limit on the breakup distance is on the order of four times the value given by Equation C-1. Thus the break-up distance can be expected to lie in the range

$$0.85'' < X_b < 3.40''$$

C.2 Drop Breakup Distance with Spiked Hemispherical Model

Employing Equation (C-1), with the gas conditions being those within the trapped air region, e.g., pressure equals equivalent cone pressure and the temperature recovery factor is approximately 60 percent,[5] we find, for M = 1.86, with D = 0.050" and σ = 4.8 x 10-3 lb/ft that

$$\rho_a = .0235 \text{ lb/ft}^3$$

$$V_a \simeq 0$$

$$V_{rel} = V_D - V_a \simeq V_D = 1200 \text{ ft/sec.}$$

$$\mu_a = 1.2 \times 10^{-5} \text{ lb}_m\text{/ft-sec.}$$

$$R_e = 8.31 \times 10^3$$

which gives

$$C_f = 0.0145$$

and $q = 525 \text{ lb/ft}^2$

thus $a = 0.0114$

and $\sqrt{\frac{a}{c_f}} = 0.888$

finally $X_b = 2.29$ inches

or, more practically, the breakup distance can be expected to lie in the range

$$2.29'' < X_b < 9.16''$$

C.3 Drop Breakup Distance Behind Tunnel Normal Shock

Employing Equation (C-1) once again with the ambient conditions being those behind a normal shock at M = 1.86, we find, using D = 0.050" and σ = 4.8 x 10^{-3} lb/ft. that:

$$\rho_a = .0467 \text{ lb/ft}^3$$

$$V_a = 676 \text{ ft/sec}$$

$$V_{rel} = V_D - V_a = 524 \text{ ft/sec.}$$

$$\mu_a = 1.21 \times 10^{-5} \text{ lb}_m\text{/ft.-sec.}$$

$$R_e = 6.63 \times 10^3$$

which gives $C_f = 0.0165$

and $q = 199 \text{ lb/ft}^2$

is $a = .062$

and $\sqrt{\frac{a}{c_f}} = 0.614$

finally $X_b = 8.06$ inches

or, more practically, the breakup distance can be expected to lie in the range

$$8.06" < X_b < 32.3"$$

C.4 Measurements of Drop Breakup Distance

The distance required to break up an oncoming waterdrop in a separated flow region can be written (derived in Reference 2).

$$X_b = \frac{\sigma}{q}\sqrt{\frac{\rho_W}{2C_f^3\rho_a}} \qquad \text{(C-4)}$$

where X_b = drop breakup distance

σ = surface tension of drop

q = dynamic pressure on drop

ρ_W = density of drop

C_f = friction coefficient between drop and airstream

ρ_a = density of air

For the sleeved model, this breakup distance is 0.85 inches. As explained, this computed breakup distance may be low by a factor of 4 so that the breakup distance can be expected to lie somewhere in the range of 0.85 inches to 3.40 inches.

An examination of the lead and brass targets used with the sleeved model indicates that good protection is afforded with sleeve lengths in excess of 2 or 3 inches. The lead target used with the 1.75 inch sleeve shows a significant reduction in erosion damage over the lead target with no sleeve. The thin brass target corresponding to a 1.75 inch sleeve, however, has been ruptured while the brass target used with a sleeve length of 3.50 inches has not been penetrated. A close examination of the lead targets employed tends to indicate that continued improvement in erosion protection is provided as the sleeve length is increased. However, as is readily apparent in Figure 16, the major part of the erosion protection is provided by the first two inches of sleeve. In addition to the two inches of sleeve that are effective, we must add on an additional 3/4 inch of stagnated air produced by the detachment distance of the normal shock in front of the sleeved model.

C. 5 REFERENCES

C. 1 Schlichting, H. Boundary Layer Theory. McGraw Hill Book Co., Inc., New York, 1954 (U)

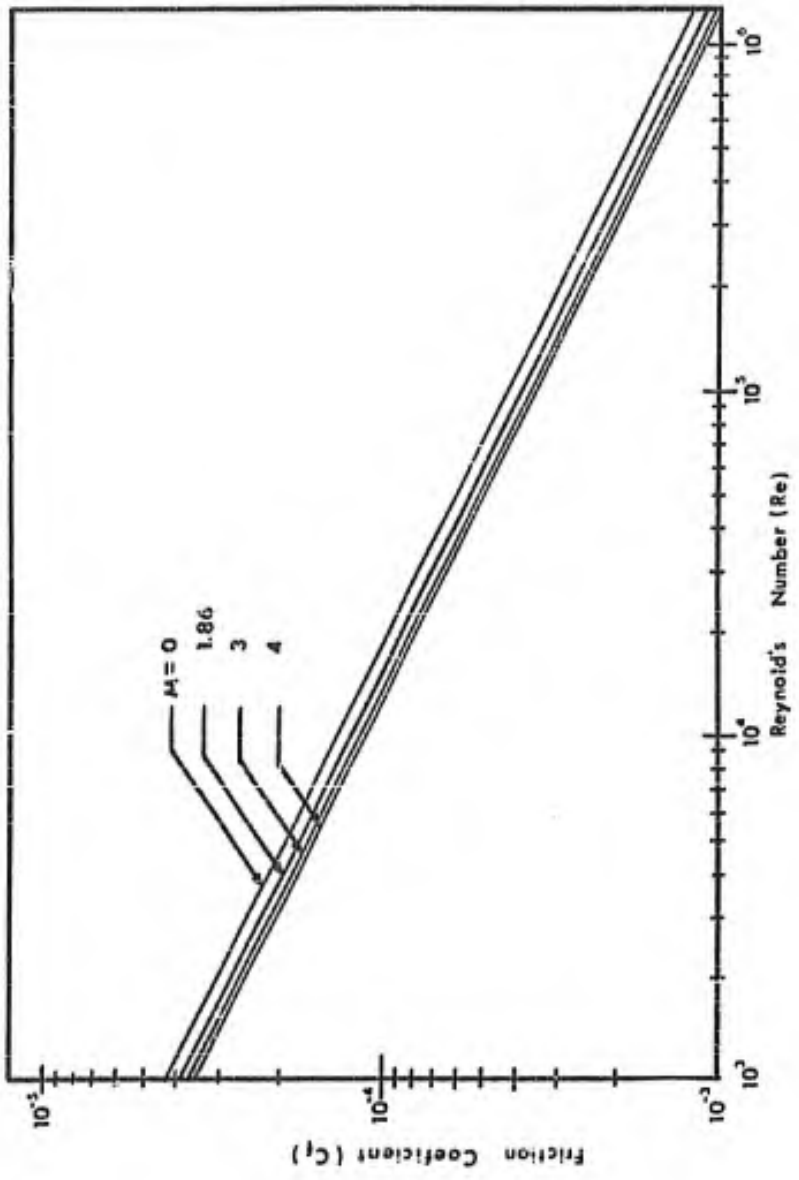

Figure C-1: Friction Coefficient Vs. Reynold's Number

APPENDIX D

Jet Breakup Distance

The jet breakup distance, i.e., the distance to turn the jet from a solid stream into a stream of drops, has been calculated by the application of the drop breakup equation (Equation C-1). It has been assumed that the airstream is at constant temperature, pressure, density and velocity. In actuality, such is not the case, since the airstream is accelerating in the region where the water is injected. The assumption of constant flow conditions will therefore result in an estimation of jet breakup distance that will be conservative, that is, it will overestimate the jet breakup distance.

The airstream flow parameters are:

$$p = 2.33 \text{ lb/in}^2$$

$$\rho = .0191 \text{ lb/ft}^3$$

$$T = 331^{\circ} \text{ R}$$

$$V_{air} = 1600 \text{ ft/sec.}$$

$$\mu_a = 10^{-5} \text{ lb}_m/\text{ft-sec.}$$

The jet parameters are:

$$D = 0.080 \text{ inches}$$

$$\sigma = 5.28 \times 10^{-3} \text{ lbs/ft.}$$

$$\rho_w = 62.4 \text{ lb}_m/\text{ft}^3$$

Thus,

$$Re = 3.99 \times 10^3$$

$$C_f = 2.5 \times 10^{-2}$$

$$a = 0.225$$

$$\sqrt{\frac{a}{C_f}} = 3$$

and finally,

$$X_b = 41.3 \text{ inches.}$$

In the tests conducted, it was found that at distances of 2 to 3 feet from the point of injection, the jet was broken up into water drops. The exact point at which breakup had occurred could not be determined however. It thus appears that equation (C-1) provides a conservative estimate of jet breakup distance. How much Equation (C-1) overestimates the jet breakup distance is not known.

APPENDIX E

Testing Equipment

A good deal of the equipment used during the tests at DTMB was used during MITHRAS' tests at M. I. T. one year earlier. However, considerable effort had gone into modifying and improving the system in the intervening year and it is felt, therefore, that a complete description of the equipment is in order even though some of the equipment was fully described in MITHRAS' report on the M. I. T. tests (Reference 2).

The equipment used at DTMB is logically divided into two major groups; the water injection system and the photographic system.

E. 1 Water Injection System

The water injection system is required to pump water to a pressure of up to 30,000 psi, store it, and then release it rapidly into a supersonic airstream at a velocity approximately equal to that of the airstream. The injection system is shown schematically in Figure 7.

E. 1. 1 High Pressure Pump

The pumping unit used is a Sprague* S-440 ready-to-use-pump unit with an S-216-C-300 basic pump. It is a "piston-type, air-operated, boost pump incorporating an automatically operated, snap action, air selection valve, "(E-1)". This pump develops high pressures through application of the principle of differential areas. The pump employs a large area piston, air-driven at a low pressure to drive a small area piston that displaces small fluid volumes at high pressures. The output pressure developed by the small area piston is determined by the ratio between the area of the driving piston, and the area of the driven piston, and the operating air pressure applied. The pump unit used had approximately a 300:1 piston area ratio. Thus when 100 psi air is

*Sprague Engineering Corporation, Gardena, California

used to operate an S-216-C-300 pump, the liquid pressure will be approximately 300 x 100, or 30,000 psi.

The basic pump unit was equipped with an air shut off valve, air line filter, air line lubricator, and an air line pressure regulator with gauge. The pump output pressure is read from a Marshalltown 30,000 psi gauge. This gauge has an accuracy of 1/2 percent of full scale, or 150 psi. The unit is seen in Figure E-1.

E. 1. 2 High Pressure Accumulator

The high pressure accumulator is a stainless steel cylinder with a two-liter capacity and is designed to operate with an internal pressure of 30,000 psi (proof tested to 45,000 psi). The unit has pressure fittings at both ends; the top fitting accommodates a nitrogen input system; the bottom fitting accommodates the water input and outlet systems. Figure E-2 illustrates the construction of the accumulator.

E. 1. 3 Quick Opening Valve

The quick opening valve is a modified Aminco Quick Opening Valve, type 44-5912. This unit is reported by the manufacturer to go from closed to full open in 4 to 5 milliseconds. This type of valve is held closed by a heavy spring which is compressed by a cam fastened to a long lever handle. This spring force seals the valve tight at pressures up to 50,000 psi. A slight angular movement of the handle opens the valve entirely, thus causing "instantaneous" release of pressure.

The Aminco valve body was modified by MITHRAS to allow the use of removable valve seats. This modification was prompted by the rapid wear of the permanent seats, thus necessitating frequent and expensive valve body replacement. To reduce turbulence of the flow in the valve body, the removable seat orifice diameter was increased over the unmodified valve body assembly. Figure E-3a shows the unmodified quick opening valve while Figure E-3b illustrates the modified valve body and replaceable seat.

E. 1. 4 Miscellaneous Hardware

The piping, valving, etc., of the system are standard Autoclave hardware (30,000 psi rated, stainless steel) and a description of these components may be found in References E-2 and E-3.

E. 1. 5 Water Injection Nozzles

Three different water injection nozzle contours were fabricated so that a range of water drop size could be obtained. The effect of the different nozzles could not easily be predicted, so final choice of the optimum configuration was based upon actual test runs under operating conditions.

The three nozzles were constructed of a five inch length of 1/4" x 0.083" stainless steel tubing silver soldered into a 10 1/2" length of 9/16" x 3/16" stainless steel tubing. A plug containing the nozzle contour was then silver-soldered into the tip of the smaller tube. The three nozzle contours are shown in Figure E-4.

The converging-diverging nozzle contour produced the most satisfactory drop size and was therefore used in a large number of the runs conducted to date.

E. 1. 6 System Operation

The operation of the water pumping system is as follows: (Referring to Figure 7).

With valves 5 and 12 closed, tap water is admitted from valve 6 and, after filtering, reaches the Sprague high pressure pump. With valves 1, 2, 4 and 11 closed and 3 open, the high pressure water on the outlet side of the pump is admitted into the 2-liter pressure vessel or accumulator. Valve 1 serves as a safety valve in the event of failure of valve 2 which is the special, quick-opening valve. By first opening valve 1 and then valve 2 the high pressure water in the accumulator is quickly released and after passing through a suitable nozzle, emerges as a high speed jet. In practice, valve 3 is closed prior to the opening of valve 2. This prevents the needle in the high pressure gauge from

slamming into its stop upon the sudden release of pressure in the system. Valves 4 and 12 serve the dual purpose of providing a bleed for the high pressure water and valve 4 is used in filling the accumulator with water. Valves 4 and 5 are permanently connected with a length of 1/4" copper tubing. To fill the accumulator with water, valves 2, 4, 5, 11, and 9 are opened permitting water to enter through valves 6, 5, 4, and 3 in that order. Valves 1 and 2, of course, remain closed. Displaced air escapes from the accumulator through valves 9 and 10.

Because of the small compressibility of water, only a small volume change is required to bring the water back to atmospheric pressure and the duration of the supersonic jet is therefore quite short. In many cases, it is required to have fairly long jet durations. This is possible if pressurized gas is used in the accumulator. This gas, because of its large compressibility, then serves as a spring and greatly increases the jet duration. For this purpose, provision is made in the water injection system for introducing 2, 300 psi nitrogen into the accumulator through valves 10 and 11. After valves 10 and 11 are closed, the system is then pumped up with water, compressing the nitrogen until the required pressure is reached.

Valves 7 and 8 are used to control the flow of 100 psi driving air into the pump and thereby controlling the pressure at the high pressure side of the pump.

E. 1. 7 Flow Properties of High Pressure System

The flow properties of the high pressure water system are described in Figure E-5 through E-8. Figure E-5 plots the system pressure loss as a function of accumulator pressure. Figure E-6 provides a curve of accumulator pressure versus time for an initial accumulator pressure of 15 kpsi. In Figure E-7 we have a curve of water velocity at the nozzle exit as a function of time, again for an initial accumulator pressure of 15 kpsi, and Figure E-8 gives a curve of gas volume in the accumulator as a function of time with an initial pressure of 15 kpsi.

In most of the test runs conducted at DTMB, the initial pressure

of the accumulator was 15 kpsi and the final pressure was normally 5 kpsi. From Figure E-6 and E-8, we see that the nominal volume of water ejected during a run was approximately 4.65×10^{-3} cubic feet. An average velocity over the total run time was therefore on the order of 1000 feet per second as can be seen from Figure E-7. Nominal run times were on the order of 0.5 seconds.

E.1.8 High Pressure System Check

The high pressure water system was prepared for use by completely filling the accumulator with water and then removing 1/2 liters of water. Nitrogen at a nominal pressure of 2000 psi was then introduced into the accumulator through valves 10 and 11. (See Figure 7.) Because the accumulator was never completely emptied of water during a run, the same volume of nitrogen could be used throughout the day providing that it is not necessary to de-pressurize the system.

The high pressure system, now under 2000 psi pressure, was then carefully inspected for leaks. The nitrogen supply was disconnected from the pumping system and the test area near the high pressure system was cleared of all unnecessary personnel.

Prior to actual test runs, the system was fired on the order of 3 to 6 times to clear the system of any debris which might have settled out after the previous day's runs. The pressure on each successive trial firing was gradually increased until the pressure to be used during actual testing was attained. During and after each trial firing, careful inspection of all joints and fittings was made to insure that no leaks were present in the system. On the final trial firing, the photographic system was operated to insure that it was in proper operating condition.

E.1.9 Safety Procedures

The high water pressures developed in the water system necessitated certain safety procedures. The entire pumping assembly was surrounded by two layers of 3/4" plywood, with the exception of a 8" x 10" x 3/4" thick lucite viewing port to read the high pressure gauge. Only one person was needed to operate the pumping system, and all other

personnel were restricted to the front side of the tunnel during test runs. A double thickness bullet-proof glass barrier was placed between the pumping equipment and the remaining personnel as an additional safety precaution.

A safety valve was placed between the quick opening valve and the water nozzle so that a failure or leakage of the quick opening valve would not mean sudden release of water pressure into the tunnel possibly while personnel were conducting a model change. This safety valve was always closed except during an actual run.

In the interest of safety, the glass face of the high pressure gauge was removed and replaced with a thin celluloid sheet. This was done to prevent the breaking of the glass face in the event of a gauge failure.

The high pressure pumping system was situated between the wind tu el and a large cement column. (See Figure E-9.) The pump operator was stationed behind this column to prevent injury in the event of system failure. It was necessary for the operator to expose himself only when releasing the quick-opening valve.

E. 2 Photographic System

The photographic system is used to determine the velocity of the water drops in the supersonic airstream and to measure drop size.

The system (Figure E-9) consists of two cameras, two electronic flash units, two electronic time delay circuits, (built as one unit) a trigger circuit, and a flash monitoring circuit.

This arrangement was used in order to obtain two individual silhouette photographs of the subject with a known time interval between each exposure. The images are separate, distinct photographs rather than the conventional superimposed double exposure technique. The cameras, light sources, light baffle, and translucent screen are arranged in a manner that allows the No. 1 camera to receive illumination only from the No. 1 light source, and the No. 2 camera to receive light from the No. 2 light source. (See Figure E-10.)

E. 2. 1 Cameras

The cameras used are conventional "Speed Graphic" 4 x 5 press cameras. The shutters are solenoid operated from a single cable and are normally set for 1 second exposure at f/8 (the f/ number required is determined by the flash units and the film type). ASA 3000 speed Polaroid 4 x 5 film is normally used. The two cameras are mounted, one above the other, on an aluminum column which is in turn mounted on a conventional camera tripod (see Figure E-10). As used, the camera and film give an experimentally measured static resolution of 0. 005 inches at a 22. 5 feet distance.

In addition to the cameras used to record the test sequence, another camera is used to photograph the oscilloscope face during a run in order to determine the time of firing of the two flash sources. This camera is a conventional Tektronix oscilloscope camera that uses Polaroid type roll film. This camera was also operated at a 1 second exposure at f/8. Its shutter was tripped in coincidence with the shutters of the two speed graphic cameras.

E. 2. 2 Light Sources

The MITHRAS designed light sources are two separate 0. 2 watt-second energy units with a flash duration of approximately one microsecond. Figure E-11 shows the circuit diagram of the units. Provision is made for firing the lights either by making or breaking of the circuit; hence the multiple input jacks of Figure E-11. Firing pulses to the units are provided by the trigger circuit and delay circuit unit. As shown in Figure E-10, the two sources are mounted in a plywood light box. The two light sources are separated by a plywood light baffle, to insure that the light from flash unit number one does not reach camera number two and vice versa. A diffusing screen, made of drafting vellum is mounted in front of the two units to provide uniform backlighting for the water drops in the tunnel.

The flash duration of the light source was originally on the order of ten microseconds. This was found to be too slow for the requirements

of the test program and the flash duration was therefore reduced to approximately one microsecond. Figure E-12 is a reporduction of the time history of the flash intensity as a function of time. The flash time histories were obtained by monitoring the light flashes with a 929 phototube and then displaying the phototube signal on an oscilloscope, from which the traces in Figure E-12 were obtained. As is evident from Figure E-12, the flash duration of the two units is approximately one microsecond.

E. 2. 3 Trigger Detector

The function of the trigger detector circuit is to sense when the stream of water or drops has emerged from the water injection nozzle and to send a signal to the trigger circuit and delay circuit unit which will in turn fire the two flash units at the correct instants of time.

The trigger circuit is actuated when the water jet intercepts a light path across the tunnel between the trigger detector light source and the trigger detector. (See Figure E-9 for the arrangement of detector and light.) The trigger detector light source is a #47 pilot lamp. The lamp voltage is full wave rectified and R-C filtered to reduce the ac component to negligible levels (the trigger detector circuitry is designed to operate on the signal variation rather than signal level). A variable resistor in series with the #47 bulb is used to control the lamp intensity. Figure E-13 shows the lamp power supply. (In practice, best performance was obtained with the lamp intensity at a minimum).

The trigger detector circuit is shown in Figure E-14. The sensor is a lead sulfide detector followed by a four-stage vacuum tube amplifier. The detector and amplifier are housed in one case (Figure E-15). Gain control is provided between the first and second amplifier stages. The circuitry is such that output depends not on signal level but on the rate of change of signal level, i. e., the sensor signal is differentiated. This was done to suppress the effects of varying ambient lighting. Because of the high velocity of the water jet or drops, the interruption of the light beam occurs quite rapidly giving rise to a large signal from the trigger detector circuit.

The #47 lamp is imaged on the detector by a single lens to provide optical gain for the system.

E. 2. 4 Trigger Circuit and Delay Circuit

The trigger circuit and delay circuit is illustrated in Figure E-16. The signal from the trigger detector is first passed into a 2D21 thyratron which produces a pulse output. The output signal is split, one part being used to trigger the oscilloscope through the scope's external sync circuit and the second part feeding into the first time delay circuit. Here the signal passes through a one-shot-multivibrator and two stage amplifier with a variable delay circuit. Coarse adjustment of the time delay is provided by means of switching in one of a series of capacitors and fine adjustment of the time delay is provided through the variable resistor. The delayed signal then passes through a 2D21 thyratron where a sharp pulse is produced. This signal is split into three parts, one part feeding the upper beam of the oscilloscope and the second part, after passing through one stage of a 6SN7 triode, feeding the number one flash unit. The triode is utilized to isolate the scope from the flash unit. The third part of the signal is fed into a second time delay circuit, identical to the first. The output signal from this second delay unit is split into two parts, one part being fed differentially to the upper beam of the oscilloscope and the second part to the number 2 flash unit.

Both time delays, the first giving the time interval from the trigger signal to the first flash and the second delay giving the time interval between the first and second flashes, are adjustable over a range of 10^{-5} seconds to 1 second. The upper beam trace is initiated when the trigger circuit pulse arrives and shows a positive pulse when the first flash signal is produced followed by a negative pulse when the second flash signal is produced. (See Figure E-17 for a typical oscilloscope photograph of the beam traces.)

The oscilloscope used is a Tektronix type 551 Dual-Beam Oscilloscope with two type D plug-in amplifiers. Triggering of the oscilloscope is accomplished through the external sync input. The scope has an optional single sweep feature which prevents multiple sweeps from

occurring and this mode of operation was used. The upper beam was fed differentially from the two flash unit signals while the lower beam was fed from the flash monitor circuit. Both the upper and lower beams were a. c. coupled.

E. 2. 5 Flash Monitor System

Because of the inherent delay between the occurrence of the flash unit signal and actual firing of the flash unit a flash monitor system was built to determine the actual firing times of the two flash units. The circuit for this unit is shown in Figure E-18. The system employes a type 929 phototube as the detector and the output signal requires no amplification prior to its being fed into the lower beam of the oscilloscope. Figure E-17 shows the upper and lower beam traces of a typical firing sequence. The delay between the firing signal to the flash units and the actua 'iring of the units is found to be on the order of 10 microseconds or less.

E. 2. 6 Photographic Calibration

At the beginning of each day of testing, the photographic equipment was calibrated. This was accomplished by placing a graduated rule along the wind tunnel centerline and photographing the rule with each camera to obtain the proper scale factor to use when analyzing the photographic results.

E. 3 Test Models

Four basic model configurations were utilized for the DTMB tests. These configurations were:

1. Sleeved models, with and without sleeve (Figures E-19a and E-19B respectively). These models were utilized to investigate the drop breakup process in a region of high relative velocity between the drops and the air and also to determine the protection afforded by such regions against raindrop penetration.
2. Flat faced models, with and without spike (Figures E-20a and E-20b respectively). These models were utilized to

study the effectiveness of a flow separating spike in affording protection against rain erosion damage.

3. Hemispherical radomes, with and without spike (Figures E-21a and E-21b respectively). These models were utilized to demonstrate the protection that was afforded to radomes equipped with a flow separating spike as compared to an identical radome without the spike.

4. Ogival Radomes. These models were employed in order to provide a comparison betwen the damage produced on a streamlined radome, in this case, an ogive, with the rain erosion damage produced on spiked and unspiked hemispherical radomes. The ogive dome is shown in Figure E-22.

The model support system in the DTMB tunnel allowed axial traversing of the models over a 15 inch range, thus permitting the determination of the optimum target-to-water-injection-nozzle distance. The support system also had the capability of vertical and horizontal movement, but all models were kept on the tunnel center line. No angle-of-attack variation was permitted with the model support system used.

E. 3. 1 Sleeved Model

The sleeved model is illustrated in Figure E-23. This model was nearly identical to the model used during the MITHRAS rain erosion tests at M. I. T. 's Gas Turbine Laboratory one year earlier (See Reference 2 for details of these tests). This model could either be used with the plexiglass sleeve in place to study the effect of a stagnated air region in front of the target, or else the model could be used without the sleeve and except for the effect of the relatively thin stagnation region between the bow shock and the model, the effect of the impinging water on an unprotected model could be studied.

The length of the plexiglass sleeve could be varied at will by simply cutting off slices of the plexiglass tube. The targets used with this model were 0.003" and 0.005" thick brass shim stock and 1/16" thick,

dead soft, polished lead. The targets were backed by a soft commercial children's clay to provide some support against aerodynamic loads, particularly during tunnel starting. The rest of the loading was taken up through edge support provided by the target support. The clay backing, because of its plasticity, did not impair target indentation upon water drop impact. The model was 1 3/16" in diameter and the plexiglass sleeve was 1 3/4" o.d. x 1 1/2" i.d.

By comparing the damage to targets using the plexiglass sleeve and those without the sleeve, it is possible to determine, in a qualitative sense, the effectiveness of a flow separation region in breaking up water drops. By varying sleeve length, it is possible to determine the effect of the length of the separated flow region on the drop breakup process.

E 3.2 Flat Faced Model

The flat faced model is in many ways similar to the sleeved model. As shown in Figure E-24, it has a target support arrangement, identical to the sleeved model, but it is more than twice the diameter of the sleeved model. Clay backing is used with this model to provide part of the target resistance to the applied aerodynamic loads, while the remainder of the applied forces are taken up through edge support. The outside diameter of the model is 4.00". The target materials were 0.003" and 0.005" thick brass shim stock and 1/16" thick, dead soft, polished lead.

A steel spike, 1/4" in diameter, tipped with a cone of 1/2" base diameter by 5/8" length could be extended upstream of the model as shown. This spike could be extended up to 12" in front of the target.

This model was used to investigate the protection afforded by flow separating spikes to radomes. Comparisons of damage to spiked and unspiked models is readily obtained and the effect of spike length on the amount of erosion damage can be determined.

E. 3. 3 Hemispherical Radomes

Figure E-25 shows the details of the fiberglass radomes and

their mounting arrangement. Two of the domes had a 1/4" diameter hole drilled through the forward point of the dome to accommodate the flow separating spike as illustrated in Figure E-25. The two remaining domes were not provided with these holes.

The radome models were provided with a series of aluminum collars of 4 1/2", 5 1/2", and 6 1/2" diameter which could be attached to the model at the hemisphere shoulder. The collar is utilized to provide a reattachment point for the boundary layer which separates from the spike. Since the pressures and temperatures at this reattachment point are normally quite high, it is important, in application to insure that reattachment does not occur on the radome itself. In practice, this is accomplished by making the radome with a diameter smaller than the missile body diameter as illustrated in Figure E-26.

The three collar diameters were provided in order that the largest diameter model might be used without choking the DTMB wind tunnel. As shown in Reference 5, at M = 1.86, a L/D ratio of 1.4 to 1.5 (where L is measured from the collar face) was the maximum that could be expected to maintain the boundary layer separation off the spike tip. For the purposes of rain erosion protection, it was desirable that a maximum spike length be used and hence the requirement on maximum model diameter (since maximum permissible spike length is proportional to body diameter). It was found that both the 4 1/2" and 5 1/2" collars could be used without choking the wind tunnel. The 6 1/2" collar, however, did block the tunnel. Therefore, the 5 1/2" diameter collar was utilized for all tests of the spiked hemispheres.

The radomes were molded from fiberglass cloth and polyester resin by the Naval Air Development Center, Johnsville, Pennsylvania. The hemispheres were four inches outside diameter with a 5/8" cylindrical portion extending aft from the dome shoulder. The cylindrical portion was used for attaching the domes to the mounting plate. Nominal radome thickness was 0.050". The mounting plate was provided with four 1/4" bleedholes for equalization of pressure on both sides of the radome. The spike was 1/4" diameter with an arrowhead tip. This spike tip

measured 1/2" diameter at the base by 5/8" long. The spike length was adjustable from 0" to 12" (measured from the radome face).

The unspiked hemispherical models were used without any collar. The mounting arrangement, however, was identical to that of the spiked hemispheres.

The thickness of the aft 1 1/32" of both the spiked and unspiked hemispheres was increased to 0.090" for structural reasons. This portion of the domes was not used for water drop impact studies during the rain erosion tests.

E. 3. 4 Ogive Radomes

Two ogive radomes were also molded by NADC, Johnsville, Pennsylvania. The domes were of the tangent ogive type. Their base outside diameter was four inches with a 5/8" long cylindrical section following the ogive portion of the dome. This 5/8" cylindrical portion was used for attachment to the mounting plate. The radius of curvature of the ogive was 12" corresponding to a 3-caliber ogive. Figure E-27 shows the details of the ogive model.

The mounting arrangement of the ogives was in every way identical to that of the hemispherical domes. No spikes or collars were employed with the ogives. The nominal wall thickness of the domes was 0.050" except at the nose and the aft 1 1/2" of the dome. The thickness of the final 1 1/2" of the dome was increased to 0.090" for structural reasons. This area was not utilized during the rain erosion portion of the test and the added thickness therefore had no effect on the rain erosion resistance of the dome.

The nose portions of the domes, approximately 3/4" in length, were found by NADC to have not bonded quite properly. NADC therefore filled in the tips of the radomes, to a depth of roughly 3/4", with epoxy. This in effect, provided the domes with solid tips and consequently resulted in domes with tip portions that had an inherent rain erosion resistance built in. Since these domes were to be compared with the hemispherical domes after being subjected to water drop impacts, the reinforced tips

meant that the ogives would possess the advantage of thicker material in the region of drop impact damage and should consequently have been more resistant to the erosion damage.

E. 4 REFERENCES

E. 1 Sprague Hydraulic and Pneumatic Equipment Bulletin No. 255 (Rev. B). Sprague Engineering Corporation, Gardena, California (U).

E. 2 Autoclave 30,000 psi Valves and Fittings Bulletin 555-B Autoclave Engineers, Inc., Erie, Pennsylvania (U)

E. 3 Autoclave Engineers Laboratory, Pilot-Plant, Plant Size Pressure Vessels, Bulletin 357-A, Autoclave Engineers, Inc., Erie, Pennsylvania (U).

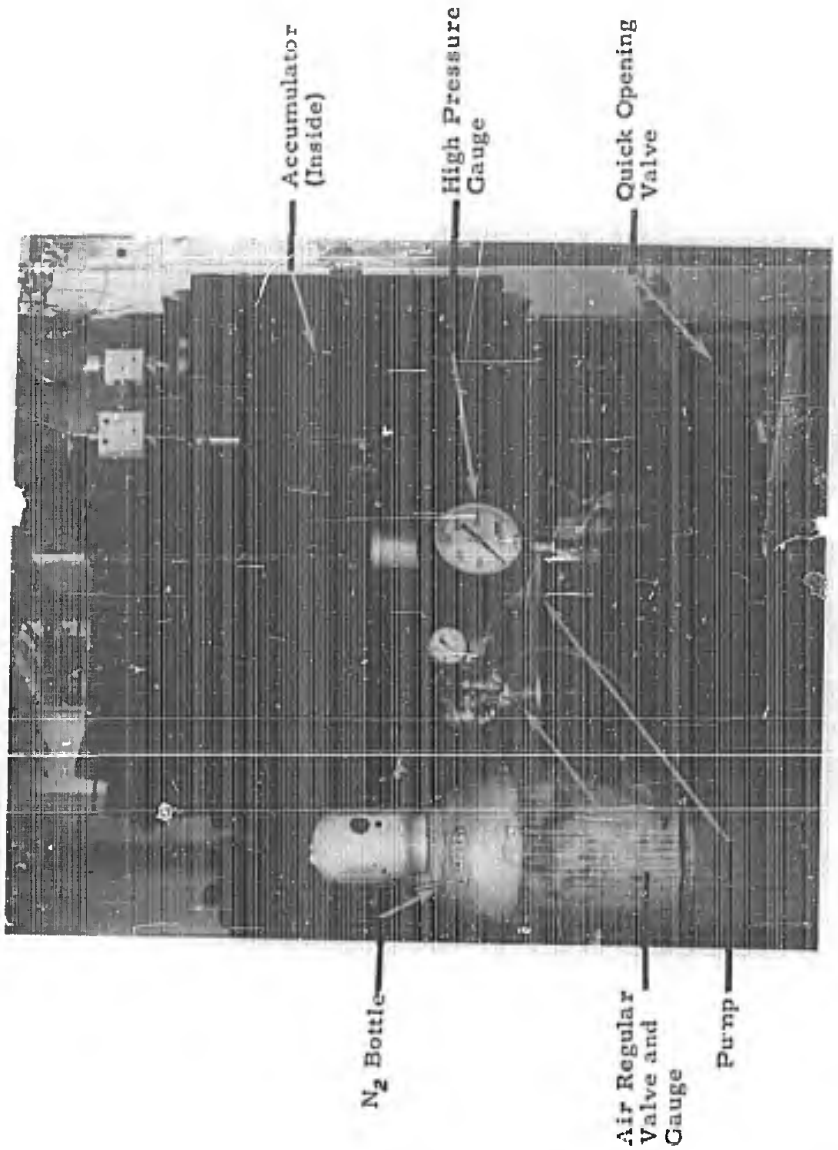

Figure E-1: High Pressure Pumping System

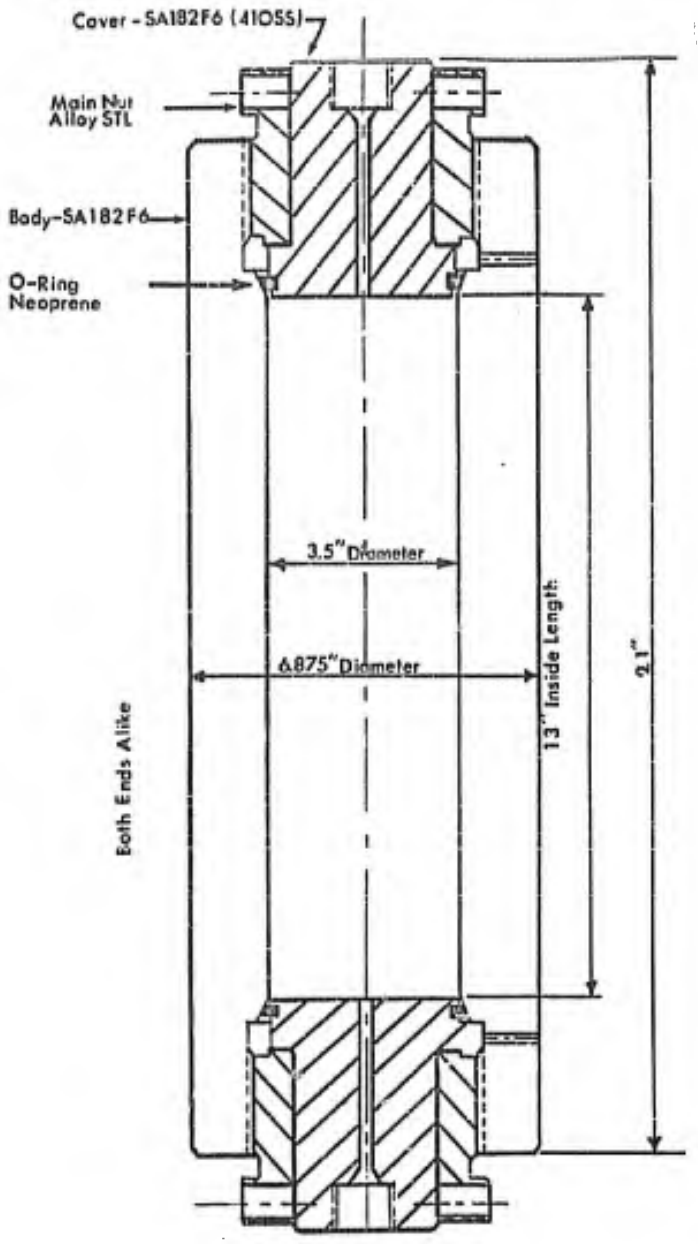

Figure E-2: High Pressure Accumulator

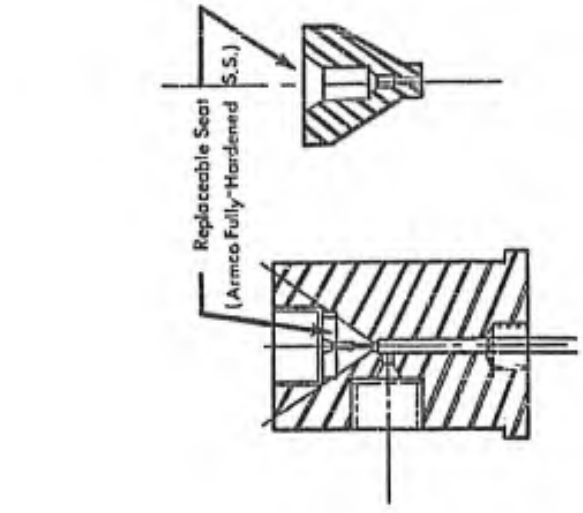

b) Modified Valve Body & Replaceable Seat

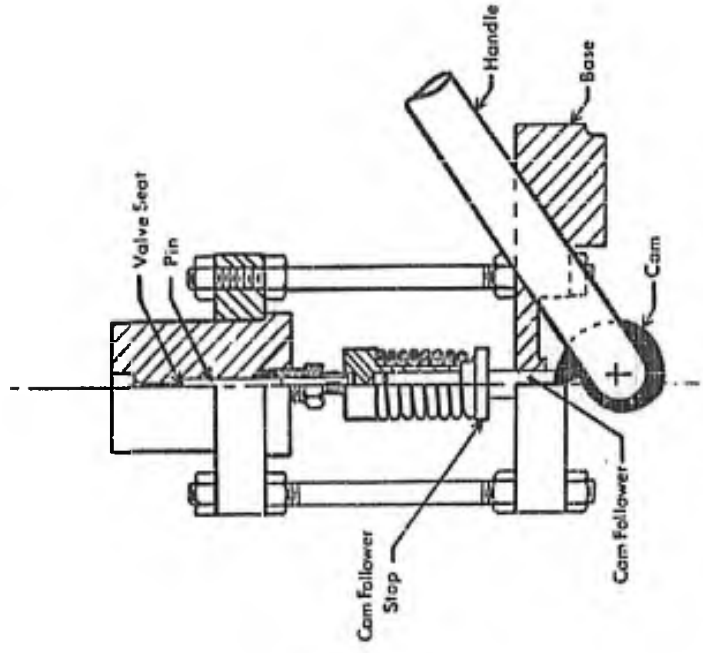

a) Unmodified Quick Opening Valve

Figure E-3: Quick Opening Valve and Modification

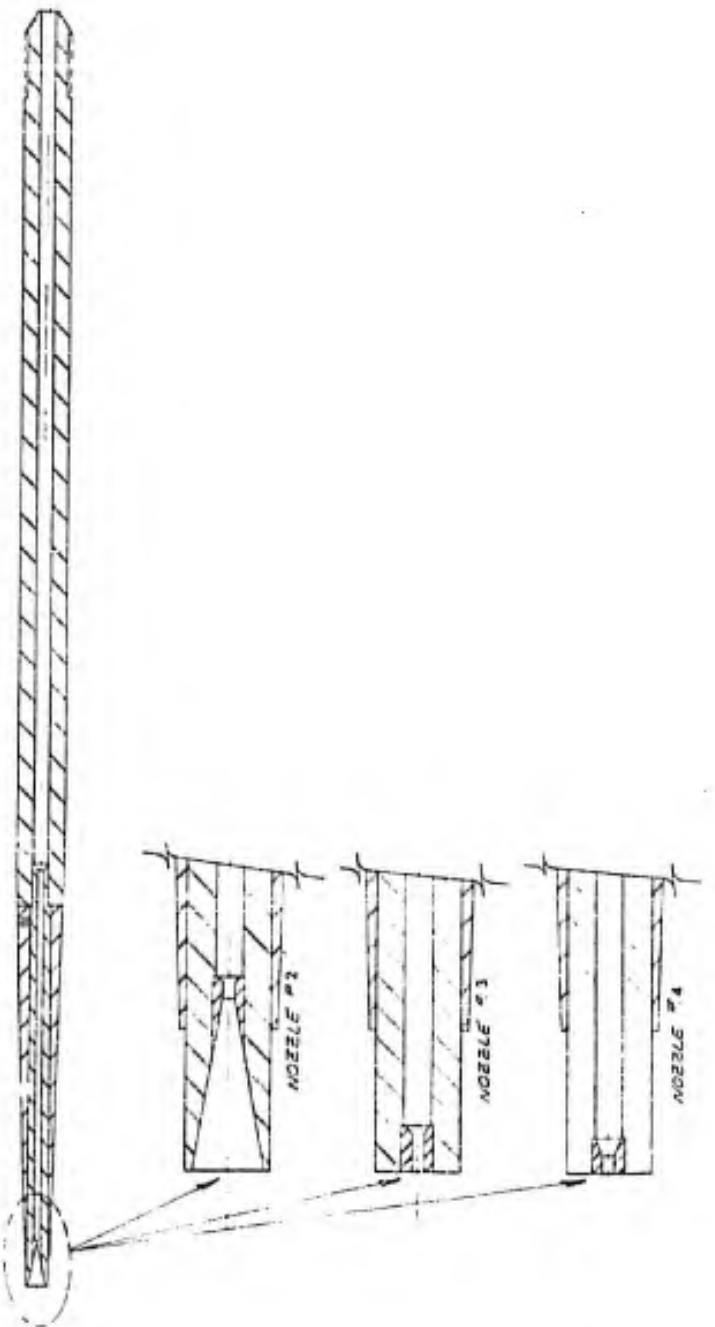

Figure E-4: Water Injection Nozzles

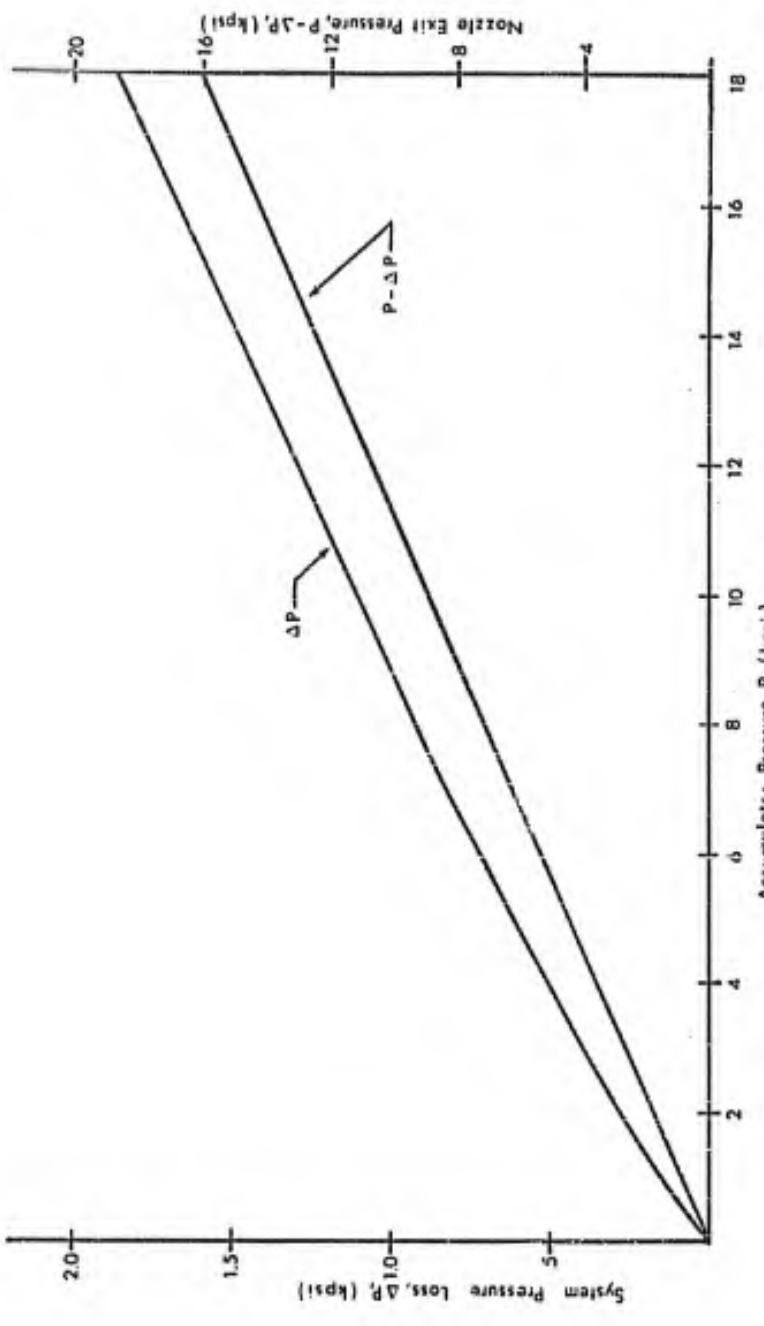

Figure E-5: System Pressure Loss Vs. Accumulator Pressure

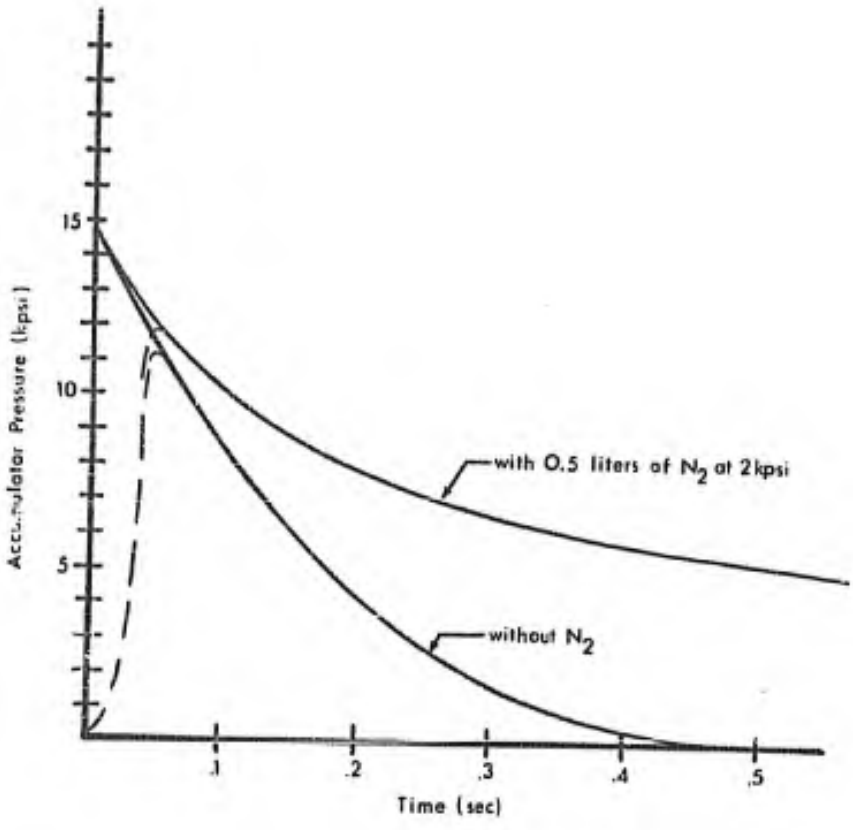

Figure E-6: Accumulator Pressure Vs. Time

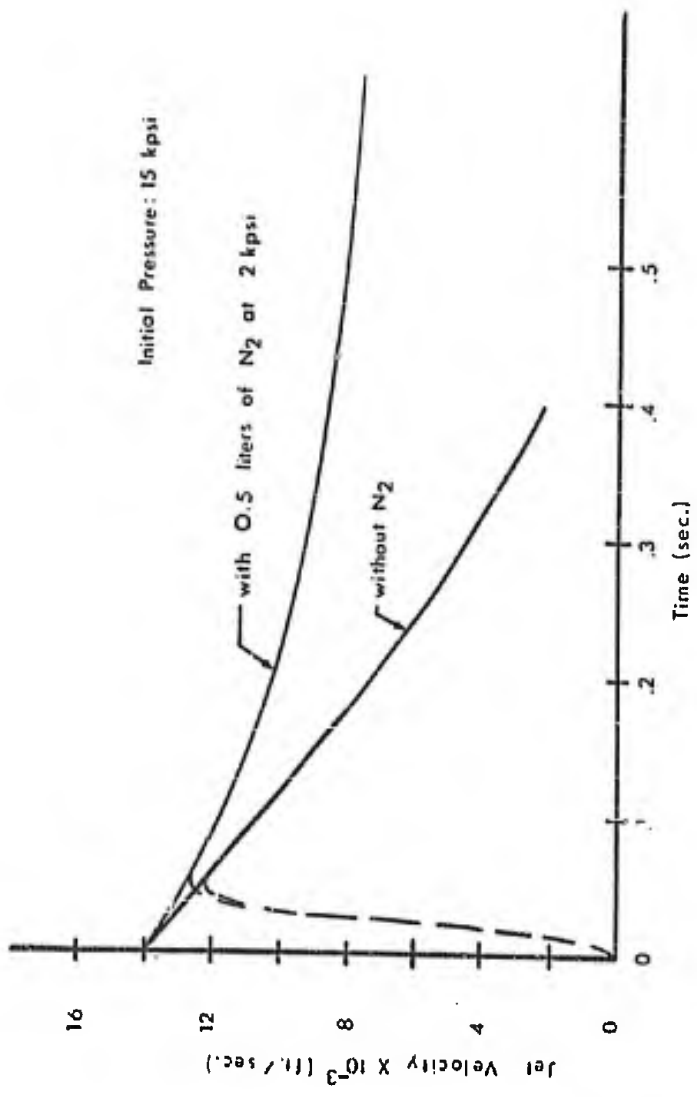

Figure E-7: Jet Velocity Vs. Time

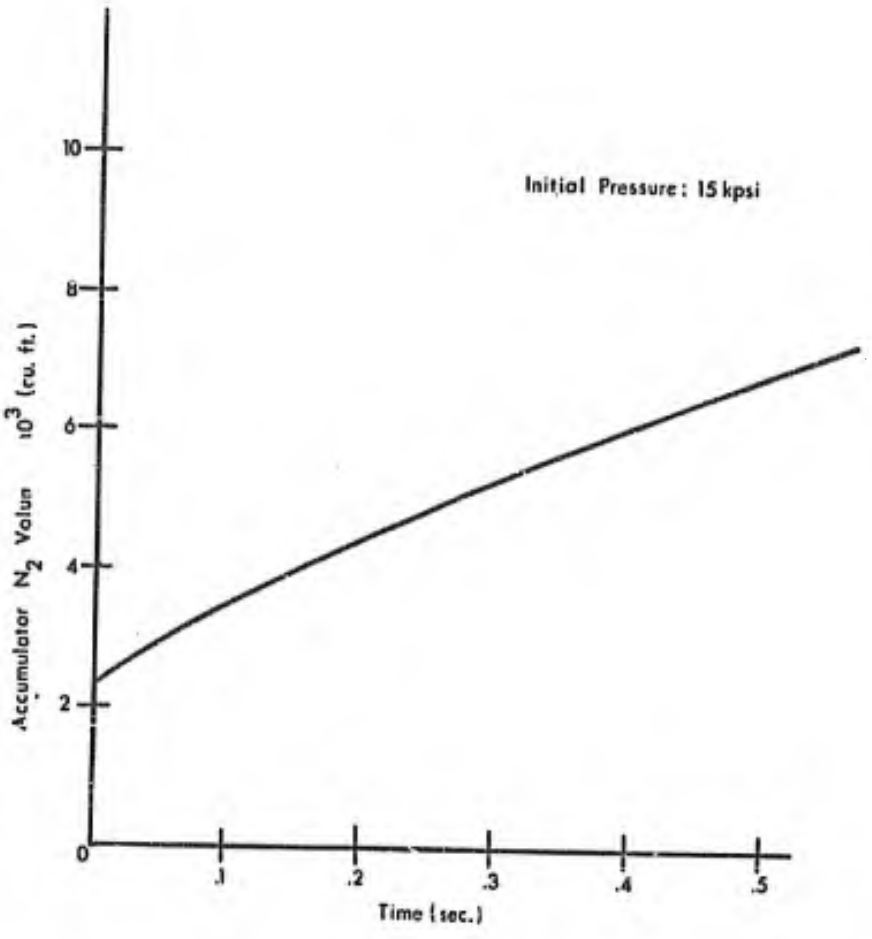

Figure E-8: Nitrogen Volume Vs. Time

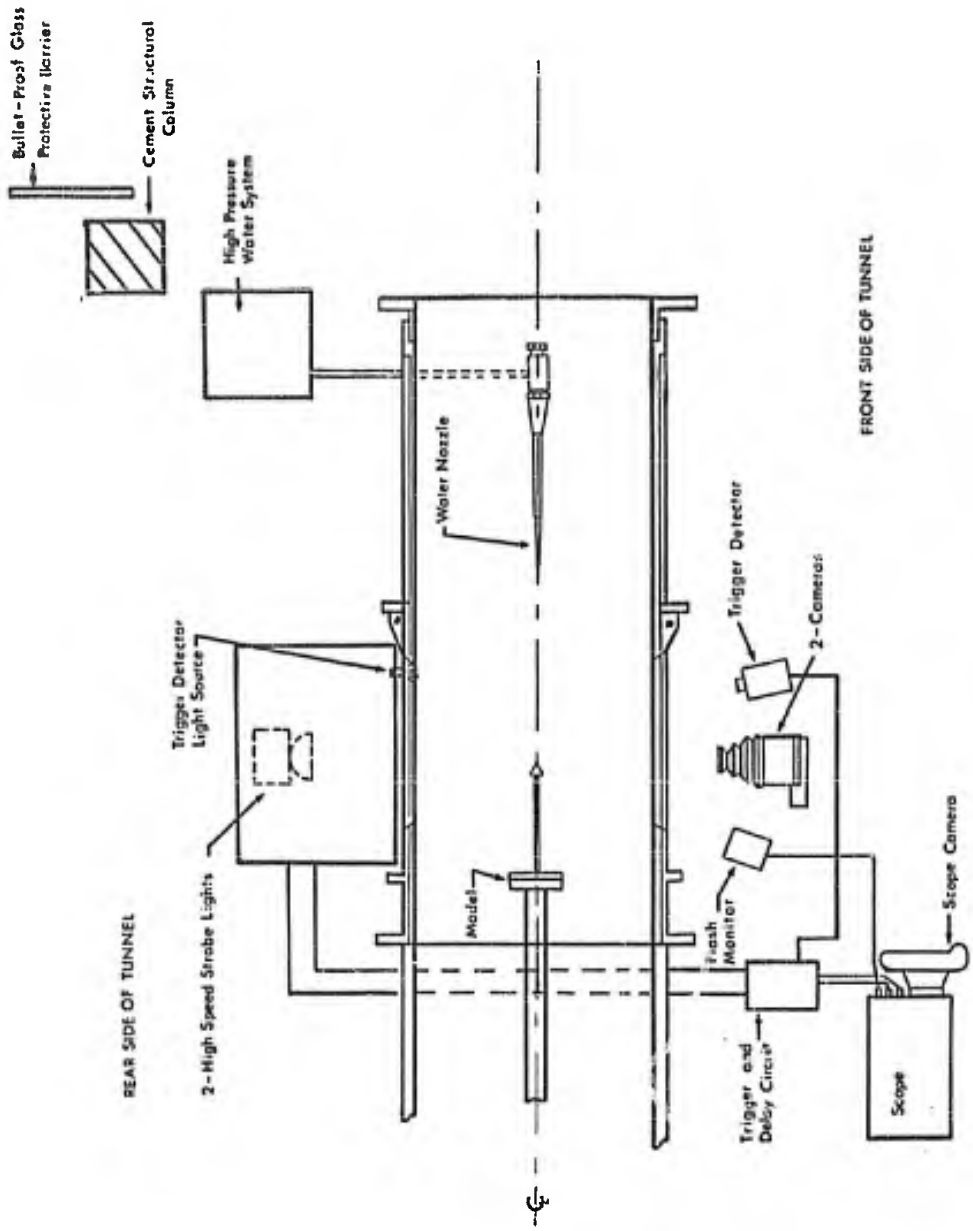

Figure E-9: Test Apparatus Layout

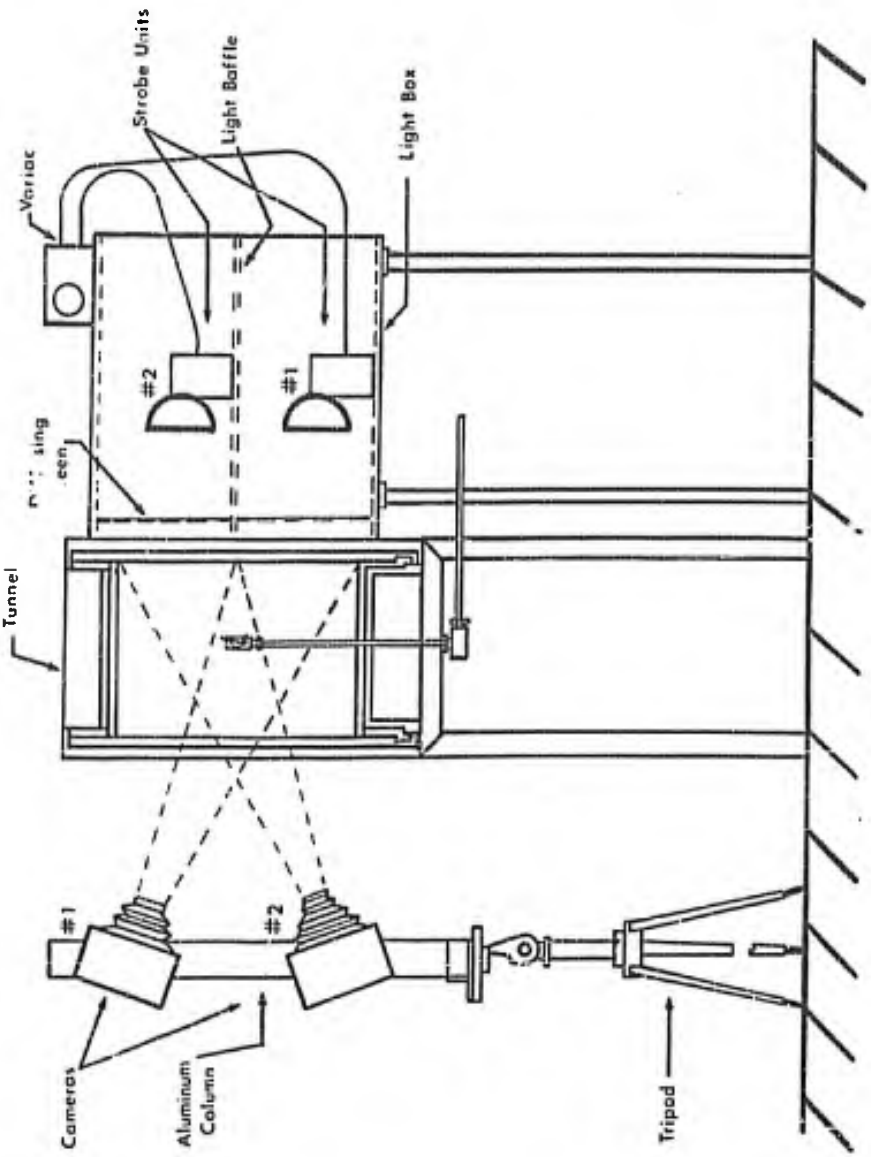

Figure E-10: Light Box and Camera Layout

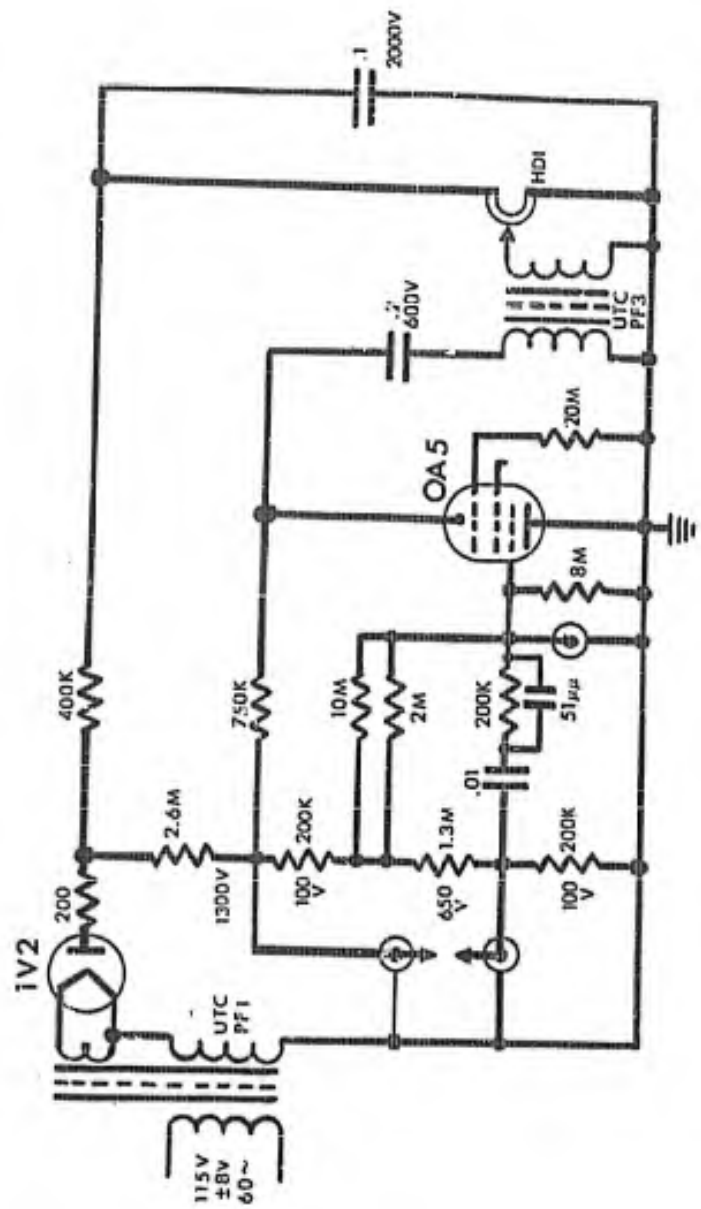

Figure E-11: Light Source Circuitry

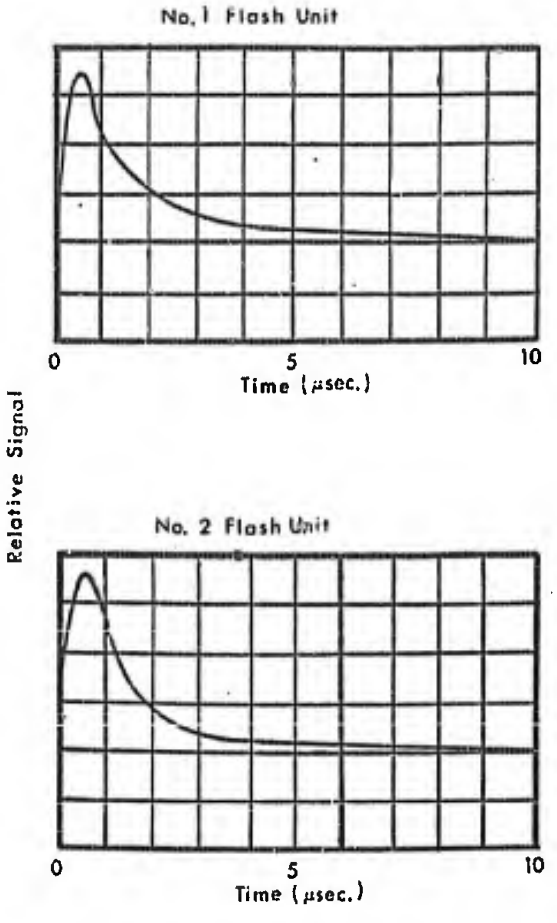

Figure E-12: Flash Duration of Light Sources

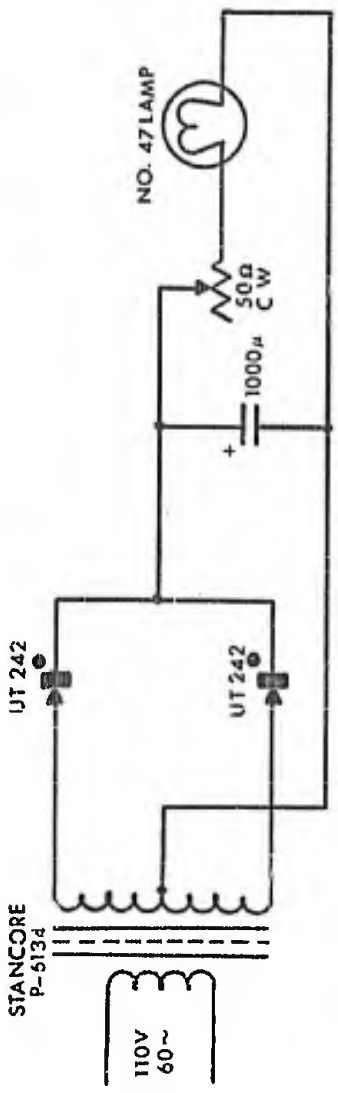

Figure E-13: Lamp and Power Supply

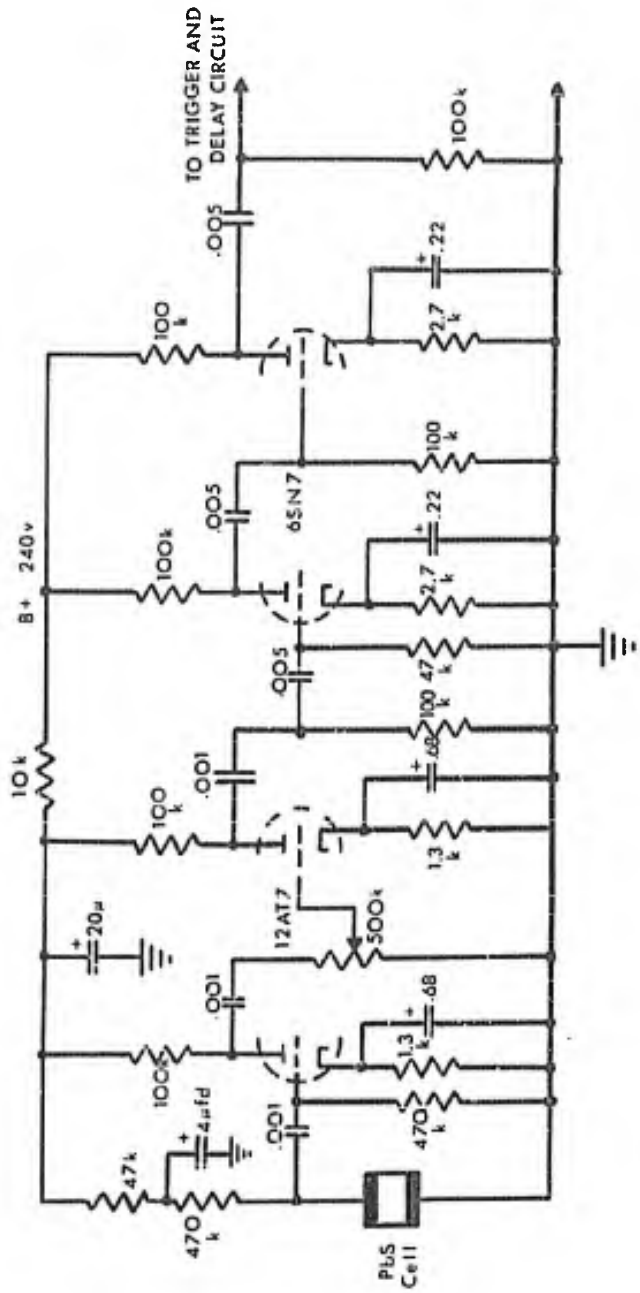

Figure E-14: Trigger Detector Circuit

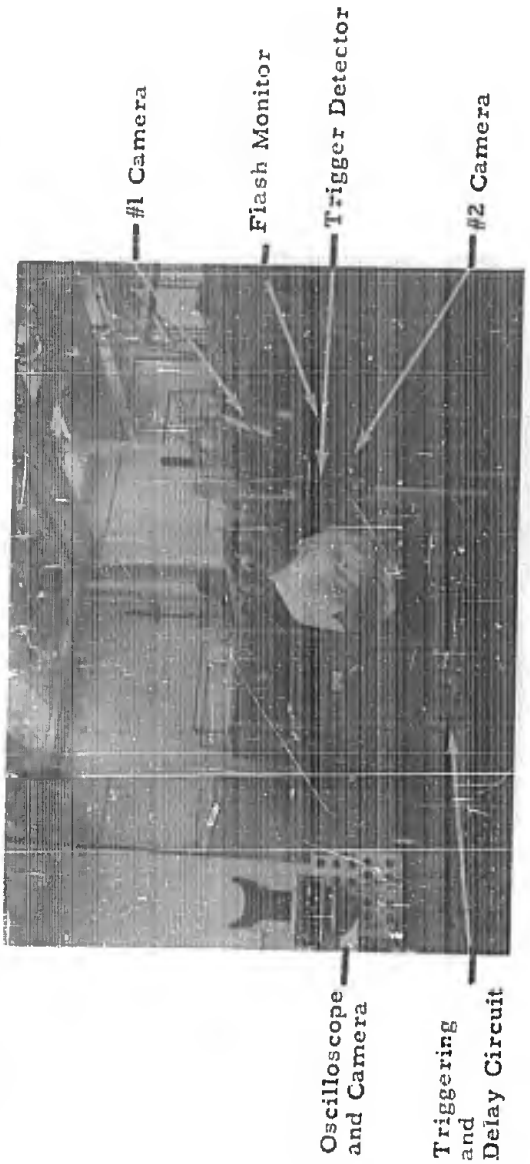

Figure E-15: Photograph of Test Section

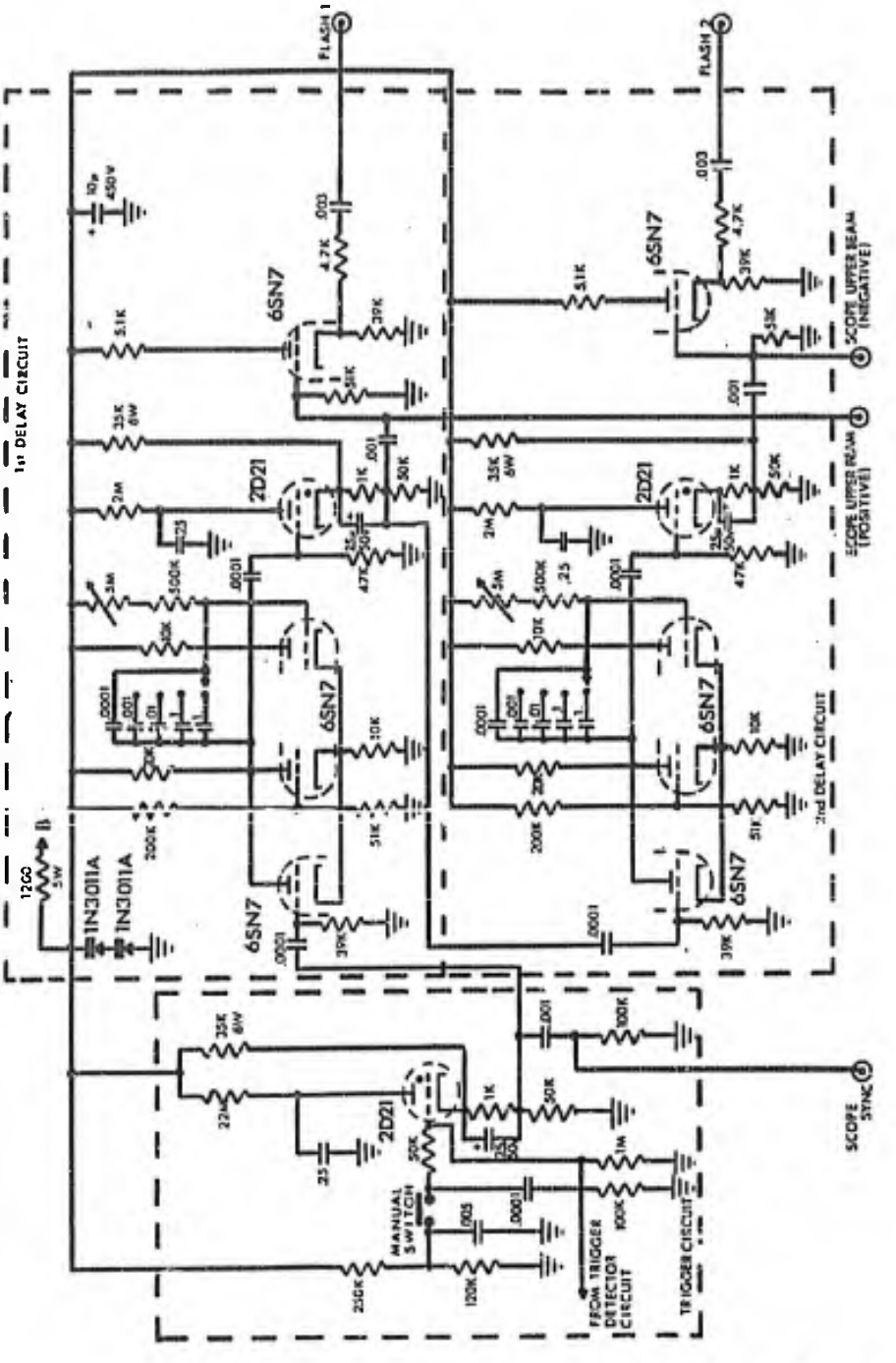

Figure E-16: Trigger Circuit and Delay Circuit

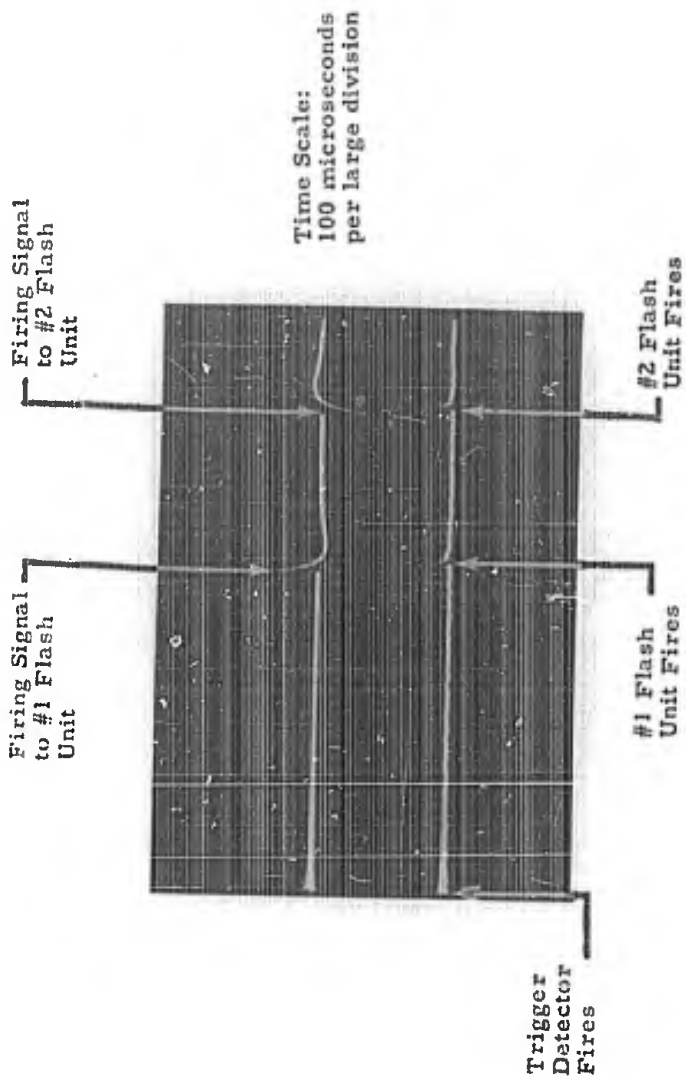

Figure E-17: Oscilloscope Trace of Typical Test Run

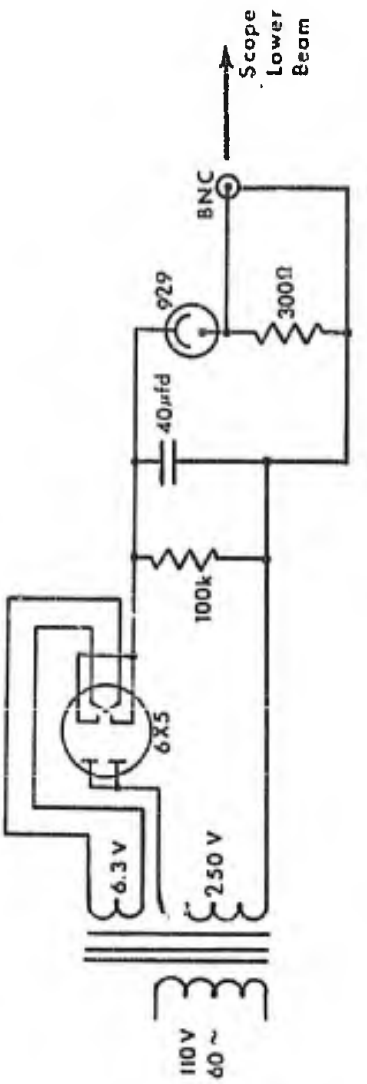

Figure E-18: Flash Monitor System Circuit

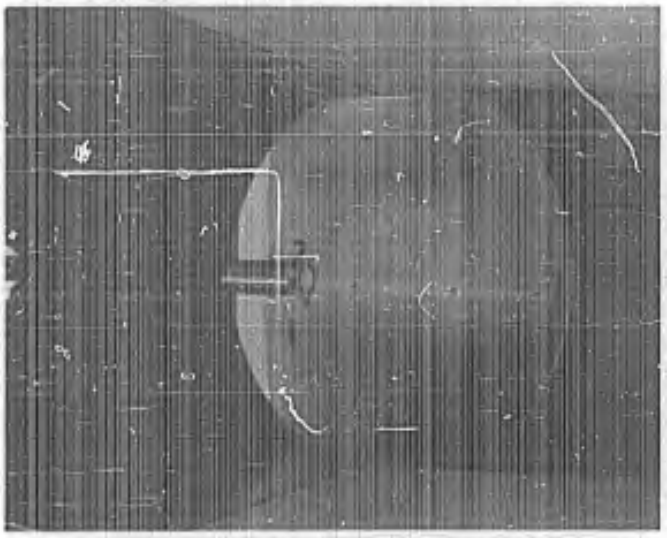

a. Without Sleeve

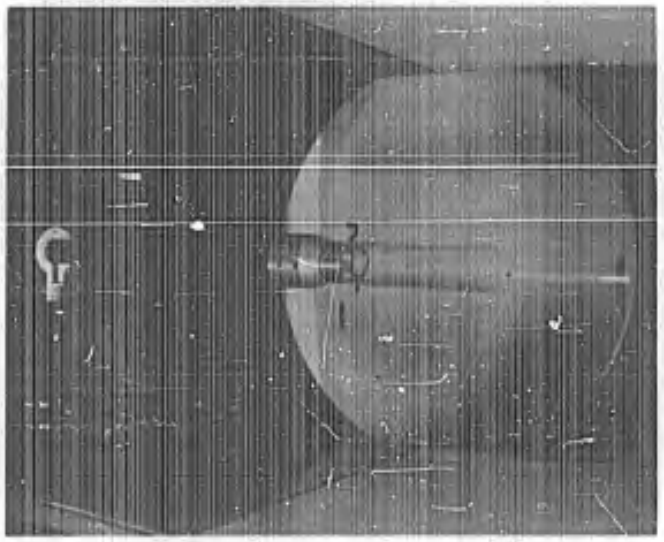

b. With Sleeve

Figure E-19: Sleeved Wind Tunnel Model

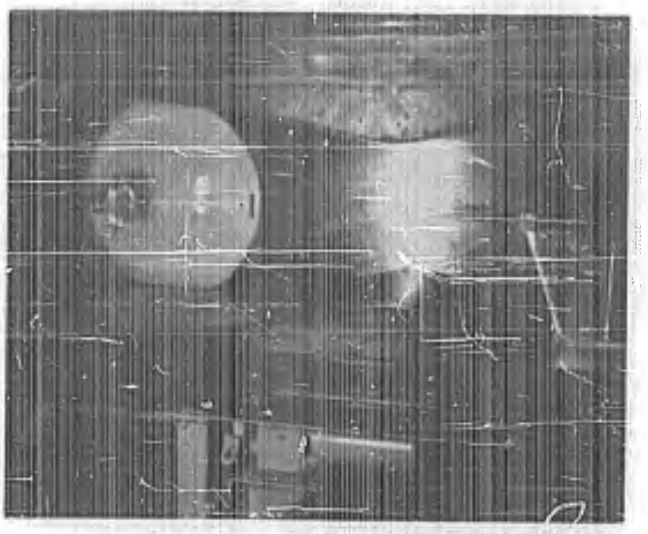

a. Without Spike

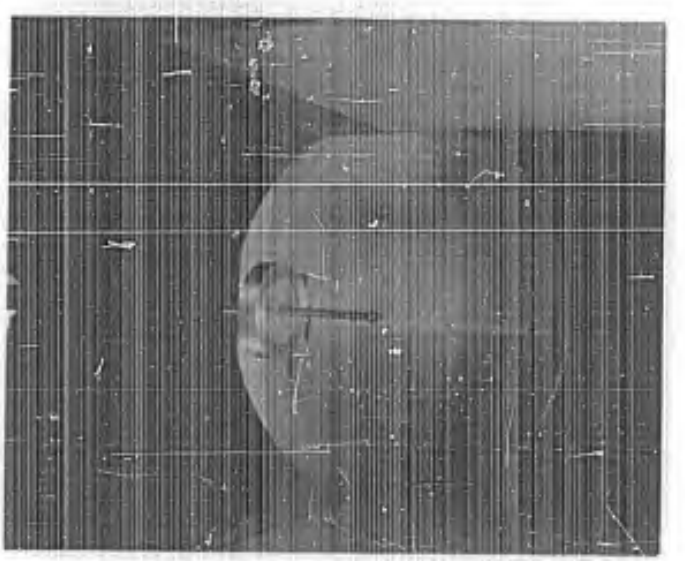

b. With Spike

Figure E-20: Flat Faced Wind Tunnel Model

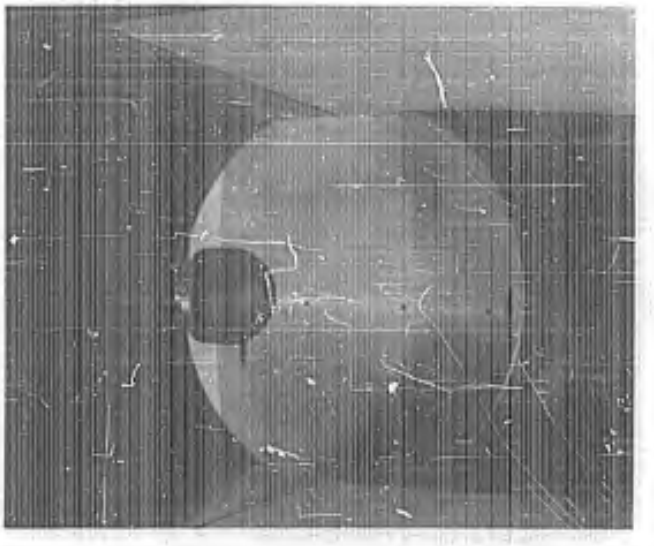

a. Without Spike

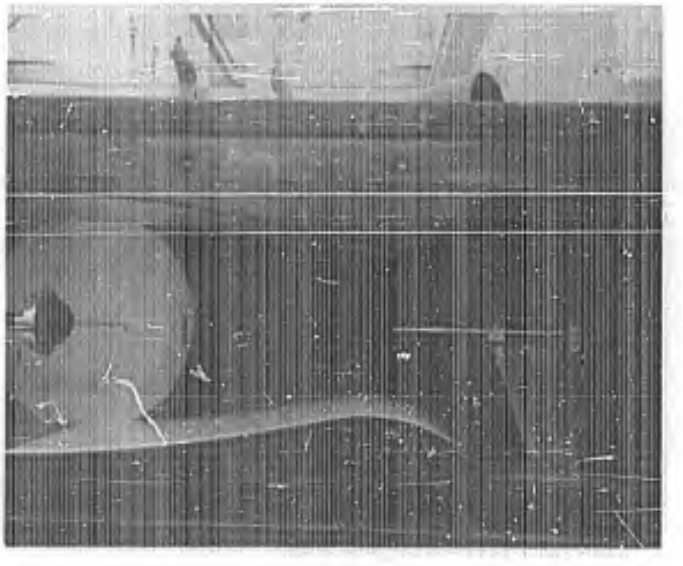

b. With Spike and 5 1/2 inch diameter Collar

Figure E-21: Hemispherical Radome Model

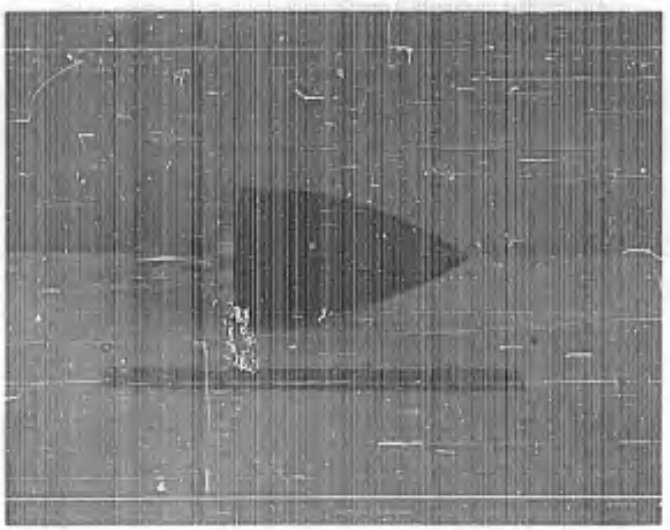

Figure E-22: Ogive Radome Model

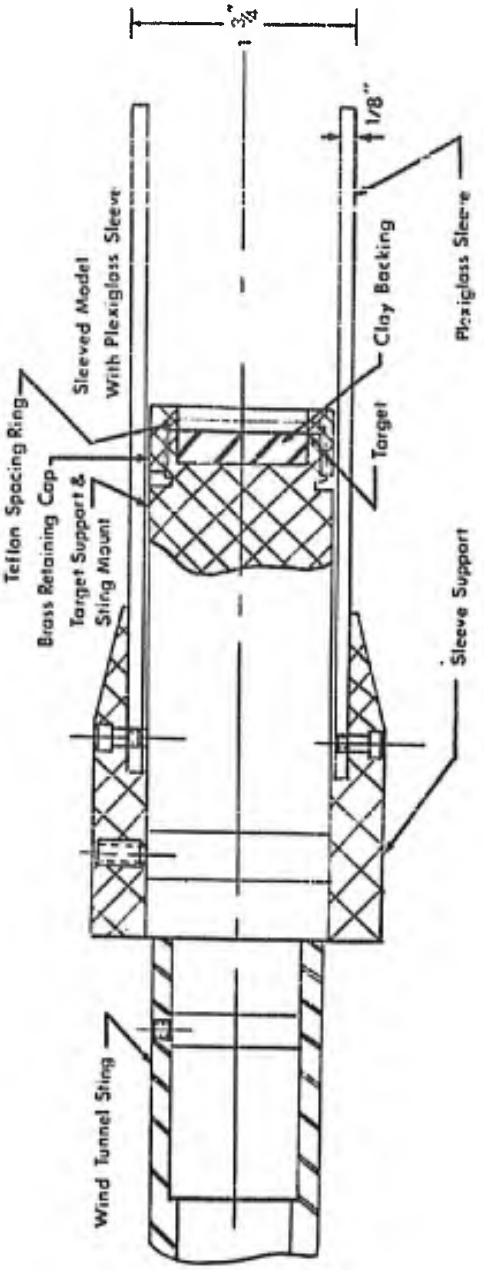

Figure F-23: Sleeved Model Details

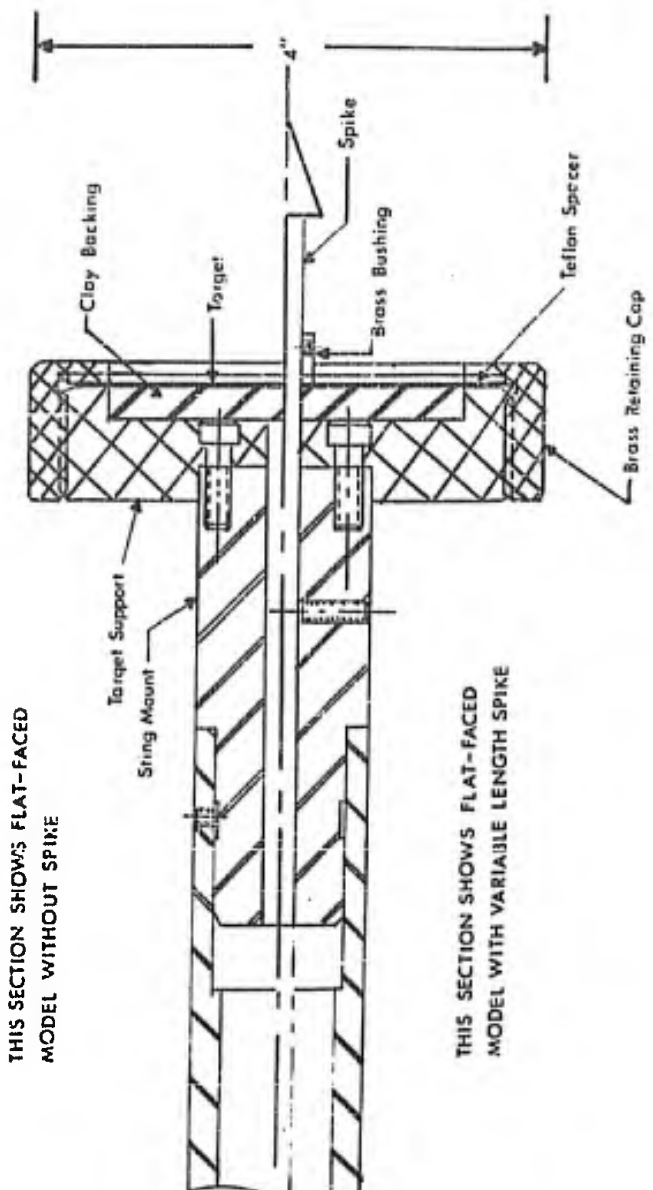

Figure E-24: Flat Faced Model Details

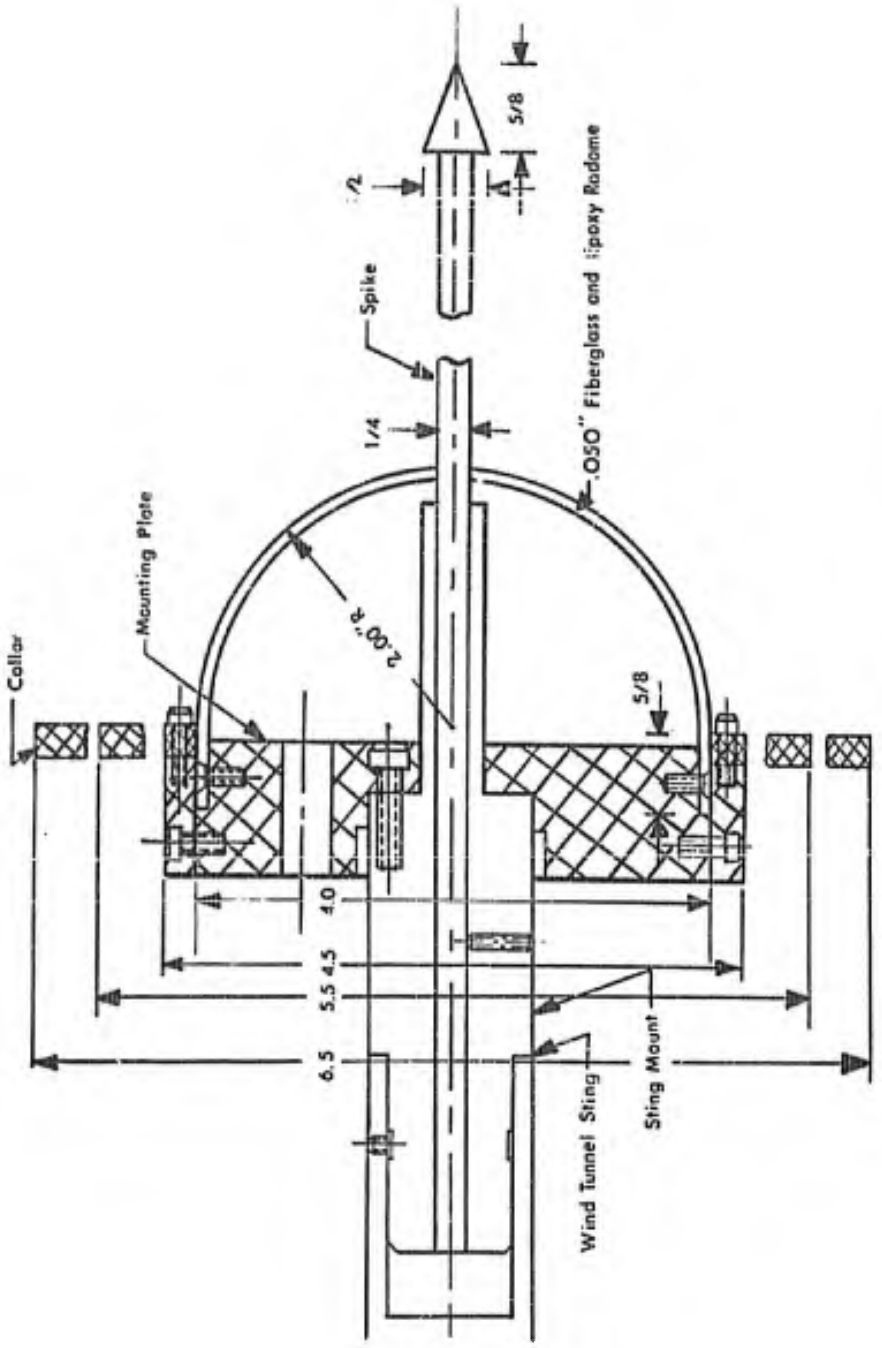

Figure E-25: Details of Fiberglass Radomes

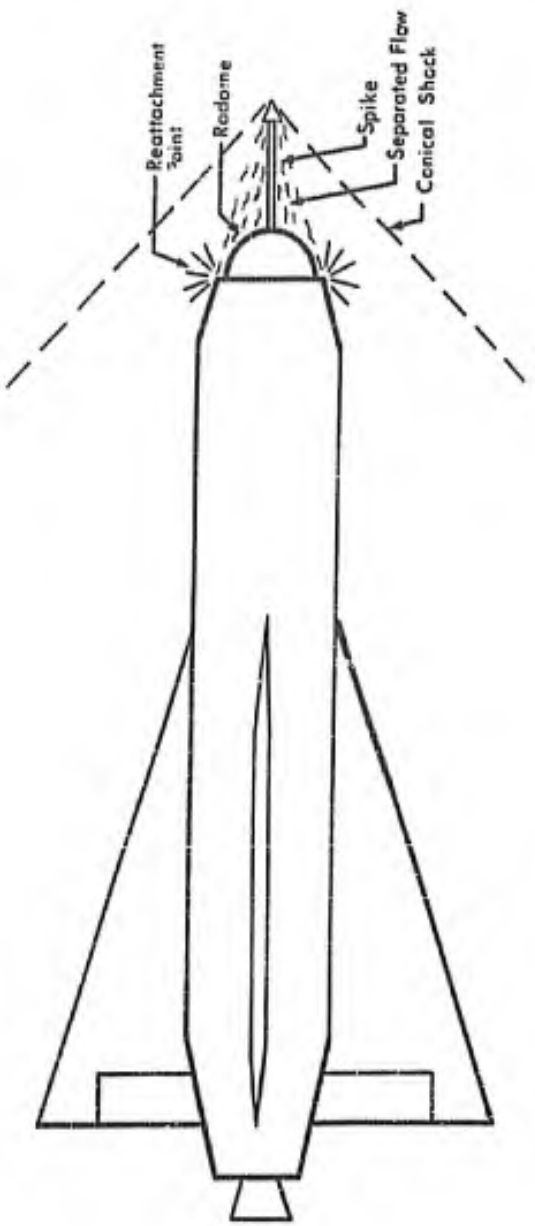

Figure E-26: Proposed Spiked Radome Configuration

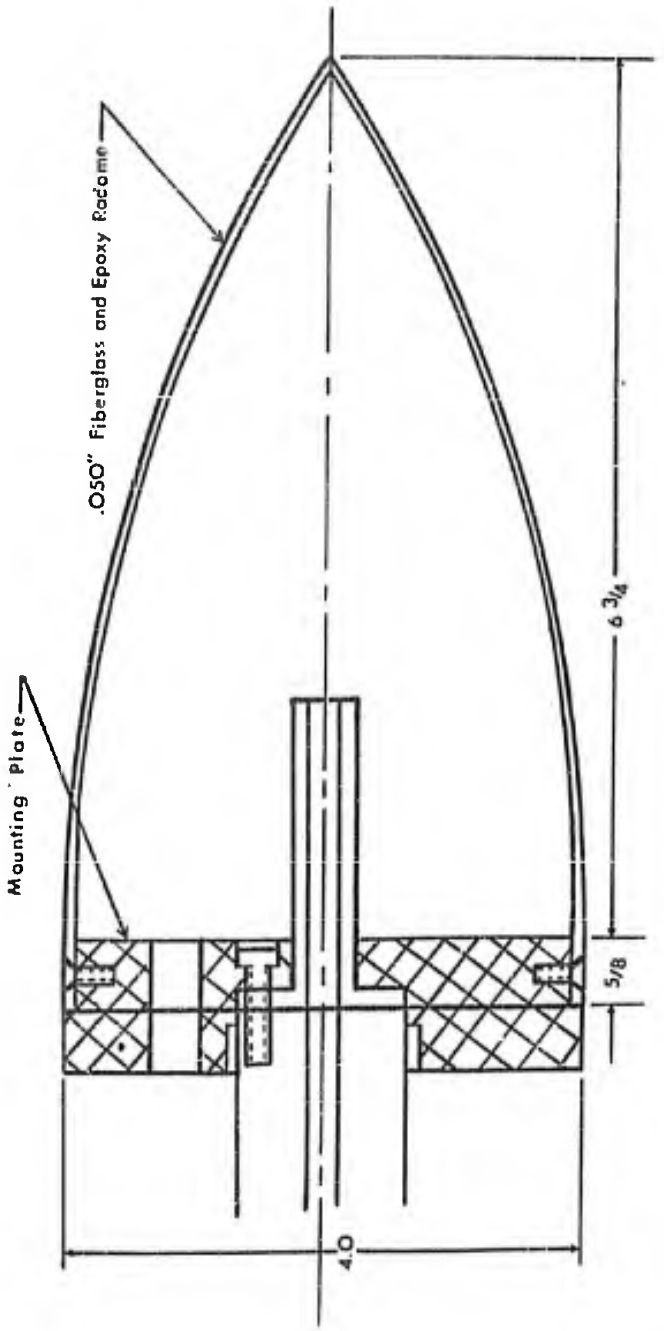

Figure E-27: Details of Ogive Radome Model

APPENDIX F
Water Drop Velocity

As indicated in Reference 1, some question had arisen after the previous year's tests concerning the reason for the apparent decrease of velocity with distance away from the water injection nozzle. To aid in our discussion of water velocity, Figure F-1 has been prepared. Part (a) of Figure F-1 illustrates a distortionless wave, one in which all parts of the wave travel with the same velocity. Such a wave does not alter its shape, either with time or distance. The line of maximum travel, describes the leading edge, in time and distance, of the disturbance, while the line of maximum disturbance is the locus of the crest of the wave in time and distance.

When the velocity is not constant for the wave, we have the situation represented in F-1b which, not incidentally, represents the physical situation that occurs during a firing of the water injection system. We see that the line of maximum travel is not now a straight line as in part (a) but is some curve asymptotic to the line of maximum velocity which is a straight line. The wave disturbance, in this case the velocity, is seen to change its shape with time or distance and hence is distorted. At any instant of time (one of the cuts illustrated), the distance-velocity curve is seen to be multivalued. In general, the foremost drops (corresponding to the line of maximum travel) are not the fastest drops (corresponding to the line of maximum velocity) until some moderately large value of time where the two curves join. Of course, in order for the faster drops to reach the front of the stream, they must pass the slower drops or collide with them. What the drop velocity will be after the collision depends upon the physics of the collision, i. e., whether the collision is elastic or plastic. In any event, it becomes clear that, initially (small values of time and distance) the faster drops form a relatively large fraction of the total number of ejected drops. In addition relatively few collisions have occurred so that the drop velocity may be large. With increasing time and distance however, the faster

drops will have a greater certainty of collision and the effect will be an apparent slowing down of the waterdrops with increasing time and/or distance.

Table F-1 summarizes the velocity measurements that were made from the photographs taken during the MITHRAS tests at DTMB. Two basic mechanisms were considered as determining the flow dynamics of the water jet. The first was the basic fluid dynamics involved in accelerating the water to the required velocity and the second and primary factor was the dynamics introduced into the system by the finite time required for the quick opening valve to open.

If the quick opening valve were instantaneously opened, it would still require a finite time to accelerate the water within the system to its final or steady state velocity. At the water nozzle throat the velocity can be derived (Reference F-1) to be

$$v = v_\infty \tanh \frac{v_\infty t}{2 \ell_1} \qquad \text{(F-1)}$$

where

v = velocity at nozzle throat

v_∞ = steady state velocity

t = time

$\ell_1 = \int_0^{\ell} A(s)\, ds$

$A(s) = \dfrac{\text{exit area}}{\text{area at station } s}$

s = distance measured from accumulator.

The integration is carried out over the length of piping extending from the accumulator to the nozzle throat. ℓ_1 for the water injection system is found to be 3.07 inches. For a supply pressure of 15 kpsi, the pressure at the nozzle throat is 13.5 kpsi and v is 1400 f.p.s. If we let $\tau = \dfrac{2\ell_1}{v_\infty}$, we find

$$\tau = 3.66 \times 10^{-4} \text{ seconds.}$$

The function tanh u is asymptotic to 1.0 and very nearly reaches this value by the time that u reaches 3. Therefore, the entire fluid flow should be stabilized out within 1 millisecond if no other effects were present. In the water injection system, other effects are, however present. It is known that the quick opening valve does not fully open for at least "4 or 5 milliseconds" after it is released. Thus the dynamics of the jet velocity can be expected to be determined by the dynamics involved in opening the quick opening valve. The dashed portions of the curves in Figures E-5 and E-6 indicate the probable shapes of these curves during the initial time interval that the valve is opening.

F. REFERENCES

F. 1 Prandtl, L. and Tietjens, O. G., Fundamentals of Hydro- and Aeromechanics, McGraw-Hill Book Company, Inc., N. Y., 1934 pp. 118-120 (U).

TABLE F-1

Tabulated Velocity Measurements

Run	Press. (kpsi)	Expected Max. Vel. (fps)	Actual Vel. (fps)	Station (To Nozzle) (in)	Time To 1st Flash (μsec)	Time Between Flashes (μsec)	$\frac{V}{V}$ Max.
127	15	1400	1080	26.5	780	290	.7714
135	15	1400	915	29.7	730	280	.654
136	15	1400	945	28.6	720	280	.675
137	15	1400	1420	28.2	740	280	1.014
137	15	1400	1380	27.1	740	280	.986
137	15	1400	1210	30.1	740	280	.864
64	18	1540	1153	31.7	860	160	.749
67	18	1540	1141	25.7	960	160	.741
69	18	1540	1145	27.1	860	190	.744
69	18	1540	926	27.2	860	190	.601
	18	1540	1110	22.7	840	190	.721
99	18	1540	943	27.6	720	160	.612
100	18	1540	1110	26.6	720	160	.721
107	18	1540	1033	26.0	725	160	.671
108	18	1540	1002	28.0	720	160	.651
116	18	1540	1244	31.5	620	140	.808
88	20	1610	1070	30.2	720	180	.665
88	20	1610	1205	30.0	700	180	.748
92	20	1610	1120	30.0	700	180	.696
92	20	1610	883	26.8	700	180	.548
94	20	1610	995	27.1	700	180	.618
96	20	1610	695	29.8	700	180	.432
100	20	1610	950	30.7	750	180	.590
74	16	1450	1020	26.2	840	165	.703
77	17.5	1520	1160	25.8	700	180	.763
78	17.5	1520	1090	25.8	700	165	.717
78	17.5	1520	985	34.7	700	165	.648
87	15.5	1440	900	33.3	700	150	.625
129C	25	1810	1100	29.5	750	180	.608

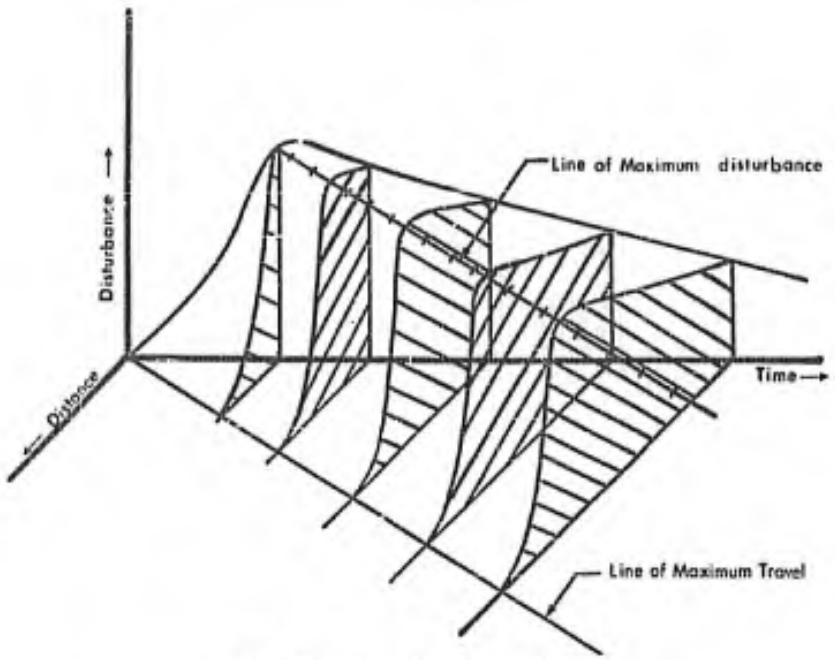

a. Distortionless disturbance

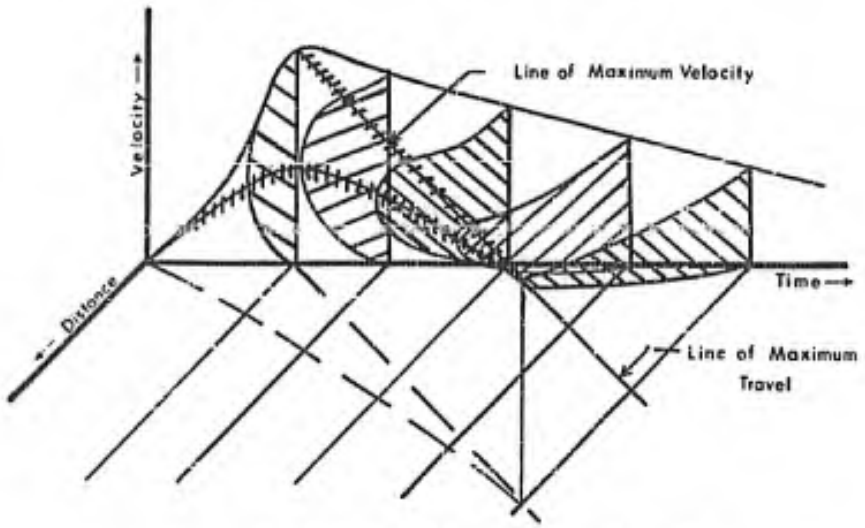

b. Velocity in time-distance plane

Figure F-1: Water Velocity Profile

APPENDIX G

Run Schedule

LEGEND

Run	Model Model Configuration Spike Length (inches)	Nozzle Nozzle Number	Pressure Starting Pressure (kpsi)	Pressure Final Pressure (kpsi)	N_2 Vol. Volume of N_2 (liters)	Position Nipple length (inches) (See Fig. E-21b)	Position Target distance from nozzle tip (inches)	Comments
0	A-3	2	30	10.5	0.5	6	20	

Wind Tunnel Conditions

Total Pressure = 14.7 psia Static Pressure = 2.33 psia

Total Temperature = 560° R Static Temperature = 331° R

Mach Number = 1.86

Conditions In Tube of Sleeved Model

Pressure = 11.55 psia

Temperature = 560° R

Density = 0.0558 lb/ft^3

NOZZLES

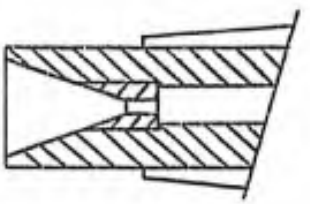

2

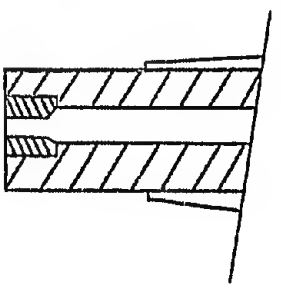

3

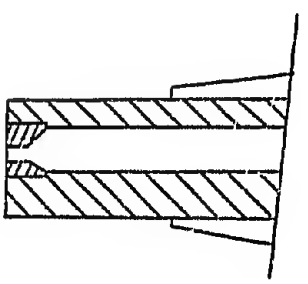

4

MODELS

Model A

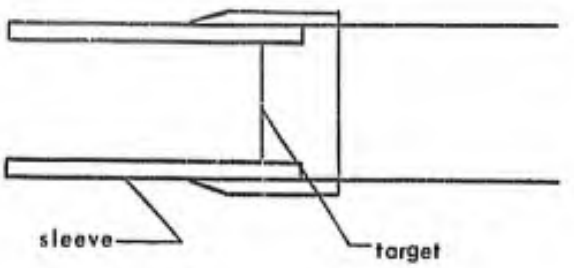

Model B

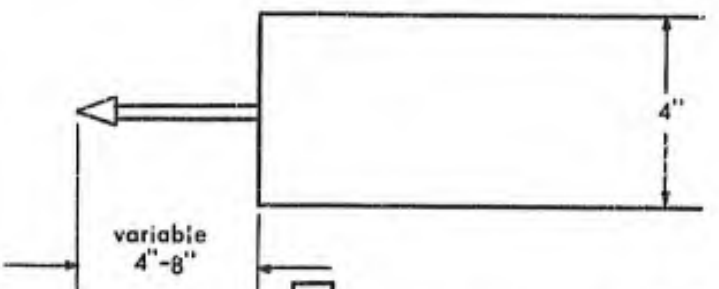

Model D

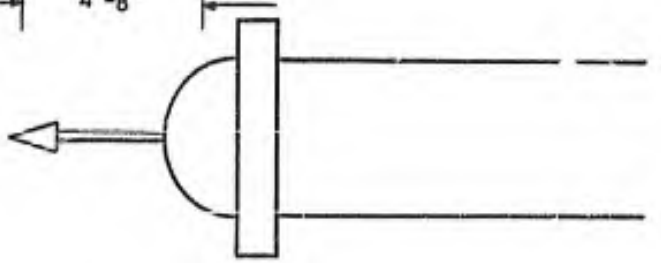

Model E

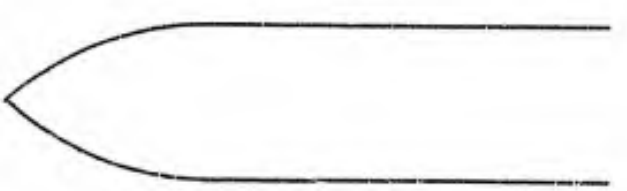

TABLE G-1

Run Schedule

Run	Model Config.	Nozzle	Pressure (kpsia)		N_2 Vol. liters	Position inches		Comments
			initial	final				
1A	B-0	2	20	0	0	0	28-3/4	No Water
1B	B-0	2	20	0	0	0	28-3/4	Water in second photo
1C	B-0	2	20	0	0	0	28-3/4	No Water
1D	B-0	2	20	0	0	0	28-3/4	No Air
1E	B-0	2	20	0	0	0	28-3/4	Water in photos
'A	B-0	4	20	0	0	0	28-3/4	No scope photo
2B	B-0	4	20	0	0	0	28-3/4	Unbacked
3A	B-0	4	20	0	0	6	22	Unbacked
3B	B-0	4	20	0	0	6	22	Unbacked
4A	B-0	3	20	0	0	6	22	No scope picture
4B	B-0	3	20	0	0	6	22	No photos, no backing
5A	B-0	2	20	0	0	6	22	No water, no scope photo
6	B-0	2	20	0	0	6	26	Lead target, water at 600μ sec.
7	B-0	2	20	0	0	6	30	Lead target
8A	B-0	2	20	2	0.2	6	30	No scope photo
8B	B-0	2	20	3	0.2	6	30	No photos
8C	B-0	2	20	3.5	0.2	6	30	
9	B-0	2	20	4.5	0.5	6	30	
10	B-0	2	20	4.5	0.5	6	21.6	Valve leaking
11	B-0	2	20	5.0	0.5	6	21.6	Fixed Valve
12	B-0	2	20	5.5	0.5	6	21.6	Very slight leak in valve

TABLE G-1 (continued)

Run Schedule

Run	Model Config.	Nozzle	Pressure (kpsia)		N_2 Vol.	Position		Comments
			initial	final	liters	inches		
13A	B-0	2	20	5.0	0.5	6	21.6	
13B	B-0	2	20	3.5	0.5	6	21.6	
14	B-0	2	20	3.5	0.5	6	21.6	.003 Shim ruptured
15	B-0	2	20	3.5	0.5	6	21.6	.003 Shim ruptured Replaced Valve Seat and stem
16	B-6	2	20	3.5	0.5	6	21.6	.003 Shim ruptured
17	B-0	2	30	3.5	0.5	6	21.6	
18	B-6	2	20	3.0	0.5	0	36.9	
19	B-6	3	20	3	0.5	0	36.9	Comparison with 20
20	B-0	3	20	3	0.5	0	36.9	
21	B-0	3	20	3	0.5	0	28.25	Comparison with 22
22	B-6	3	20	3.3	0.5	0	28.25	
23	B-6	3	20	3.5	0.5	4	23.4	Comparison with 24
24	B-0	3	20	3.5	0.5	4	23.4	
25	B-0	3	20	3	0.5	6	21.4	No photos
26A	B-0	4	20	3.4	0.5	6	21.4	No photos, no damage
26B	B-0	4	20	3.5	0.5	6	21.4	No photos, no damage
27	B-0	3	20	3.5	0.5	6	13.4	No photos, no damage
28	B-0	3	20	2	0.5	0	22	No photos, no damage

TABLE G-1 (continued)

Run Schedule

Run	Model Config.	Nozzle	Pressure (kpsia)		N_2 Vol.	Position		Comments
			initial	final	liters	inches		
29	B-0	3	20	4.5	0.5	0	26	No photos, no damage
30	B-0	3	20	3.5	0.5	0	32	No photos, no damage
31	B-0	3	20	3.5	0.5	0	30	No photos, no damage Comparison with 32 and 33
32	B-6	3	20	3.5	0.5	0	30	N photos, no damage
33	B-0	3	20	3.5	0.5	0	30	No photos, no damage
34A	B-6	3	20		0.5	0	26	
34B	B-6	3	20		0.5	0	26	
34C	B-6	3	20		0.5	0	26	
35A	B-0	3	20	4	0.5	0	26	Comparison with 35A, B, C, and 36A, B, C
35B	B-0	3	20	4	0.5	0	26	
35C	B-0	3	20	4	0.5	0	26	
36A	B-6	3	20	4	0.5	0	26	
36B	B-6	3	20	4	0.5	0	26	
36C	B-6	3	20	4	0.5	0	26	
37	A-6	3	20	1.5	0.5	0	26	
38	A-0	2	20	4	0.5	0	36	
39	A-0	2	20	4	0.5	0	36	Target ruptured (.003)
40	A-0	2	12.5	3.5	0.5	0	36	Comparison with 41

TABLE G-1 (continued)

Run Schedule

Run	Model Config.	Nozzle	Pressure (kpsia)		N_2 Vol.	Position		Comments
			initial	final	liters		inches	
41	A-6	2	12	3.5	0.5	0	36	
42	A-6	2	15	3	0.5	0	36	Comparison with 43
43	A-0	2			0.5	0	36	
44	A-6	2	20	3.5	0.5	0	36	No photos
45	A-0	2	20	4.0	0.5	0	36	No photos
46	A-0	2	12	4	0.5	0	27	
47	-0	2	12	4	0.5	0	27	Target bl- /n out
48	A-0	2	20	5	0.5	0	27	Lead target
49	A-6	2	20	4.5	0.5	0	27	Brass target
50	A-6	2	15	4.5	0.5	0	27	Brass target
51	A-0	2	15	4.5	0.5	0	27	Lead target, no photos
52	B-6	2	12	4	0.5	0	36	Lead target
53	B-0	2	12	3.25	0.5	0	36	Spike
54	B-0	2	12	3.5	0.5	0	36	No spike (.005 target)
55	B-6	2	12	4	0.5	0	36	
56	B-6	2	15	4	0.5	0	36	(.003 Shim)
57	B-0	2	15	3.0	0.5	0	36	
58	B-6	2	20	3.0	0.5	0	36	(.003 Shim)
59	B-6	2	18	5.0	0.5	0	36	.005 Stock
60	B-0	2	18	4.0	0.5	0	36	#1 flash did not fire
61	B-0	2	20	4	0.5	0	36	Pictures bad
62	B-6	2	20	4	0.5	0	36	No time photo

TABLE G-1 (continued)

Run Schedule

Run	Model Config.	Nozzle	Pressure (kpsia)		N_2 Vol.	Position		Comments
			initial	final	liters	inches		
63	B-6	2	18	4	0.5	0	36	.003 Shim, change valve body, no photos
64	B-6	2	18	4	0.5	0	36	
65	B-6	2	17	4	0.5	0	36	
66	B-0	2	17	4	0.5	0	36	
67	B-6	2	18	3.5	0.5	0	36	
68	B-0	2	18	3.5	0.5	0	36	
69	B-5 1/2	2	18	3.5	0.5	0	36	
70	B-6 1/4	2	18	3.0	0.5	0	36	
71	B-6 1/2	2	18	2.5	0.5	0	36	
72	B-7	2	18	3.0	0.5	0	36	No photos
73A	B-0	2	10	0.5	0.5	0	36	No photos
73B	B-0	2	12	0.5	0.5	0	36	No photos
73C	B-0	2	15	0.5	0.5	0	36	No photos
74	B-0	2	16	4.0	0.5	0	36	
75	B-2	2	17.5	4.0	0.5	0	36	
76	B-4	2	17.5	4	0.5	0	36	
77	B-5	2	17.5	4.5	0.5	0	36	
78	B-6	2	17.5	4.0	0.5	0	36	
79	B-6 1/2	2	17.5	4.0	0.5	0	36	
80	B-7	2	17.5	4.0	0.5	0	36	Replaced valve
81	B-8	2	17.5	4.5	0.5	0	36	
82	B-10	2	17.5	4.25	0.5	0	36	
83	B-0	2	17.5	4.0	0.5	0	36	
84	B-0	2	20	4.75	0.5	0	36	.005 Stock

TABLE G-1 (continued)

Run Schedule

Run	Model Config.	Nozzle	Pressure (kpsia)		N_2 Vol.	Position		Comments
			initial	final	liters		inches	
85	B-0	2	22.5	4.25	0.5	0	36	.005 Stock
86	B-6 1/2	2	22.5	4.50	0.5	0	36	.005 Stock
87	B-0	2	15.5	4	0.5	0	36	Lead target
88	B-0	2	20	4.5	0.5	0	36	Lead target
89	B-6 1/2	2	20	4.5	0.5	0	36	Lead target
90	B-7	2	20	4.0	0.5	0	36	Lead target
91	B-10	2	20	4.0	0.5	0	36	Lead target
92	B-6	2	20	4.5	0.5	0	36	Lead target
93	B-5	2	20	4.0	0.5	0	36	Lead target
94	B-3	2	20	4.7	0.5	0	36	Lead target
95	B-0	2	20	4.0	0.5	0	36	Lead target
96	B-0	2	20	4.0	0.5	0	36	Lead target
97A	A-0	2	12	2	0.5	0	36	
97B	A-0	2	11	4	0.5	0	36	
97C	A-0	2	15	4	0.5	0	36	
97D	A-0	2	17	4	0.5	0	36	
98	A-0	2	18	5	0.5	0	36	
99	A-0	2	18	5	0.5	0	36	
100	A-0	2	18	5	0.5	0	36	Lead target
101	A-6	2	18	5	0.5	0	36	
102	A-6	2	18	5	0.5	0	36	Lead target
103	A-9	2	18	5	0.5	0	36	
104	A-9	2	18.5	5	0.5	0	36	Lead target
105	A-5	2	18	5	0.5	0	36	
106	A-5	2	18	4.5	0.5	0	36	Lead target

TABLE G-1 (continued)

Run Schedule

Run	Model Config.	Nozzle	Pressure (kpsia)		N_2 Vol.	Position		Comments
			initial	final	liters	inches		
107	A-5	2	18	5.0	0.5	0	36	Repeat of 105
108	A-4 1/2	2	18	4.75	0.5	0	36	
109	A-4 1/2	2	18	4.5	0.5	0	36	Lead target
110	A-4 1/2	2	18	5	0.5	0	36	Repeat of 108
111	A-4	2	18	5	0.5	0	36	
112	A-4	2	18	2.5	0.5	0	36	Lead target
13	A-3 1/2	2	18	4.75	0.5	0	36	N photos
114	A-3 1/2	2	18	3.5	0.5	0	36	Lead target
115	A-3	2	18	5.0	0.5	0	36	
116	A-1 3/4	2	18	4.5	0.5	0	36	
117	A-1 3/4	2	18	5.0	0.5	0	36	Lead target
118	A-0	2	18	5.0	0.5	0	36	
119	A-0	2	25	5.5	0.5	0	36	.005 Stock
120	A-0	2	25	5.75	0.5	0	36	.005 Stock
121	A-0	2	25	5.25	0.5	0	36	.005 Stock
122	A-0	2	25	5.5	0.5	0	36	
123	A-0	2	25	5.5	0.5	0	36	
124A	A-0	2	10	3.5	0.5	0	36	
124B	A-0	2	12.5	4.0	0.5	0	36	
124C	A-0	2	15	3.5	0.5	0	36	
124D	A-0	2	20	4.5	0.5	0	36	
124E	A-0	2	24.5	5.5	0.5	0	36	
125	A-0	2	21	2.5	0.5	0	36	
126	D-4	2	12	2.0	0.5	0	36	
127	D-4	2	15	1.5	0.5	0	36	

TABLE G-1 (continued)

Run Schedule

Run	Model Config.	Nozzle	Pressure (kpsia) initial	Pressure (kpsia) final	N_2 Vol. liters	Position inches		Comments
128	D-4	2	15	1.5	0.5	0	36	
129A	A-0	2	15	0	0	0	36	Change seat, fix pump, no nitrogen
129B	A-0	2	20	0	0	0	36	No nitrogen
129C	A-0	2	25	0	0	0	36	No nitrogen
130A	A-0	2	25	0	0	0	36	
130B	A-0	2	20	0	0	0	36	
131A	A-0	2	10	4	0.5	0	36	With nitrogen
131B	A-0	2	15	4.5	0.5	0	36	
131C	A-0	2	20	3.5	0.5	0	36	
132	D-6	2	15	4.5	0.5	0	36	5-1/2" collar, 6" spike
133	D-6	2	15	4.5	0.5	0	36	5-1/2", Collar Model DII
134	D-6	2	15	5.0	0.5	0	36	5-1/2", Collar Model DII
135	D-0	2	15	4.5	0.5	0	36	Remove spike and ring and rotate model 180°
136	D-0	2	15	2.5	0.5	0	36	
137	D-0	2	15	4.5	0.5	0	36	
138	D-0	2	15	4.0	0.5	0	36	Model DIII
139	D-0	2	15	4.0	0.5	0	36	Model DIII
140	D-0	2	15	4.5	0.5	0	36	Model DII
141	D-6	2	15	4.0	0.5	0	36	Model DI
142	D-6	2	15	4.5	0.5	0	36	

TABLE G-1 (continued)

Run Schedule

Run	Model Config.	Nozzle	Pressure (kpsia) initial	Pressure (kpsia) final	N_2 Vol. liters	Position inches		Comments
143	D-6	2	15	2.5	0.5	0	36	
144	E-0	2	15	1.5	0.5	0	36	Model EI
145	E-0	2	15	3.5	0.5	0	36	Model EII

MC-61-6-R2 MITHRAS, INC., Cambridge, Mass.

A SOLUTION TO THE PROBLEM OF RAIN EROSION AT SUPERSONIC SPEEDS (Unclassified Title)
Interim Report, Contract 3684(00) 149 and xiv pages, October, 1963.

The second year's work on the alleviation of rain erosion damage to radomes through the use of flow separating devices, culminated by a series of successful wind tunnel tests of the technique, is described. Actual radome models were afforded excellent protection through the use of physical spikes while conventional unprotected hemispherical and ogival domes were severely damaged under identical test conditions. Pertinent equations and a description of the test apparatus employed are included.

CONFIDENTIAL

1. Radomes
2. Rain Erosion
3. Spiked Bodies

I. Mithras, Inc. MC-61-6-R2

II. Figler, B. D.

CONFIDENTIAL

MC-61-6-R2 MITHRAS, INC., Cambridge, Mass.

A SOLUTION TO THE PROBLEM OF RAIN EROSION AT SUPERSONIC SPEEDS (Unclassified Title)
Interim Report, Contract 3684(00) 149 and xiv pages, October, 1963.

The second year's work on the alleviation of rain erosion damage to radomes through the use of flow separating devices, culminated by a series of successful wind tunnel tests of the technique, is described. Actual radome models were afforded excellent protection through the use of physical spikes while conventional unprotected hemispherical and ogival domes were severely damaged under identical test conditions. Pertinent equations and a description of the test apparatus employed are included.

CONFIDENTIAL

1. Radomes
2. Rain Erosion
3. Spiked Bodies

I. Mithras, Inc. MC-61-6-R2

II. Figler, B. D.

CONFIDENTIAL

MC-61-6-R2 MITHRAS, INC., Cambridge, Mass.

A SOLUTION TO THE PROBLEM OF RAIN EROSION AT SUPERSONIC SPEEDS (Unclassified Title)
Interim Report, Contract 3684(00) 149 and xiv pages, October, 1963.

The second year's work on the alleviation of rain erosion damage to radomes through the use of flow separating devices, culminated by a series of successful wind tunnel tests of the technique, is described. Actual radome models were afforded excellent protection through the use of physical spikes while conventional unprotected hemispherical and ogival domes were severely damaged under identical test conditions. Pertinent equations and a description of the test apparatus employed are included.

CONFIDENTIAL

1. Radomes
2. Rain Erosion
3. Spiked Bodies

I. Mithras, Inc. MC-61-6-R2

II. Figler, B. D.

CONFIDENTIAL

MC-61-6-R2 MITHRAS, INC., Cambridge, Mass.

A SOLUTION TO THE PROBLEM OF RAIN EROSION AT SUPERSONIC SPEEDS (Unclassified Title)
Interim Report, Contract 3684(00) 149 and xiv pages, October, 1963.

The second year's work on the alleviation of rain erosion damage to radomes through the use of flow separating devices, culminated by a series of successful wind tunnel tests of the technique, is described. Actual radome models were afforded excellent protection through the use of physical spikes while conventional unprotected hemispherical and ogival domes were severely damaged under identical test conditions. Pertinent equations and a description of the test apparatus employed are included.

CONFIDENTIAL

1. Radomes
2. Rain Erosion
3. Spiked Bodies

I. Mithras, Inc. MC-61-6-R2

II. Figler, B. D.

CONFIDENTIAL